

PULSED ACCRETION IN ECCENTRIC BINARIES:
AN OBSERVATIONAL STUDY OF THE PHOTOMETRIC AND KINEMATIC
VARIABILITY OF ACCRETION IN SHORT-PERIOD, PRE-MAIN SEQUENCE
BINARY STARS

by

BENJAMIN M. TOFFLEMIRE

A dissertation submitted in partial fulfillment of
the requirements for the degree of

DOCTOR OF PHILOSOPHY

(ASTRONOMY)

at the

UNIVERSITY OF WISCONSIN–MADISON

2018

Date of final oral examination: 29 May 2018

The dissertation is approved by the following members of the Final Oral Committee:

Dr. Robert Mathieu, Professor, Astronomy

Dr. Sebasitan Heinz, Professor, Astronomy

Dr. Richard Townsend, Associate Professor, Astronomy

Dr. Dan McCammon, Professor, Physics

ProQuest Number: 10837796

All rights reserved

INFORMATION TO ALL USERS

The quality of this reproduction is dependent upon the quality of the copy submitted.

In the unlikely event that the author did not send a complete manuscript and there are missing pages, these will be noted. Also, if material had to be removed, a note will indicate the deletion.



ProQuest 10837796

Published by ProQuest LLC (2018). Copyright of the Dissertation is held by the Author.

All rights reserved.

This work is protected against unauthorized copying under Title 17, United States Code
Microform Edition © ProQuest LLC.

ProQuest LLC.
789 East Eisenhower Parkway
P.O. Box 1346
Ann Arbor, MI 48106 – 1346

Abstract

Over the past thirty years, a detailed picture of star formation has emerged that highlights the significance of the interaction between a pre-main sequence star and its protoplanetary disk. This star-disk interaction has been extensively characterized in the case of single stars, revealing implications for pre-main sequence stellar evolution and planet formation. Many stars, however, form in binary or higher-order systems where orbital dynamics fundamentally alter this star-disk interaction. Divergence from the single-star paradigm is most extreme in the case of short-period binaries where orbital resonances are capable of clearing out disk material on size scale of the binary separation. Under these conditions, streams of material driven by the binary orbit are predicted to periodically cross this cleared gap, linking a circumbinary disk to the inner binary. These streams may feed circumstellar disks or accrete directly onto the stars themselves, leading to bursts of accretion during each orbital period.

In this thesis, I observationally characterize the binary-disk interaction in two short-period, eccentric systems, DQ Tau and TWA 3A. This is achieved through long-term monitoring campaigns that combine multiple observational probes of stellar accretion. For each source a time-series, optical photometry campaign provides a foundation for this work by measuring accretion diagnostics ~ 20 times per orbit for ~ 10 orbital periods. For DQ Tau, these data are supplemented with stretches of high-cadence, optical photometry that capture the detailed morphology of accretion events. In the case of TWA 3A, the addition

of time-series, high-resolution optical spectroscopy provides a new lens on the kinematics of the stellar accretion flows.

The results of these campaigns reveal an intimate link between stellar accretion and the binary orbit. Both systems exhibit consistent bursts of accretion near their periastron passages that are in reasonable agreement with the predictions of numerical simulations. With the addition of kinematic information via spectroscopy, circumbinary accretion flows are found to preferentially feed the TWA 3A primary star. This is in contrast to the prediction of most numerical simulations and may point to the importance of secular interactions between the binary potential and the circumbinary disk. With the three observational studies presented in this thesis I provide a comprehensive characterization of binary accretion in eccentric systems. These results mark a significant step forward in our understanding of the binary-disk interaction and carry implications for star and planet formation in the binary environment.

To my parents

Acknowledgments

There are too few opportunities in life to reflect upon the people and things you are thankful for in as direct a setting as the acknowledgment section of your PhD thesis. As my time in graduate school draws to a close, I am grateful to have these pages to express my thanks to those who helped me reach this stage, weather its hard times, and celebrate its good times. It is difficult to express what these past years in Madison have meant to me, definitely more than another “step along the way”, and with the support of the following people these years have become some of the most influential in my life.

As a research document, I must begin by thanking those who most directly made this work possible. First and foremost is my advisor, Bob Mathieu. Bob, your unwavering encouragement, enthusiasm, and patience has made for an exciting and supportive research environment. You have given me the freedom to find my own identity in this field and have supplied me with every opportunity to become a part of the scientific community. Your thoughtful mentorship in research and teaching has continually challenged and expanded my view on both. You have also introduced me to an amazing group of collaborators who have greatly improved the research presented in this thesis. Greg Herczeg, Rachel Akeson, Chris Johns-Krull, and David Ardila, thank you for your time, your encouragement, and your guidance these past years.

I also have to thank the amazing research group which I had the opportunity to be a part of in grad school. Natalie and Katelyn, you showed me the ropes those first few years

and helped foster a supportive and collaborative research group. Max and Erika, thanks for providing a new shot of life into the group and for thoughtful discussions that can only come explaining your work to someone new. And Emily, I am truly lucky to have you as a contemporary and a friend. You are a great scientist and having you as a partner in the job hunt and defense season has made life this past year infinitely more bearable.

Stepping back, there are a number of people I have to acknowledge who made graduate school a possibility for me. The first are my parents. You have supplied me with every imaginable opportunity growing up, and instilled in me that “snake-killing” attitude. I am truly fortunate to be your son.

Next is my undergrad research advisor, John Wisniewski. John, your confidence in me was the first step down this path and for that, I am very grateful. Thanks for being a constant source of support in my career and my life, and for showing me the fun, ridiculous, and occasionally shark-infested side of astronomy.

And to Blakesley, I *literally* would not be a graduate student at UW-Madison if it were not for your advocacy. Thank you for showing me what grad school at UW-Madison is all about, for being a great mentor, and for introducing me to the Plaza. But most of all, thank you for putting yourself out there for me.

The astronomy graduate students I’ve had the pleasure of overlapping with these past years are a special group of people. I have been lucky to be a part of a community that made life bearable in the worst times and unforgettable in the best times. The following people helped me keep my sanity when needed and lose it at just the right times. Jenna, Chris, and John, you guys made my first year feel like home and the department feel like a family. Arthur, my grad mentor and all around legit dude, I don’t think there will ever be a time where I am not surprised by what you say and do, but your view on the world has been a constant expansion of my own. I can’t image grad school or what comes next

without you somewhere in the mix. And David, you have always been there with a friendly ear, an excellent music suggestion, and the ability to cut through the malarkey that often comes with grad school. Thanks for always being there.

I also have to acknowledge my excellent office mates, Andrew and Stephen. Andrew for always telling it to me straight and for teaching me early how to be a jaded grad student. And to Stephen, my plot consultant, for putting up with my convoluted python questions and for caring about doing things the right way.

And of course, I have to acknowledge my soul classmate, Claire. Co-member of the class that brought the classes together. Claire, unfortunately, the conditions under which I was admitted to this department left a chip on my shoulder that I could seemingly only fill by trying to be better than you. This was no short order as you are one of most talented and hardworking people I know. I can confidently say that you have made me a better scientist. I only hope this unspoken, and potentially one-sided, competition has benefited you too. You're great!

Outside of the astronomy department, the following groups of people helped me decompress and escape during grad school. First are The Begowatts: Arthur, David, Chris, Lydia, Dan, Aaron, Rob, and Tom. Playing tunes (tubes) with you doods has been one of the coolest things I have ever done. I am so thankful for the time we had writing, recording, road-tripping, and exploring the seedy underbelly of the midwest's music dives. Second are the Extragalacticos, especially Julian, Lisa, Josh and a number of those above, for having more heart than any other co-ed, social-league, indoor soccer team and for getting me off the couch during those long winter months. And last, my friends outside of academia. Hanna, Amie, Adam, Claire, and Denny, thanks for giving me a glimpse into the "real world" and for making me feel like a normal person.

Last, and above all else, I have to acknowledge my greatest source of support and encouragement, my partner in this crazy life we chose, my B, Katrina. You had the faith in me and in us to move across the country and start a life together. At the end of so many tough days along the way, you were there to make me laugh and melt away my stresses. During stretches of prelims, or proposals, or defending, when I had the tendency to let everything slide, you provided a stability that I can't imagine getting through grad school without. At the same time your own achievements personally and professionally have been a constant source of motivation for me. I am so proud of the life we have built together and while I don't know where it will take us, I am confident that there is nothing we cannot weather together.

Contents

Abstract	i
Dedication	iii
Acknowledgments	iv
Contents	viii
List of Tables	xii
List of Figures	xiii
1 Introduction	1
1.1 Star Formation	2
1.1.1 The Star-Disk Interaction	3
1.2 Binarity	8
1.2.1 Binary-Star Formation	9
1.2.2 The Binary-Disk Interaction - Theory	10
1.2.3 The Binary-Disk Interaction - Observations	15
1.2.4 Broader Impacts of the Binary-Disk Interaction	19
1.3 Outline of Thesis	20
References	22
2 Pulsed Accretion in DQ Tau	27
Abstract	28

2.1	Introduction	29
2.1.1	DQ Tau	32
2.2	Observations & Data Reduction	35
2.2.1	LCO 1m Network	36
2.2.2	WIYN 0.9m	37
2.2.3	ARCSAT 0.5m	38
2.2.4	Photometry	38
2.2.5	Photometric Calibration	39
2.3	Determining Optical Emission Mechanisms	41
2.3.1	Light Curve Characteristics	44
2.3.2	Stellar Flares	48
2.3.3	Colliding Magnetospheres	54
2.4	Characterizing Accretion	57
2.4.1	Periodic Enhanced Accretion	61
2.4.2	Accretion Variability	67
2.4.3	Apastron Accretion Events	71
2.5	Summary & Conclusions	72
	References	76
3	Pulsed Accretion in TWA 3A	82
	Abstract	83
3.1	Introduction	84
3.2	Observations & Data Reduction	86
3.2.1	LCO 1m Network	86
3.2.2	SMARTS 1.3m	87

3.2.3	Photometry and Calibration	87
3.3	Analysis	89
3.3.1	Light Curve Variability	89
3.3.2	Mass Accretion Rate	91
3.3.3	Accretion Periodicity	93
3.3.4	Accretion Rate Profile	94
3.4	Discussion	95
3.5	Summary	98
	References	100
4	Accretion Kinematics in TWA 3A	103
	Abstract	104
4.1	Introduction	105
4.2	The TWA 3 System	107
4.3	Observations & Data Reduction	111
4.3.1	SALT-HRS	111
4.3.1.1	HRS Red Arm-Specific Reductions	115
4.3.2	Archival Spectroscopic Observations	116
4.3.3	LCO 1m Network	116
4.4	Results	118
4.4.1	Equivalent Width Measurements	118
4.4.2	Spectral Line Velocity Structures	121
4.4.2.1	H Balmer Series	125
4.4.2.2	He I 5876 Å & 4471 Å	125
4.4.2.3	Ca II H & K	127

4.4.2.4	[O I] 6300 Å	127
4.4.2.5	Li I	130
4.4.2.6	Other Spectral Features of Note	131
4.4.2.7	Archival FEROS Observations: H α & He I 5876 Å	132
4.5	Discussion	132
4.5.1	Accretion and Chromospheric Emission	132
4.5.2	Preferential Accretion onto the TWA 3A Primary	138
4.5.2.1	Implication for the Accretion Stream Theory	140
4.6	Conclusions	145
4.7	Future Work	146
	References	149
5	Conclusions	155
	References	161
A	SALT–HRS Red-Arm Specific Reductions	162
A.1	SALT–HRS Red-Arm Specific Reductions	163
B	Gaia Distance Inference	166
B.1	Distance Inference from Gaia Parallax	167
	References	168
C	DQ Tau K2 Light Curve	169
C.1	DQ Tau K2 Light Curve	170
	References	171

List of Tables

2.1	DQ Tau System Summary	33
2.2	Flare Characterization Summary	53
3.1	TWA 3A System Characteristics	85
4.1	TWA 3A System Characteristics	109
4.2	Dates, Equivalent Widths, and Mass Accretion Rates for SALT-HRS Observations	114
4.3	Dates and Equivalent Widths of FEROS Observations	116

List of Figures

1.1	Schematic of a protoplanetary disk.	4
1.2	Numerical simulation of stable and unstable accretion in the magnetospheric accretion scenario.	6
1.3	Hydrodynamic simulations of binary accretion from Artymowicz & Lubow (1996).	12
1.4	Hydrodynamic simulations of circular and eccentric binary accretion from Muñoz & Lai (2016).	13
1.5	Mass accretion rates for the simulations presented in Figure 1.4	14
1.6	Spatially resolved circumbinary gap in the binary system GG Tau A.	17
1.7	V -band light curve of DQ Tau from Mathieu et al. (1997).	18
2.1	$UBVR$ light curves of DQ Tau spanning 10 orbital periods.	41
2.2	High-cadence U -band light curves of 4 separate DQ Tau periastron passages.	46
2.3	$U-R$ color-magnitude diagram of DQ Tau variability. Variability consistent with stellar flare events are highlighted.	48
2.4	An eight-hour, high-cadence, U -band light curve of DQ Tau during which two stellar flare candidates are present.	50
2.5	Modeling of the stellar flare candidates present in Figure 2.4.	51

2.6	Top: Time-resolved mass accretion rate measurements of DQ Tau spanning 10 orbital periods. Bottom: Integrated mass accreted over each full orbital period and each periastron passage.	60
2.7	Top: Orbital-phase-folded mass accretion rate measurements of DQ Tau. Bottom: Two Lomb-Scargle periodograms of the DQ Tau mass accretion rate. The first makes use of all observations while the second excludes a subset of apastron observations with high-accretion.	62
2.8	The DQ Tau orbit-averaged mass accretion rate as a function of orbital phase derived from 10 orbital cycles of observation.	64
2.9	A comparison of the DQ Tau median mass accretion rate presented in Figure 2.8 with the results of a numerical simulation of eccentric binary accretion (Muñoz & Lai 2016).	65
2.10	A comparison of DQ Tau’s median accretion rate profile (as a function of orbital phase) with two orbital periods of drastically different accretion variability.	67
2.11	A $U-B$ color-magnitude diagram of DQ Tau accretion variability.	70
3.1	$UBVR$ light curves of TWA 3 spanning ~ 14 orbital periods over 3 observing seasons.	89
3.2	B -band light curve of TWA 3A and TWA 3B, highlighting TWA 3A as the source of system’s variability.	90
3.3	Top: Orbital-phase-folded mass accretion rate measurements of TWA 3A. Bottom: Lomb-Scargle periodogram of the TWA 3A mass accretion rate.	94

3.4	Top: The TWA 3A orbit-averaged mass accretion rate as a function of orbital phase derived from ~ 14 orbital cycles of observation. Bottom: A comparison of the TWA 3A median accretion rate profile (as a function of orbital phase) with DQ Tau's and a numerical simulation of binary accretion (Muñoz & Lai 2016).	96
4.1	Overview of our LCO photometric and SALT–HRS spectroscopic time-series monitoring campaign of TWA 3.	112
4.2	Equivalent widths of accretion-tracing emission lines as a function of the TWA 3A orbital phase.	120
4.3	Velocity structure of TWA 3A Balmer emission lines H α and H β	122
4.4	Velocity structure of TWA 3A Balmer emission lines H γ and H δ	123
4.5	Velocity structure of TWA 3A Balmer emission line H ϵ	124
4.6	Velocity structure of He I emission lines in TWA 3A.	126
4.7	Velocity structure of Ca II H and K emission lines in TWA 3A.	128
4.8	Velocity structure of [O I] 6300 Å in TWA 3A.	129
4.9	Velocity structure of Li I 6707 Å in TWA 3A.	131
4.10	Velocity structure of H α and He I 5876 Å from archival observation of TWA 3A.	133
4.11	Equivalent width of He I 5876 Å as a function of the H α equivalent width for TWA 3A.	135
4.12	Equivalent widths of accretion-tracing emission lines as a function of the mass accretion rate for TWA 3A.	136

4.13	A comparison of two epochs of He I 5876 Å emission that highlight the dominant emission from TWA 3A primary in the presence of high accretion rates.	139
4.14	Doppler tomography of He I 5876 Å emission in TWA 3A.	141
A1	Demonstration of SALT-HRS red-arm slit image distortions and their correction.	164
C1	K2 light curve of DQ Tau.	170

Chapter 1

Introduction

*And the first lesson of all was the
basic trust that he could learn.*

Princess Irulan

With this thesis I aim to address a set of open questions in an important domain of our broader understanding of star formation. Taken in itself, the results presented here describe the behavior of two young binary star systems as they interact with their surrounding protostellar disks. Set in a larger context, these findings carry implications for the formation of binary stars, the formation of planets around them, and for the orbital evolution of accreting binary systems, stellar or otherwise. This introduction serves to provide that context. I begin with a summary of star formation where it is best understood - the case of single stars - focusing particularly on the interconnection of stars with their circumstellar material. A discussion of binarity and its effect on star formation then follows. In the final section of this chapter, I outline the three observational studies that comprise this thesis.

1.1 Star Formation

The formation of isolated single stars begins in the coldest and densest regions of giant molecular clouds. The collapse of these molecular cloud cores requires the aid of an external process to push this region, which is initially in pressure equilibrium, into a regime that is unstable to gravitational collapse. Whether this process is internal to the cloud itself through turbulent flows (Matsumoto et al. 2015), or requires some external driver (e.g. galactic spiral density waves (Shu 2016) or stellar feedback (Rey-Raposo et al. 2017)), the collapse of these structures marks the start of the star-formation process. This initial collapse of ~ 0.1 pc-sized structures takes place on roughly a “free-fall” timescale occurring over $\sim 10^4$ years.

From this point, the evolutionary pathway of a forming star is dependent on its mass. Formation scenarios are typically broken into two regimes based on the star’s final mass, with the division at $M_{\star} \sim 8M_{\odot}$ (Motte et al. 2017). In the high-mass regime, a massive

protostar reaches hydrostatic equilibrium with a high enough radiation pressure to begin immediately clearing out its surrounding envelope (Krumholz et al. 2005). Whether a circumstellar disk develops or has any serious implication on the formation of the star in this case is unclear. The timescale for reaching the main sequence at these high masses can be as short as 10^5 years, making this phase of star formation difficult to observe (Russeil et al. 2010).

In the case of lower-mass single stars, however, a much more well-established theory exists, aided by longer evolutionary timescales and more observational constraints. In this case, the collapsing core forms a flattened disk of material around a central protostar through the conservation of the cloud's initial angular momentum and the dissipative (collisional) properties of gas. At the earliest stages, the assembly of a rotationally supported disk occurs while a dense envelope enshrouds the central protostar; with far-IR and sub-mm observations, evidence for disk material is beginning to be found in sources with ages $\sim 10^5$ years (Murillo et al. 2013).

1.1.1 The Star-Disk Interaction

The evolution of a young, low-mass star toward the main sequence becomes intimately linked to the evolution of this surrounding material. Figure 1.1 presents a schematic of a star-disk system listing relevant scales and their corresponding observational probes (Dullemond & Monnier 2010).

The most direct and consequential interaction between the star and disk takes place at the boundary of the innermost gaseous disk and the star's magnetic field. This interaction is driven by two main ingredients. First, that pre-main sequence (pre-MS) stars have strong stellar magnetic fields. Being fully convective at this stage leads to vigorous dynamo motion that can amplify and sustain a strong magnetic field (Browning 2008). And second, that

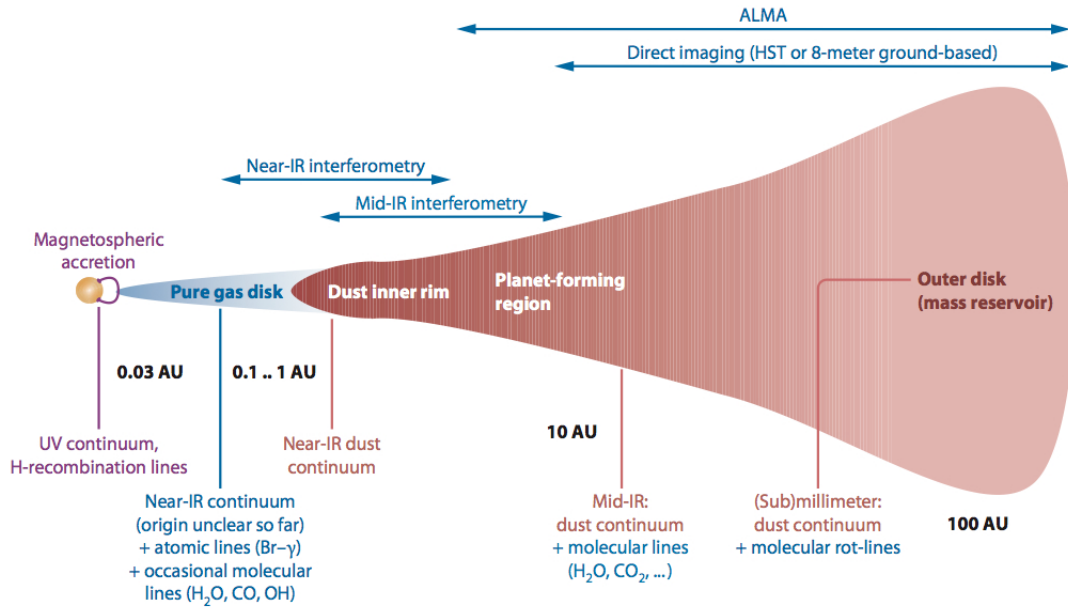


Figure 1.1 A schematic of a protoplanetary disk. Relevant regions are highlighted with their corresponding observational probes (Dullemond & Monnier 2010).

disk material viscously accretes radially inward. The mechanism by which this viscosity operates and is able to transport angular momentum remains a topic of active research. Turbulence from magnetorotational (Balbus & Hawley 1998) or vertical shear (Nelson et al. 2013) instabilities have shown promise in certain regions of a disk, but a global solution at all radii has proven elusive. An alternative mechanism may be the launching of material (and with it angular momentum) along magnetic fields that thread the disk vertically in a magneto-centrifugal wind scenario (Blandford & Payne 1982). Whatever the mechanism, mass accretion is observed at steady rates as high as $\sim 10^{-6} M_{\odot} \text{ yr}^{-1}$ at early ages (Muzerolle et al. 1998).

This inward flow of disk material applies a pressure on a star’s magnetic field, deforming it, until an equilibrium is reached between the star’s magnetic pressure and the ram pressure of accreting material. At this point the magnetic field is capable of truncating circumstellar disk material. Residing at ~ 5 stellar radii for typical magnetic

field strengths and accretion rates (Johnstone et al. 2014), material inside this boundary is then funneled along magnetic field lines before impacting the stellar surface at magnetic foot-points. At near free-fall velocities, these flows create standing shocks that give rise to the classical signatures of stellar accretion: strong H Balmer line and continuum emission, UV and X-ray emission, and continuum veiling of photospheric absorption lines (Hartmann et al. 1994; Gullbring et al. 1998).

Figure 1.2 presents a 3D magnetohydrodynamic simulation of this magnetic accretion scenario from Romanova et al. (2008). The left panel presents a stable accretion regime where disk material continuously flows along magnetic field lines. While stable accretion models are able to reproduce the instantaneous observed properties of stellar accretion, they are not able to describe its variability. Variability is indeed one of the defining characteristics of accreting systems (e.g. Cody et al. 2014; Stauffer et al. 2014; Sousa et al. 2016). The right panel of Figure 1.2 displays one attempt to explain this variability. In this “unstable” accretion scenario, Rayleigh-Taylor instabilities allow for transient flows to pass through the classical boundary, accreting more chaotically via interior magnetic field lines that impact the stellar surface at lower latitudes.

This complex interaction between the star and disk takes place over the gaseous disk’s lifetime, lasting on the order of 10 Myr (Williams & Cieza 2011). Many characteristics of the star are set by this interaction, while at the same time shaping the evolution of the disk. For the star, this interaction acts as an avenue for continued mass growth that may be capable of supplying up to half of a star’s final mass (Baraffe et al. 2012). The timing and amplitude of the delivery of this mass is also relevant. Tying back to the accretion variability above, large bursts of mass accretion as opposed to a steady flow are predicted to affect the contraction timescales for young stars (Enoch et al. 2009; Evans et al. 2009; Baraffe et al. 2012). Additionally, “locking” between the star’s magnetic field and the inner

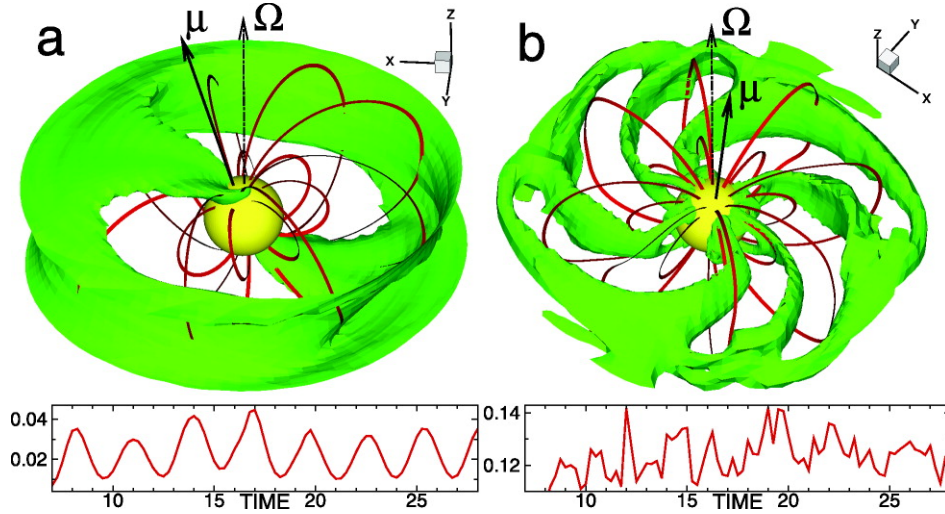


Figure 1.2 Results of a magneto-hydrodynamic simulation depicting the accretion of disk material along stellar magnetic field lines (Romanova et al. 2008). On the left (a) is a model of stable accretion. On the right (b), Rayleigh-Taylor instabilities lead to unstable, stochastic accretion. The bottom panels present the rotationally modulated light curves of the respective accretion hot spots.

disk can act as an angular momentum sink that torques the star, limiting its spin up during contraction (Shu et al. 1994).

For the disk, accretion processes, in part, set the disk’s lifetime. In addition to direct consumption onto the star, the magnetospheric interaction with the disk can drive outflows through jets and winds. At the same time, high-energy radiation from stellar accretion shocks can photoevaporate the upper layers of the disk. As the dust grains grow and settle in the disk midplane, this radiation can be important for the chemical properties of the disk (Alexander et al. 2014). As these processes exhaust a disk’s gas supply, this direct interaction with the central star ceases, leaving a dusty debris disk that is slowly expelled through radiation pressure.

Each of the processes that shape the evolution of the disk are also vital ingredients for planet formation. Lifetimes and disk chemistry are of particular relevance. While our understanding of planet formation is much less developed than star formation, the star-disk

interaction predicts a relatively stable environment for grain settling and growth.

From an observational perspective, the evolution of sources through this phase of star formation can be broken into four classes based on the spectral slope of their mid-infrared (MIR) emission, α_{IR} (spectral index; typically between 2.2 and 10 μm). This emission probes thermal disk emission and reprocessed stellar light in the case of embedded systems (Evans et al. 2009). As this nomenclature is used throughout this thesis, I present a summary of it here. Beginning with the youngest sources ($t \sim 10^5$ yr), Class 0 sources are heavily embedded, so much so that they have no MIR detections. It is only possible to probe such sources in the far-IR and sub-mm.

Next are Class I sources ($t \sim 1$ Myr), defined as having positive MIR spectral indices. These sources are still heavily embedded and are typically not probed at optical wavelengths. SED modeling in these systems and NIR line emission, however, suggest high accretion rates (Muzerolle et al. 1998).

Class II sources are defined as having negative spectral indices with $\alpha_{\text{IR}} > -1.5$. By this stage of evolution ($t \sim \text{few Myr}$), most envelope material has been cleared allowing for studies at optical wavelengths. These systems are commonly referred to as classical T Tauri stars (CTTSs), and are the main source of our observational constraints on the star-disk interaction. Here, the stellar photosphere can be easily probed allowing for the earliest determination of stellar properties (e.g. $\log g$, T_{eff}), and the characterization of stellar accretion through strong emission lines and UV excesses. Accretion rates in this phase range from 10^{-6} to $10^{-11} M_{\odot} \text{ yr}^{-1}$ at the lowest detectable limits.

Last are Class III sources with spectral indices $\alpha_{\text{IR}} < -1.5$ ($t \sim 10$ Myr). Referred to as weak-lined T Tauri stars, these systems are no longer accreting disk material, but maintain weak levels of line emission from active chromospheres and host dusty debris disks.

The description of single-star formation presented here represents over thirty years of detailed theoretical and observational studies. While the success of the current paradigm is indeed one of the most significant achievements in modern astrophysics, it is far from complete. And nowhere is this more the case than in the consideration of environment. Our current view is one of relative isolation, while it is well known that stars form in a range of environments, from loose associations to dense clusters. At the extreme of this spectrum is the case of stellar companions.

1.2 Binarity

Binary stellar systems are a common outcome of the star-formation process (Raghavan et al. 2010). In the last decade, large advances have been made in our understanding of binary populations through massive surveys of main-sequence stars in the solar neighborhood and in open clusters. Through Herculean efforts combining both high-angular-resolution imaging and high-spectral-resolution spectroscopy in time series, these studies reveal the ubiquity of multiplicity across all stellar masses. The binary frequency is observed to increase with the mass of the primary star, with binary frequencies of $\sim 30\%$ in low-mass systems (M dwarf primaries; Ward-Duong et al. 2015), which rises to $\sim 40\%$ for solar mass stars, and reaches $>90\%$ for the highest mass stars (Moe & Di Stefano 2017).

At younger ages, our census of binaries is much less complete. As we have seen, young stars are typically embedded, which only allows for the detection of widely separated systems. By the Class II phase, the detection of binaries with high-angular-resolution observations becomes more feasible. Detecting spectroscopic binaries in Class II sources, however, remains difficult due to high levels of absorption line veiling that prevent precise radial-velocity measurements. Only very short-period systems ($P \lesssim 100$ days), with high-

amplitude radial-velocity variability have been found, and even then, they are typically in systems with low accretion rates (Mathieu 1994; Prato et al. 2002). This limitation vanishes by Class III sources where large populations of pre-MS binaries are being found at all separations (Reipurth & Zinnecker 1993; Duchêne et al. 2004; Prato 2007).

The pervasiveness of binary systems at all masses and ages emphasizes the need to characterize this mode of star formation and reveals the relative infancy of current theory compared to single-star formation. Binary-star formation and particularly the effects of binaries on the star-disk interaction is a frontier of star-formation research.

1.2.1 Binary-Star Formation

Beginning with the consideration of a single molecular cloud core, binary stars are believed to form by two main pathways: core fragmentation and disk fragmentation. In the initial collapse, high levels of rotation or turbulence can lead to core fragmentation (Goodwin et al. 2007). Depending on the initial conditions of the core, this process is able to produce binaries at a variety of initial separations (1000s of AU to ~ 1 AU scales; Machida et al. 2008).

Disk fragmentation occurs at later times and on smaller spatial scales. In this scenario, massive disks become gravitationally unstable and fragment on < 100 AU scales. This mechanism is thought to operate most efficiently in low mass systems where, at early times, the disk mass and central stellar mass are near equal (Meyer et al. 2018).

A third binary formation pathway that nods to the clustered environment of star formation is via the dynamical decay of triple or higher order multiple systems. In this scenario, a highly fragmented cloud core or group of gravitationally bound cores forms in an initially unstable configuration that stochastically decays. In the case of an initial triple, on average this process ejects the lowest mass component leaving in a close binary

(Reipurth 2000; Reipurth & Clarke 2001).

The fragmentation or decay timing, initial separation, and orbital parameters that result by either mechanism above can have a substantial impact on the subsequent evolution of the system. Most notably, binaries have the ability to alter the canonical star-disk interaction.

1.2.2 The Binary-Disk Interaction - Theory

The degree to which the binary-disk interaction deviates from single stars is most dependent on binary semi-major axis (a). Here we can break binaries up into three regimes based on their separation with respect to the typical protoplanetary disk size (~ 100 AU; Ansdell et al. 2018).

For wide separations ($a \gtrsim 300$ AU), the effect of binarity is minimal. Each star can possess a “full sized” disk that, other than longterm precession from the binary potential, will proceed in its pre-MS evolution similar to that of a single star. Binaries with these wide separations can be easily spatially resolved where large individual disks are observed. Many of these disk pairs are also not coplanar, further highlighting their

At intermediate separations ($300 \gtrsim a \gtrsim 50$ AU), the binary orbit will begin to truncate the outer regions of each star’s protoplanetary disk. This should lead to smaller disks that are exhausted on shorter timescales than in single stars. Surveys of disk frequency and disk mass for binaries with these separations confirm this general effect (Williams & Best 2014; Kraus et al. 2016). Aside from changes to the disk’s evolutionary timescale, the processes that govern the interaction between each star and its disk on small scales should be preserved.

In the smallest separation regime ($a \lesssim 50$ AU), the effect of binarity on the star-disk interaction becomes the most extreme. In coplanar systems, Lindblad and co-rotational

resonances prevent the orbit of stable disk material on scales of $1-3a$, significantly altering the distribution of disk material (Lin & Papaloizou 1979). Under the influence of the binary, a specific disk architecture is predicted where an extended circumbinary disk surrounds the close pair, each of which may possess their own small circumstellar disk.

Early theoretical efforts to describe this binary-disk interaction predicted that orbital resonances would completely dam the viscous accretion of the outer disk. Small circumstellar disks would then be exhausted on short timescales, greatly decreasing the length of the accretion phase in short-period binaries. In the mid-1990’s, however, the discovery of short-period spectroscopic binaries with accretion rates similar to that of single stars prompted a reevaluation of the binary-disk interaction (Mathieu 1994; Jensen et al. 1996; Mathieu et al. 1997). Notably, several of these binary systems were exemplars of the observational studies that supported the development of single-star-disk interaction theory.

In the seminal work by Artymowicz & Lubow (1996), a much more dynamic view of the binary-disk interaction was introduced that would become the cornerstone of binary accretion theory. In their early simulations these authors showed evidence for time-variable accretion flows from the circumbinary disk that would cross the dynamically cleared gap to periodically feed the central binary. Figure 1.3 presents two snapshots from their initial simulation highlighting the dynamically driven streams. These streams were shown to produce enhanced accretion events giving this set of predictions the name, the binary “pulsed” accretion theory. Many subsequent studies have refined this theory but the disk architecture and the presence of pulsed accretion streams have remained.

The specific frequency of these accretion streams and their interaction with the central binary depend most heavily on the binary eccentricity. For equal-mass systems, a break in the predicted behavior takes place at low eccentricities ($e \lesssim 0.05$; Miranda et al. 2017). In the high eccentricity case, stream behavior is driven by the binary orbit. For even small

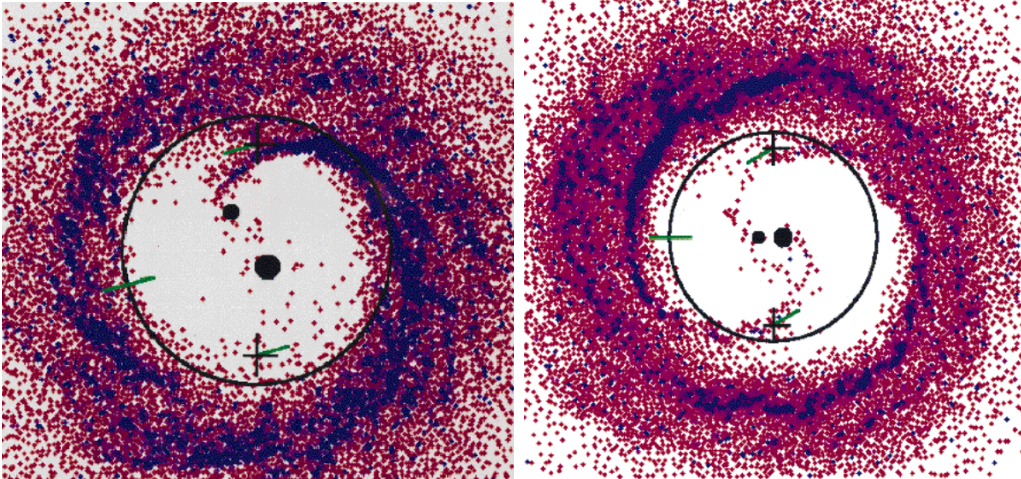


Figure 1.3 Two snapshots from the seminal 2D hydrodynamic simulations of binary accretion by Artymowicz & Lubow (1996). The left panel is for a $q=0.42$, $e=0.1$ binary at $\phi=0.75$. The right panel is for a $q \sim 1$, $e=0.5$ binary.

eccentricities streams are predicted to draw in circumbinary material every orbital period as the binary traverses its apastron passage. These flows supply a periodic replenishment to the circumstellar disks. Simulations of eccentric systems predict bursts of accretion near each periastron passage as each star applies a tidal torque on its companion's disk. This torque induces $m=2$ spiral modes in each circumstellar disk that aid in the outward transport of angular momentum, fueling a burst of accretion near periastron passage. The amplitude of these bursts scales with the binary eccentricity increasing the specific accretion rate by a factor of ~ 10 for $e \sim 0.5$.

Figure 1.4 presents snapshots from 2D adaptive-mesh hydrodynamic simulations of binary accretion (Muñoz & Lai 2016). The bottom panels display four orbital phases of an equal-mass binary with an eccentricity of 0.5. Here, as in the panels above for a circular binary, stream material is readily visible across the dynamically cleared gap. The top panel of Figure 1.5 presents this binary's combined mass accretion rate where sharp burst in the accretion rate are observed near each periastron passage.

For binaries with nearly circular orbits, accretion variability is driven more by the

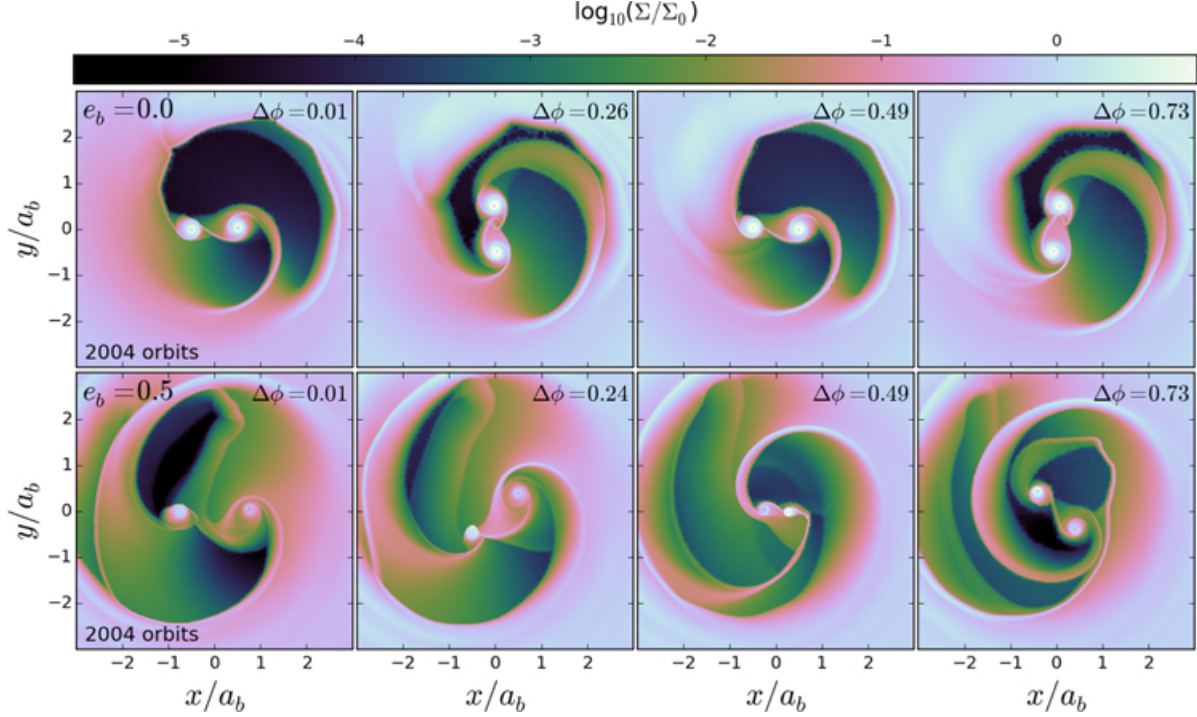


Figure 1.4 2D hydrodynamic simulations of binary accretion (Muñoz & Lai 2016). The top panels are four snapshots from an equal-mass, circular binary. The bottom panels are for an equal-mass binary with an eccentricity of 0.5. In this representation, $\Delta\phi = 0$ corresponds to apastron.

properties of the disk. In this case, accretion streams spur from a buildup of material over the course of the inner disk orbital timescale (typically ~ 5 binary orbital periods). This buildup becomes unstable and flows inward replenishing the circumstellar disks, yielding a saw-toothed variable accretion pattern over ~ 5 binary orbital periods with an amplitude of ~ 2 times the quiescent accretion rate.

The top panels of Figure 1.4 present results for a circular, equal-mass binary. The third panel from the right ($\Delta\phi = 0.49$) depicts the radial decay of an over-dense region of the circumbinary disk. The bottom panel of Figure 1.5 presents the stellar mass accretion rate of this simulation as a function of time over 60 binary orbits.

Outside of equal-mass binaries, systems with modest mass ratios are expected to follow the same basic behavior described above. Predictions for the temporal variation

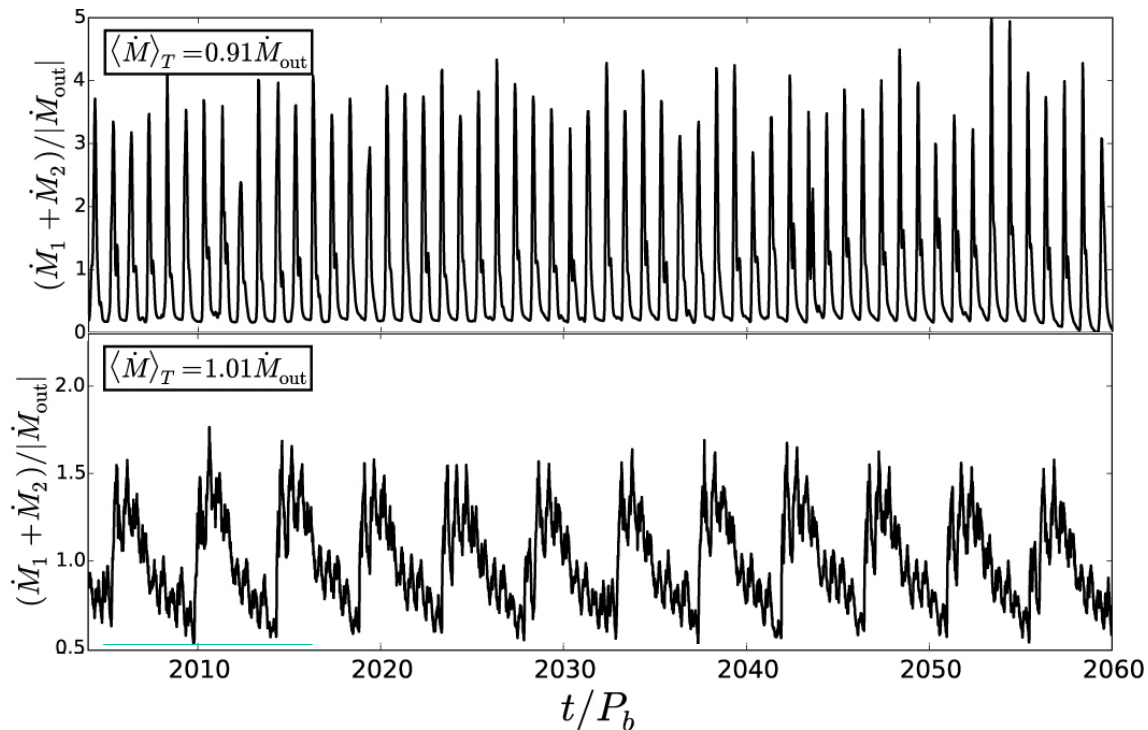


Figure 1.5 Binary accretion rate for simulations presented in Figure 1.4 (Muñoz & Lai 2016). The top panel is for an equal-mass binary with an eccentricity of 0.5 (bottom panel of Figure 1.4). The bottom panel is for an equal-mass, circular binary (top panel of Figure 1.4). Accretion rate values are normalized to the input accretion rate at the simulation boundary.

of the stellar accretion rate are comparable. Notably though, most simulations suggest that the circumsecondary disk will be preferentially fed by the accretion streams. In simulations, this preferential accretion results from a closer match between the specific angular momentum of inner disk material with the secondary star rather than the primary star. Requiring less angular momentum loss to be accreted on to the secondary (or its disk), stream material more readily does so. The ratio of mass accreted onto each component of the binary is predicted to depend on the “temperature” of the disk material - its thermal sound speed with respect to binary orbital speed. Higher disk temperatures increase the supply to the primary but only to level of $\sim 40\%$ of the secondary in extreme cases (Young et al. 2015; Young & Clarke 2015).

At more extreme mass ratios, $q \lesssim 0.1$, this description of the binary-disk interaction begins to break down. The ability to open a cleared region around both stars gradually decreases with q until a scenario more closely resembling an orbiting Jovian planet develops. Many of the processes that govern planet formation and migration processes become relevant in this regime but are beyond the scope of this current work.

The last ingredient that is relevant for this discussion of the binary-disk interaction in the short-period regime is the binary semi-major axis. For binary separations larger than $\sim 100 R_\star$ the description above is most likely to provide an accurate representation. At the very smallest separations, however, the interplay of stellar magnetic fields and orbital dynamics can begin to play an important role in the stability and even the existence of circumstellar disks.

A binary orbit will dynamically truncate the outer part of a circumstellar disk at $\sim 0.2a$ depending on the orbital parameters (Eggleton 1983; Miranda & Lai 2015). At the same time, a star's magnetic field will truncate the inner edge of the disk at $\sim 5 R_\star$. With smaller semi-major axes the ability for circumstellar disks to collect incoming stream material and fuel accretion events via tidal torques will also diminish. At the smallest separations each star's magnetosphere will overlap, excluding the possibility for any stable circumstellar material. Incoming stream material at these separations may involve a direct and complex interaction with stellar magnetic fields. Current simulations have not ventured in to this regime, and none have included stellar magnetism. The timing and amplitude of the predicted accretion events in very close binary systems remains largely unknown.

1.2.3 The Binary-Disk Interaction - Observations

Pulsed accretion streams were discovered almost simultaneously by observers and theorists (Artymowicz & Lubow 1996; Mathieu et al. 1997). However, today our under-

standing of binary-disk interactions sits on a much stronger theoretical than observational footing. Computing capabilities in the last decade have outpaced our ability to detect and characterize accretion in short-period binary systems. This lag mainly hinges on the lack of facilities that can provide long-term observations that span many binary orbital periods at a high sampling rate. Still, there is strong observational evidence for certain aspects of the binary-disk interaction.

Foremost is observational evidence for cleared gaps around close binary systems. This can be seen most dramatically in the polarized-light image of GG Tau A presented in Figure 1.6 (Yang et al. 2017). This image reveals extended emission around each component of GG Tau A, residing within the cleared gap of a circumbinary disk. Above the secondary, GG Tau Ab, there is evidence for stream material that looks remarkably similar to the simulations in Figure 1.4. A circumbinary disk has also recently been spatially resolved around the protostellar binary system IRAS17216-3801 (Kraus et al. 2017). And for unresolved binaries, the spectral energy distributions of their disk emission are usually best fit with an inner disk gap (Jensen & Mathieu 1997).

While support for predictions of the architecture of disk material in binary systems has grown, the temporal predictions have proven more difficult to test. Efforts to confirm the predictions of pulsed accretion have found the most success in time-series photometry of Class II binaries with short orbital periods. Orbital phase modulated accretion signatures were first observed in DQ Tau ($P=15.8$ days; $q=1$; $e=0.6$), which showed increases in broadband luminosities at many periastron passages, just as the simulations of Artymowicz & Lubow (1996) predicted (Mathieu et al. 1997). Figure 1.7 presents the DQ Tau V -band light curve in which many periastron passages (shown as horizontal line segments) are seen to brighten significantly. It was of note though that not every periastron passage produced increased luminosity.

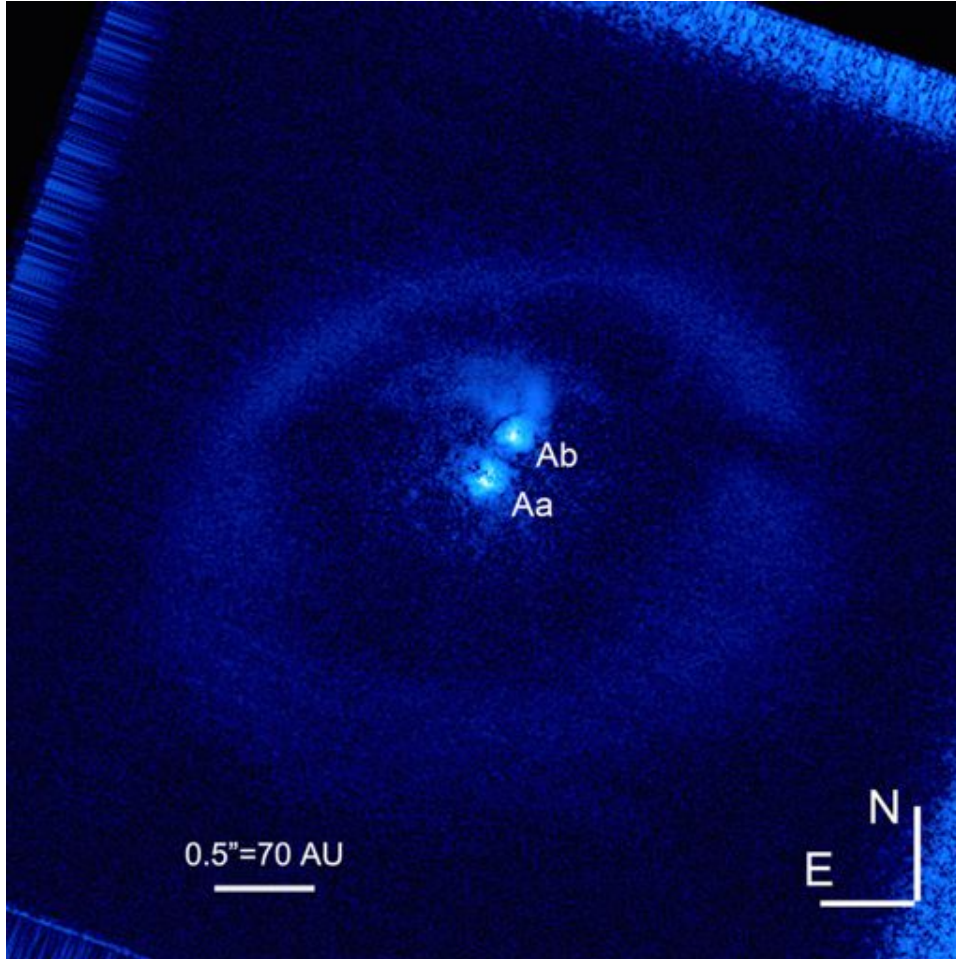


Figure 1.6 Polarized-difference image of GG Tau A tracing starlight scattered off dust grains. Adapted from Yang et al. (2017).

Subsequently, the Class II binary UZ Tau E ($P=19.1$ days; $q=0.3$; $e=0.3$) was found to exhibit periodic, sinusoid-like brightness variations over its orbital period in good agreement with predictions from simulations with similar orbital parameters (Jensen et al. 2007). Phase modulated accretion was searched for unsuccessfully, however, in the PMS binaries AK Sco ($P=13.6$ days; $q=1$; $e=0.5$; Alencar et al. 2003) and V4046 Sgr ($P=2.4$ days; $q=1$; $e=0$; Mekkaden 2000).

Moving beyond photometric studies, spectroscopy began to reveal the spatial distributions, kinematics, and fluxes of accretion flows. In the IR, Carr et al. (2001) were able to establish the presence of accreting material in the cleared gap of DQ Tau using the emission

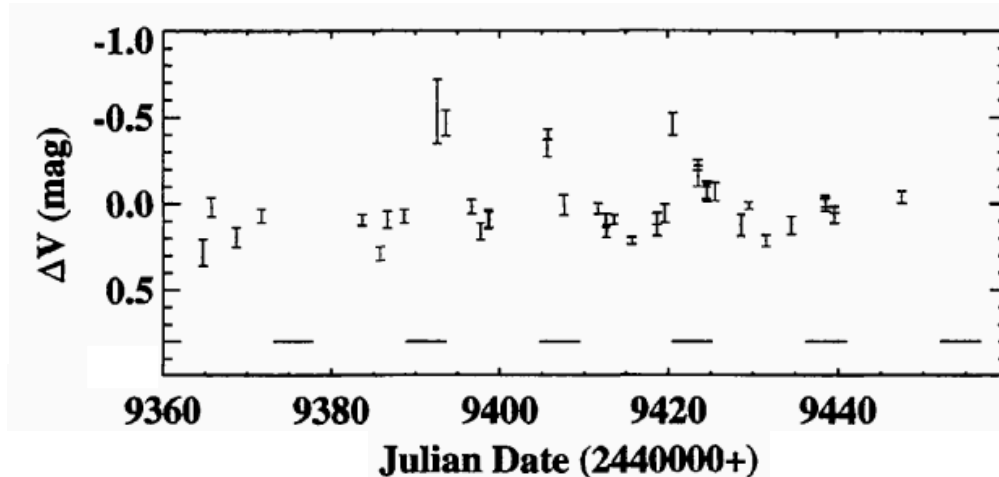


Figure 1.7 V-band light curve of DQ Tau ($P=15.8$ d; $q=1$; $e=0.56$). Enhanced emission near periastron, marked with horizontal line segments, was interpreted as enhanced accretion. This behavior is in good agreement with the pulsed accretion theory for eccentric binaries. Adapted from Mathieu et al. (1997).

of CO ro-vibrational lines. Similarly, Beck et al. (2012) used ro-vibrational emission of H_2 to characterize circumstellar material in the resolved gap of GG Tau A.

At shorter wavelengths, high-resolution, time-series spectroscopic studies have proven difficult to interpret due to the large intrinsic variability of CTTSs. DQ Tau and AK Sco, both eccentric binaries, have shown spectroscopic evidence for enhanced periastron accretion via line emission in the optical (Basri et al. 1997) and UV (Gómez de Castro et al. 2013), respectively. Interpreting these complex line structures strictly in terms of the accretion stream theory, however, has been challenging. A notable study by Stempels & Gahm (2004), however, has provided some interpretation of $H \alpha$ line emission in the short-period, circular binary V4046 Sgr. These authors modeled dramatic variations in the $H \alpha$ line width as gas in the cleared gap co-rotating with the stars themselves.

The main challenge facing all of these works is in extracting periodic signals from the stochastic variability that is intrinsic to the accretion process. Finding this signal only becomes more difficult at lower orbital eccentricities where accretion events are predicted

to have lower amplitudes. Thorough studies require observations that span many orbital periods with a high sampling rate. A data set with these characteristics has yet to be obtained for any accreting binary system. While these studies have supplied intriguing support for the binary accretion theory, to date no clear observational picture of accretion flow dynamics has emerged.

1.2.4 Broader Impacts of the Binary-Disk Interaction

The interaction between binary stars and their disk material has the potential to be vastly different from single stars. These differences can affect pre-MS stellar evolution as well as the lifetime and stability of disk material.

For the stars, the more dynamic or perhaps shortened interaction with disk material, depending on the binary separation, is believed to limit the efficiency of magnetic disk-locking to regulate the star's angular momentum. This effect is seen observationally in young clusters where binaries are found to have systematically higher rotation rates than single stars (Douglas et al. 2017), even in wide systems where tidal synchronization is not a concern (Lurie et al. 2017). These stars subsequently reach the main sequence with higher rotation rates, correspondingly high magnetic fields, and potentially having experienced more mixing than their single counterparts.

For the disks, lifetimes may be significantly shortened compared to single stars, reducing the timescale and reservoir of material for planet formation. Kraus et al. (2016), for instance, find evidence that intermediate-separation binaries are less likely to host planets, supporting this view. For short-period binaries especially, disk material resides in a much more dynamic environment. The binary orbit is predicted to excite spiral waves that heat the circumbinary disk, pushing the location of snow-lines further from the star (Vartanyan et al. 2016). Given our limited understanding of planet formation, the degree

to which these motions help or hinder planet formation is unclear. Beyond the central regions, however, the orbits of planets are predicted to be generally stable in the presence of perturbations from the binary, the disk, and accompanying planets (Bromley & Kenyon 2015). And indeed a growing number of circumbinary planets are being found (Orosz et al. 2012; Kaib et al. 2013; Mugrauer et al. 2014).

The theory of binary accretion in short-period systems also has implications for binary orbital evolution. The excitation of spiral density waves in the circumbinary disk can act as an angular momentum sink for the binary and is predicted to shrink the orbital separation. Additionally, preferential feeding of the secondary can act to equalize the mass ratio and has been a proposed mechanism to explain the observed overabundance of stellar twins ($q > 0.95$) at small separations (Raghavan et al. 2010; Moe & Di Stefano 2017).

The evolution of binary orbital parameters through circumbinary accretion is of particular interest in light of recent gravitational wave detections from the merger of compact objects. Super-massive binary black holes mergers have yet to be detected, but their evolution in separation and mass ratio should probe similar physics as the young binaries discussed here. Indeed, the characterization of binary accretion in the pre-MS, where the binary orbital parameters are well constrained, may be an ideal avenue to test binary accretion generally.

1.3 Outline of Thesis

In the following chapters I set out to observationally test predictions of the binary pulsed accretion theory. These studies focus on two short-period, pre-MS binaries, both of which are eccentric, near-equal mass, and actively accreting from their circumbinary disks. The new insights provided in this thesis have been made possible through a coordinated, multi-site campaign combining nearly 500 hrs of observation from 11 telescopes on four

continents. It is only through this unique and extensive dataset that we are able to search for and draw out periodic trends in the stellar accretion rate, and measure the kinematics of accretion onto each star.

The results presented in this thesis are organized as follows:

- In Chapter 2 I present the results of our extensive photometric campaign to monitor DQ Tau. This study includes moderate-cadence, multi-band, optical photometry spanning ~ 10 binary orbital periods, supplemented with stints of high-cadence photometry near periastron passage. Within these data we search for evidence of periodic enhanced accretion events, characterize the morphology of accretion events, and determine the relative contribution of stellar flares to the broadband emission. From this study we are able to make the first direct comparison of orbital-modulated accretion rates with numerical simulations.
- In Chapter 3 I present the results of our time-series photometric study of TWA 3A. Long-term, multi-band, optical photometry spanning ~ 12 orbital periods provides the means to monitor accretion variability as a function of orbital phase. These results serve as an ideal comparison to DQ Tau and theory.
- In Chapter 4 I present the results of our time-series spectroscopic study of TWA 3A. Overlapping with the photometric study presented in Chapter 3, 15 SALT high-resolution spectra probe the timing and location of stellar accretion flows.
- Finally, in Chapter 5 I provide a summary of our findings, placing them collectively in context with our broader understanding of the binary-disk interaction.

References

- Alencar, S. H. P., Melo, C. H. F., Dullemond, C. P., et al. 2003, *A&A*, 409, 1037
- Alexander, R., Pascucci, I., Andrews, S., Armitage, P., & Cieza, L. 2014, *Protostars and Planets VI*, 475
- Ansdell, M., Williams, J. P., Trapman, L., et al. 2018, *ApJ*, 859, 21
- Artymowicz, P., & Lubow, S. H. 1996, *ApJL*, 467, L77
- Balbus, S. A., & Hawley, J. F. 1998, *Reviews of Modern Physics*, 70, 1
- Baraffe, I., Vorobyov, E., & Chabrier, G. 2012, *ApJ*, 756, 118
- Basri, G., Johns-Krull, C. M., & Mathieu, R. D. 1997, *AJ*, 114, 781
- Beck, T. L., Bary, J. S., Dutrey, A., et al. 2012, *ApJ*, 754, 72
- Blandford, R. D., & Payne, D. G. 1982, *MNRAS*, 199, 883
- Bromley, B. C., & Kenyon, S. J. 2015, *ApJ*, 806, 98
- Browning, M. K. 2008, *ApJ*, 676, 1262
- Carr, J. S., Mathieu, R. D., & Najita, J. R. 2001, *ApJ*, 551, 454
- Cody, A. M., Stauffer, J., Baglin, A., et al. 2014, *AJ*, 147, 82
- Douglas, S. T., Agüeros, M. A., Covey, K. R., & Kraus, A. 2017, *ApJ*, 842, 83
- Duchêne, G., Bouvier, J., Bontemps, S., André, P., & Motte, F. 2004, *A&A*, 427, 651
- Dullemond, C. P., & Monnier, J. D. 2010, *ARA&A*, 48, 205

- Eggleton, P. P. 1983, *ApJ*, 268, 368
- Enoch, M. L., Evans, II, N. J., Sargent, A. I., & Glenn, J. 2009, *ApJ*, 692, 973
- Evans, II, N. J., Dunham, M. M., Jørgensen, J. K., et al. 2009, *ApJS*, 181, 321
- Gómez de Castro, A. I., López-Santiago, J., Talavera, A., Sytov, A. Y., & Bisikalo, D. 2013, *ApJ*, 766, 62
- Goodwin, S. P., Kroupa, P., Goodman, A., & Burkert, A. 2007, *Protostars and Planets V*, 133
- Gullbring, E., Hartmann, L., Briceno, C., & Calvet, N. 1998, *ApJ*, 492, 323
- Hartmann, L., Hewett, R., & Calvet, N. 1994, *ApJ*, 426, 669
- Jensen, E. L. N., & Akeson, R. 2014, *Nature*, 511, 567
- Jensen, E. L. N., Dhital, S., Stassun, K. G., et al. 2007, *AJ*, 134, 241
- Jensen, E. L. N., Koerner, D. W., & Mathieu, R. D. 1996, *AJ*, 111, 2431
- Jensen, E. L. N., & Mathieu, R. D. 1997, *AJ*, 114, 301
- Johnstone, C. P., Jardine, M., Gregory, S. G., Donati, J.-F., & Hussain, G. 2014, *MNRAS*, 437, 3202
- Kaib, N. A., Raymond, S. N., & Duncan, M. 2013, *Nature*, 493, 381
- Kraus, A. L., Ireland, M. J., Huber, D., Mann, A. W., & Dupuy, T. J. 2016, *AJ*, 152, 8
- Kraus, S., Kluska, J., Kreplin, A., et al. 2017, *ApJL*, 835, L5

- Krumholz, M. R., Klein, R. I., & McKee, C. F. 2005, in IAU Symposium, Vol. 227, Massive Star Birth: A Crossroads of Astrophysics, ed. R. Cesaroni, M. Felli, E. Churchwell, & M. Walmsley, 231–236
- Lin, D. N. C., & Papaloizou, J. 1979, MNRAS, 188, 191
- Lurie, J. C., Vyhmeister, K., Hawley, S. L., et al. 2017, AJ, 154, 250
- Machida, M. N., Tomisaka, K., Matsumoto, T., & Inutsuka, S.-i. 2008, ApJ, 677, 327
- Mathieu, R. D. 1994, ARA&A, 32, 465
- Mathieu, R. D., Stassun, K., Basri, G., et al. 1997, AJ, 113, 1841
- Matsumoto, T., Dobashi, K., & Shimoikura, T. 2015, ApJ, 801, 77
- Mekkaden, M. V. 2000, in IAU Symposium, Vol. 200, IAU Symposium, 31P
- Meyer, D. M.-A., Kuiper, R., Kley, W., Johnston, K. G., & Vorobyov, E. 2018, MNRAS, 473, 3615
- Miranda, R., & Lai, D. 2015, MNRAS, 452, 2396
- Miranda, R., Muñoz, D. J., & Lai, D. 2017, MNRAS, 466, 1170
- Moe, M., & Di Stefano, R. 2017, ApJS, 230, 15
- Motte, F., Bontemps, S., & Louvet, F. 2017, ArXiv e-prints
- Muñoz, D. J., & Lai, D. 2016, ApJ, 827, 43
- Mugrauer, M., Ginski, C., & Seeliger, M. 2014, MNRAS, 439, 1063
- Murillo, N. M., Lai, S.-P., Bruderer, S., Harsono, D., & van Dishoeck, E. F. 2013, A&A, 560, A103

- Muzerolle, J., Hartmann, L., & Calvet, N. 1998, *AJ*, 116, 2965
- Nelson, R. P., Gressel, O., & Umurhan, O. M. 2013, *MNRAS*, 435, 2610
- Orosz, J. A., Welsh, W. F., Carter, J. A., et al. 2012, *Science*, 337, 1511
- Prato, L. 2007, *ApJ*, 657, 338
- Prato, L., Simon, M., Mazeh, T., et al. 2002, *ApJ*, 569, 863
- Raghavan, D., McAlister, H. A., Henry, T. J., et al. 2010, *ApJS*, 190, 1
- Reipurth, B. 2000, *AJ*, 120, 3177
- Reipurth, B., & Clarke, C. 2001, *AJ*, 122, 432
- Reipurth, B., & Zinnecker, H. 1993, *A&A*, 278, 81
- Rey-Raposo, R., Dobbs, C., Agertz, O., & Alig, C. 2017, *MNRAS*, 464, 3536
- Romanova, M. M., Kulkarni, A. K., & Lovelace, R. V. E. 2008, *ApJL*, 673, L171
- Russeil, D., Zavagno, A., Motte, F., et al. 2010, *A&A*, 515, A55
- Shu, F., Najita, J., Ostriker, E., et al. 1994, *ApJ*, 429, 781
- Shu, F. H. 2016, *Annual Review of Astronomy and Astrophysics*, 54, 667
- Sousa, A. P., Alencar, S. H. P., Bouvier, J., et al. 2016, *A&A*, 586, A47
- Stauffer, J., Cody, A. M., Baglin, A., et al. 2014, *AJ*, 147, 83
- Stempels, H. C., & Gahm, G. F. 2004, *A&A*, 421, 1159
- Vartanyan, D., Garmilla, J. A., & Rafikov, R. R. 2016, *ApJ*, 816, 94

Ward-Duong, K., Patience, J., De Rosa, R. J., et al. 2015, MNRAS, 449, 2618

Williams, J. P., & Best, W. M. J. 2014, ApJ, 788, 59

Williams, J. P., & Cieza, L. A. 2011, ARA&A, 49, 67

Yang, Y., Hashimoto, J., Hayashi, S. S., et al. 2017, AJ, 153, 7

Young, M. D., Baird, J. T., & Clarke, C. J. 2015, MNRAS, 447, 2907

Young, M. D., & Clarke, C. J. 2015, MNRAS, 452, 3085

Chapter 2

Accretion and Magnetic Reconnection in the Classical T Tauri Binary DQ Tau

Don't fall in love with your stars.

Ivan King

*A version of this chapter has previously appeared
in the Astrophysical Journal*

Tofflemire, et al. 2017, ApJ, 835, 8

Abstract

Binary star-formation theory predicts that close binaries ($a < 100$ AU) will experience periodic pulsed accretion events as streams of material form at the inner edge of a circumbinary disk, cross a dynamically cleared gap, and feed circumstellar disks or accrete directly onto the stars. The archetype for the pulsed-accretion theory is the eccentric, short-period, classical T Tauri binary DQ Tau. Low-cadence (\sim daily) broadband photometry has shown brightening events near most periastron passages, just as numerical simulations would predict for an eccentric binary. Magnetic reconnection events (flares) during the collision of stellar magnetospheres near periastron could, however, produce the same periodic, broadband behavior when observed at a one-day cadence. To reveal the dominant physical mechanism seen in DQ Tau's low-cadence observations, we have obtained continuous, moderate-cadence, multi-band photometry over 10 orbital periods, supplemented with 27 nights of minute-cadence photometry centered on 4 separate periastron passages. While both accretion and stellar flares are present, the dominant timescale and morphology of brightening events are characteristic of accretion. On average, the mass accretion rate increases by a factor of 5 near periastron, in good agreement with recent models. Large variability is observed in the morphology and amplitude of accretion events from orbit-to-orbit. We argue this is due to the absence of stable circumstellar disks around each star, compounded by inhomogeneities at the inner edge of the circumbinary disk and within the accretion streams themselves. Quasi-periodic apastron accretion events are also observed, which are not predicted by binary accretion theory.

2.1 Introduction

One of the primary outcomes of binary star formation theory is that the interaction between close binary star systems and their disk(s) is fundamentally different than the well-established single-star paradigm. In single stars, interplay between the star and disk is mediated by the stellar magnetic field (Shu et al. 1994; Hartmann et al. 1994). In this magnetic accretion model, strong stellar magnetic fields truncate the inner edge of the disk at the distance where viscous ram pressure balances the magnetic pressure. This “magnetospheric radius” is modeled as 5–10 stellar radii ($\sim 0.05\text{AU}$; Johnstone et al. 2014) for typical pre-MS magnetic field strengths ($\sim 1\text{--}2\text{ kG}$; Johns-Krull 2007) and accretion rates ($10^{-12}\text{--}10^{-8}M_{\odot}\text{ yr}^{-1}$; Alcalá et al. 2014). Inside this radius, material is confined to flow along magnetic field lines where it impacts the stellar surface at magnetic footpoints, shock-heating the photosphere (Orlando et al. 2013).

The single-star magnetic accretion model plays a critical role in the evolution of the star-disk system. For the star, it provides an avenue for continued mass growth while regulating the stellar angular momentum through magnetic disk locking (Shu et al. 1994). For the disk, accretion processes set the evolution timescale by controlling the consumption rate, outflow rates through wind and jet launching, and the intensity of UV radiation relevant for photoevaporation and disk chemistry (Alexander et al. 2014). By governing the stability, lifetime, and chemistry of protoplanetary disks, the star-disk interaction plays a vital role in the formation and evolution of planets.

The successes of the single-star accretion paradigm and its impact on the evolution of the star-disk system highlights the need to characterize the binary-disk interaction. Most pressing is the indication that binary and higher multiple systems are a common outcome

of star-formation (Raghavan et al. 2010). Kraus et al. (2011), for instance, find that up to 75% of Class II/III members of the Taurus-Auriga star-forming region are in multi-star systems. In binary systems with separations on the order of typical protostellar disk radii (~ 100 s of AU; Jensen et al. 1996; Harris et al. 2012) the single-star model cannot simply be applied to environments where the distribution of disk material and mass flows are more complex. While theory describing binary-disk interaction is advancing, many of its predictions remain untested and therefore the effects of binarity on star and planet formation remains largely unconstrained.

Theory describing the binary-disk interaction in short-period systems has made two predictions that portray a complex and variable environment compared to single-stars. First, through co-rotational and Lindblad resonances, orbital motion will dynamically clear a central region around the binary creating up to three stable accretion disks: a circumstellar disk around each star and an encompassing circumbinary disk (Artymowicz & Lubow 1994). Observational support for this spatial structure has come from modeling the IR spectral energy distribution (SED) of spectroscopic binaries (Jensen & Mathieu 1997; Boden et al. 2009) and from spatially resolving central gaps from scattered light (Beck et al. 2012) and mm/sub-mm images (Andrews et al. 2011; Harris et al. 2012) of longer-period systems.

Second, hydrodynamical models predict that circumbinary disk material will periodically form an accretion stream that crosses the cleared gap to feed circumstellar disks or accrete directly onto the stars themselves (Artymowicz & Lubow 1996). Observations of ongoing accretion in pre-MS binary stars necessitates this refueling behavior to balance the short timescale on which a dynamically truncated circumstellar disk would be exhausted through viscous accretion.

Driven by binary orbital motion, predictions for the frequency of circumbinary

accretion streams and their impact on stellar accretion rates are highly dependent on the binary orbital parameters (Günther & Kley 2002; de Val-Borro et al. 2011; Gómez de Castro et al. 2013). Orbital eccentricity in particular has a large effect where, for a given mass ratio, the amplitude and “sharpness” of accretion events (in orbital phase) are predicted to increase with increasing eccentricity. Muñoz & Lai (2016, hereafter ML2016) for instance predict that equal-mass, circular binaries will experience long-duration (multiple orbital periods) accretion enhancements that occur every ~ 5 orbital periods with a factor of 2 increase in the accretion rate at peak. A highly eccentric equal-mass binary, on the other hand, is predicted to exhibit sharp accretion events every orbit that evolve over roughly one-third of the orbital period and increase the accretion rate by more than a factor of 10 at peak. With these orbital parameter dependencies, short-period, eccentric systems provide the best opportunity to test accretion models.

Focusing on this advantageous corner of the eccentricity-period parameter space (analogous to DQ Tau; Table 2.1), the general consensus of models is that each apastron passage (orbital phase $\phi=0.5$) will induce a stream of material from the circumbinary disk (CBD) that feeds a burst of accretion during periastron passage ($\phi=0,1$). The specific morphology and amplitude of the accretion events varies from one modeling effort to the next (i.e. saw-toothed vs. symmetric rise and decay). Also, binary accretion simulations to date have yet to include a magnetohydrodynamic (MHD) treatment, which undoubtedly plays an important role close to the stars (e.g. Kulkarni & Romanova 2008). If these models are representative of binary accretion, they would imply very different angular momentum histories compared to single stars and a more dynamic disk environment relevant for planet formation.

2.1.1 DQ Tau

Since its discovery as a pre-main sequence (pre-MS) spectroscopic binary, DQ Tau has become one of the primary targets in confronting theory of the binary-disk interaction (Mathieu et al. 1997; Basri et al. 1997). Meeting the criteria of a classical T Tauri star (CTTS) with evidence of ongoing accretion and a gaseous protoplanetary disk, DQ Tau is one of a few, well-characterized pre-MS binary systems capable of informing the physics of star and planet formation in the binary environment.

The most extensive characterization of DQ Tau comes from Czekala et al. (2016). Their study combines the orbital solution from high-resolution, optical spectroscopy with disk kinematics derived from ALMA observations to jointly constrain the orbital parameters, stellar characteristics, and critically, the orbital inclination of the system. We compile their results and other relevant system parameters from other works in Table 2.1.

DQ Tau was the first source to provide observational evidence for the pulsed accretion theory. At many, but not all, periastron passages the system exhibited sharp increases in both broadband and $H\alpha$ luminosities (Mathieu et al. 1997; Basri et al. 1997), the same orbital phase predicted by simulations with DQ Tau’s orbital parameters (Artymowicz & Lubow 1996). Broad and variable $H\alpha$ emission line profiles provided support that accretion was, at least in part, the source of the photometric variability. Subsequent studies in the NIR also supported the pulsed accretion interpretation with detections of diffuse, warm gas within a cleared central cavity (Carr et al. 2001; Boden et al. 2009). These results were limited however in their temporal and/or wavelength coverage. Sparse spectroscopic and interferometric observations provide valuable snap-shots of the system but are unable to test the temporal predictions of binary accretion theory. Even the Mathieu et al. (1997) V -band photometry (~ 10 observations per orbit) was only marginally sensitive to accretion,

Table 2.1. DQ Tau System Summary

Parameter	Value	Reference
P (days)	15.80158 ± 0.00066	1
e	0.568 ± 0.013	1
T_{peri} (HJD-2,400,000)	47433.507 ± 0.094	1
a (R_{\odot})	28.96 ± 0.48	1
$q \equiv M2/M1$	0.936 ± 0.051	1
Periastron Separation (R_{\odot})	12.51 ± 0.43	1
Apastron Separation (R_{\odot})	45.42 ± 0.43	1
i ($^{\circ}$)	158 ± 2	1
Rotation Period (d)	~ 2	2
Disk M_{gas} ($10^{-4}M_{\odot}$)	< 10	3
Disk M_{dust} ($10^{-4}M_{\odot}$)	0.90	3
d (pc)	140	4
A_V	1.5 ± 0.3	5
Primary		
M_1 (M_{\odot})	0.63 ± 0.13	1
T_1 (K)	3700 ± 200	1
L_1 (L_{\odot})	0.19 ± 0.07	1
R_1 (R_{\odot})	1.05 ± 0.22	1
Secondary		
M_2 (M_{\odot})	0.59 ± 0.13	1
T_2 (K)	3500 ± 175	1
L_2 (L_{\odot})	0.13 ± 0.07	1
R_2 (R_{\odot})	1.00 ± 0.21	1

Note. — ⁽¹⁾(Czekala et al. 2016), ⁽²⁾(Basri et al. 1997), ⁽³⁾(Williams & Best 2014), ⁽⁴⁾(Kenyon et al. 1994), ⁽⁵⁾(This work)

compared to U -band for instance (e.g. Venuti et al. 2014), and lacked the time-resolution necessary to test accretion models in detail.

While the above studies provide encouraging results for pulsed accretion theory, the quasi-periodic broadband, photometric behavior observed in DQ Tau is not exclusive to periodic enhanced accretion events alone. Magnetic reconnection events on low mass stars can create optical flares with the same general broadband characteristics of accretion. During magnetic reconnection, magnetic energy is converted into kinetic energy accelerating electrons along field lines. In stellar flares, these flows impact the chromosphere and photosphere where relativistic electrons deposit their energy creating a photospheric hot-spot and white-light excess very similar to that of accretion (e.g. compare Kowalski et al. 2013 and Herczeg & Hillenbrand 2008). Stellar flares are stochastic events but in a highly eccentric binary like DQ Tau, orbital motion brings the stars from ~ 43 stellar radii (R_\star) at apastron to $\sim 12R_\star$ at closest approach where the collision between each star's magnetosphere may induce a series of magnetic reconnection events. Salter et al. (2010) find evidence for such events with observations of recurrent synchrotron, mm-wave flares (typical of stellar/solar flares) near the periastron passages of DQ Tau. If these events are capable of depositing their energy in the stellar surface, a large magnetic reconnection event or series of them could create optical flares near periastron that masquerade as the signal of periodic enhanced accretion in low-cadence broadband photometry. High-cadence, multi-color photometry, however, can distinguish between stellar flares and accretion variability.

In an effort determine the primary physical mechanism behind DQ Tau's photometric variability, we have carried out an extensive monitoring campaign combining moderate and high-cadence optical photometry spanning more than 10 orbital periods. Our observations are capable of detecting and characterizing periodic pulsed accretion while determining the contribution from magnetic reconnection events. By monitoring the accretion rate as a

function of orbital phase, these data provide a direct test of binary accretion theory and will extend our understanding of the star-disk interaction to binary systems.

A description of our observations is provided in Section 2.2 as well as our data reduction and calibration procedures. In Section 2.3 we discuss the morphology of our light curves and determine the dominant physical mechanism behind DQ Tau’s variability. We also characterize magnetic reconnection events and their frequency, and place our results in context of the colliding magnetosphere scenario. In Section 2.4 we calculate mass accretion rates, establish the presence of periodic enhanced accretion events, and comment on their variability. Section 2.5 provides a summary of our results.

2.2 Observations & Data Reduction

Observations capable of detecting and characterizing pulsed accretion events in pre-MS binaries require multi-color photometric coverage over many orbital cycles at a cadence that is a fraction of the orbital period. These formidable demands are well met by the capabilities of the Las Cumbres Observatories (LCO) global telescope network (Brown et al. 2013). Described below (Section 2.2.1), these data form the basis of our observational study of DQ Tau.

Despite the comprehensive nature of our LCO observations, they are not capable of characterizing short-timescale events such as flares. To gain sensitivity in this time domain, we supplement our moderate-cadence LCO observations with 33 nights of concurrent minute-cadence, multi-color photometry centered on 4 separate periastron passages. These single-site, traditional observing runs were carried out at the WIYN 0.9m¹ (Section 2.2.2) and ARCSAT 0.5m (Section 2.2.3) telescopes. At the end of this section, we describe our

¹The WIYN Observatory is a joint facility of the University of Wisconsin-Madison, Indiana University, the National Optical Astronomy Observatory and the University of Missouri.

photometry (Section 2.2.4) and calibration (Section 2.2.5) schemes.

2.2.1 LCO 1m Network

The LCO 1m network consists of 9 1m telescopes spread across 4 international sites: McDonald Observatory (USA), CTIO (Chile), SAAO (South Africa), and Siding Springs Observatory (Australia). Together, they provide near-continuous coverage of the southern sky with automated queue-scheduled observing. At the time of our observations, a majority of the 1m network was outfitted with identical SBIG imagers which were chosen to maximize observing efficiency. These $4k \times 4k$ CCD imagers have $15.8'$ fields-of-view with $0.464''$ pixels in standard 2×2 binning.

Over the 2014-2015 winter observing season, our program requested queued “visits” of DQ Tau 20 times per orbital cycle for 10 continuous orbital periods. Given the orbital period of DQ Tau, the visit cadence corresponded to ~ 20 hours. Each visit consisted of 3 observations in each of the broadband *UBVRIY* and narrow-band $H\alpha$ and $H\beta$ filters requiring ~ 20 min. The execution of our program went exceedingly well with 218 completed visits made over 163 days (~ 10.3 orbital periods) with a mean time between visits of 18.0 hours.

Observations are automatically reduced by the LCO pipeline, which performs bad-pixel masking, bias and dark subtraction, and flat-field correction. The three images per filter are then aligned, median combined, and fit with astrometric solutions using standard IRAF² tasks.

While observations were made in all of the filters listed above, in this work we present

²IRAF is distributed by the National Optical Astronomy Observatory, which is operated by the Association of Universities for Research in Astronomy (AURA) under a cooperative agreement with the National Science Foundation.

only those in *UBVR*, which overlap with our high-cadence observations described below. The full observational data set for DQ Tau and other pre-MS binaries in our LCO observing campaign will be presented in an upcoming paper.

Figure 2.1 presents our LCO, *UBVR* light curves in \times symbols plotted against an arbitrary orbital cycle number beginning at the start of our observations.

2.2.2 WIYN 0.9m

Two eight-night observing runs centered on separate periastron passages of DQ Tau (orbital cycles 3 and 5 in Figure 2.1) were obtained from the WIYN 0.9m telescope located at the Kitt Peak National Observatory. Observations were made cycling through the *UBVR* filters to achieve the highest cadence possible while maintaining a signal-to-noise ratio of ~ 100 per stellar point-spread-function.

Our first run obtained some amount of data on all 8 nights. The first 6 of these nights used the S2KB imager while the standard Half-Degree Imager³ (HDI) was being serviced. S2KB is a 2048^2 CCD with a $20.48'$ field-of-view (FOV) and $0.6''$ pixels. Binning (2×2) and chip windowing ($\sim 10'$) were implemented to reduce the readout time and increase our observing cadence. With these measures the average filter cycle cadence was reduced to ~ 5.5 minutes.

HDI was used for the remaining two nights of our first run. HDI is a $4k \times 4k$ CCD with a $29.2'$ FOV and $0.43''$ pixels. Using the four-amplifier mode we were able to reach an improved observing cadence of ~ 3.6 minutes per filter cycle. Our second run utilized HDI exclusively and obtained observations on 6 of the 8 nights. Data from both observing runs were bias subtracted, flat-field corrected, and fit with astrometric solutions using standard IRAF tasks.

³http://www.noao.edu/0.9m/observe/hdi/hdi_manual.html

In addition to our two eight-night observing runs, a synoptic observation program was also in place at the WIYN 0.9m that provided \sim weekly observations of DQ Tau in *UBVR* during the 2014-B semester.

2.2.3 ARCSAT 0.5m

Using Apache Point Observatory’s ARCSAT 0.5m telescope, we performed a 7 and 10 night observing run centered on two separate periastron passages of DQ Tau (orbital cycles 2 and 7 in Figure 2.1). The 1024×1024 FlareCam⁴ imager was used for both observing runs (11.2’ FOV; 0.66’’ pixels). Cycling through the SDSS *u’g’r’i’* filters (Johnson filters were not available) provided an average cadence of \sim 3.8 minutes per filter cycle.

Our first observing run obtained observations on 5 of the 7 nights and 8 of the 10 nights on the second. Data from these runs were bias and dark subtracted, flat field corrected, and fit with an astrometric solution using standard IRAF tasks.

2.2.4 Photometry

Given the large number of images obtained for this project, we rely on the SExtractor (Bertin & Arnouts 1996) software to perform automated source detection and aperture photometry. For each individual data set (LCO, ARCSAT, WIYN 0.9m HDI, WIYN 0.9m S2KB) a matched catalog of each star’s instrumental magnitude is created image-by-image. This catalog is used to perform ensemble photometry following the Honeycutt (1992) formalism in a custom Python implementation.

In short, a system of linear equations is solved to minimize the variation of all stars within our catalog, weighted by their signal-to-noise. Variable, or non-constant stars (including the target) are then interactively removed from the system of equations based

⁴http://www.apo.nmsu.edu/Telescopes/ARCSAT/Instruments/arcsat_instruments.html

on their standard deviation compared to stars of similar magnitude. Iteratively, stars are removed from the solution until only steady, non-varying comparison stars remain, producing differential-light curve magnitudes for all stars. We require a minimum of 3, non-variable comparison stars for each image, and each comparison star must be present in at least 30 separate images across the data set. This technique is ideal for our highly inhomogeneous observations in which observing conditions or pointing errors may change the number and/or collection of comparison stars available in a given image.

2.2.5 Photometric Calibration

Once differential magnitudes are derived for each individual dataset, we perform the photometric calibration required to make direct comparisons across datasets and to calculate mass accretion rates from a measure of the accretion luminosity. While we did not observe traditional standard stars during our observing program, the large FOV of HDI includes three stars for which Pickles & Depagne (2010) have produced “fitted” apparent magnitudes. By fitting the published Tycho2 $B_T V_T$, NOMAD R_N , and 2MASS JHK data with a library of observed, flux-calibrated spectra, these authors have produced best-fit apparent broadband photometry for 2.4 million stars. The 1σ errors on each star’s best-fit magnitudes are ~ 0.2 , 0.06, 0.04, and 0.04 mag for $UBVR$, respectively. The three stars used in our calibration have the following Tycho2 IDs: TYC 1271-1341-1, TYC 1284-216-1, TYC 1271-1195-1. Their best-fit-magnitudes range from 9.76 to 11.65 in V -band magnitude and 0.76 to 1.67 in $B - V$ color.

Using these three stars as our standard calibrators we calculate magnitude zero-points and color coefficients during a photometric night of our HDI run. RMS values from color-magnitude relations were on par or less than the errors quoted in Pickles & Depagne (2010). They are 0.24, 0.10, 0.05 and 0.07 mag for $UBVR$, respectively. As these stars are only

observed in the HDI FOV, we use them to measure apparent magnitudes for all non-variable comparison stars near DQ Tau which are then used to standardize the smaller FOVs of the LCO and S2KB datasets.

In the case of ARCSAT, only the SDSS $u'g'r'i'$ filters were available for our observations. To convert these data to the Johnson filter system, the Jester et al. (2005) Johnson-to-SDSS transformations were used to place our newly calibrated comparison stars into the Sloan system. These were then used to calibrated the differential Sloan magnitudes from ensemble photometry before finally transforming them into the Johnson system.

Near-simultaneous LCO and high-cadence observations provide the opportunity to directly test the agreement of our calibration between datasets. Comparing observations made within 20 minutes of each other (typically 6), the LCO-HDI and LCO-S2KB mean offsets agree to less than the uncertainties quoted in Pickles & Depagne (2010) for each filter. The LCO-ARCSAT offsets are larger, owing to the additional transformation, but are still modest; 0.10, 0.20, 0.10, 0.02 mag for the $UBVR$ transformed magnitudes, respectively. A final offset was applied to match zero-point variations to the HDI dataset from which the apparent magnitudes are initially derived. Offsets were first calculated for overlapping HDI-LCO data and then extended to the WIYN 0.9m and ARCSAT datasets (overlapping with LCO).

The systematic errors involved in our calibration procedure are much larger than the random error on any given point and the random errors are small compared to the intrinsic variability observed. To remain cognizant of the systematic errors however, we propagate them through each step of our analysis and present them as the black error bar in the top right corner of Figures 2.1, 2.6, 2.8, and 2.10.

A machine-readable table providing the epoch of observation (Heliocentric Julian date), zero-point corrected apparent magnitude, random magnitude error, and observing

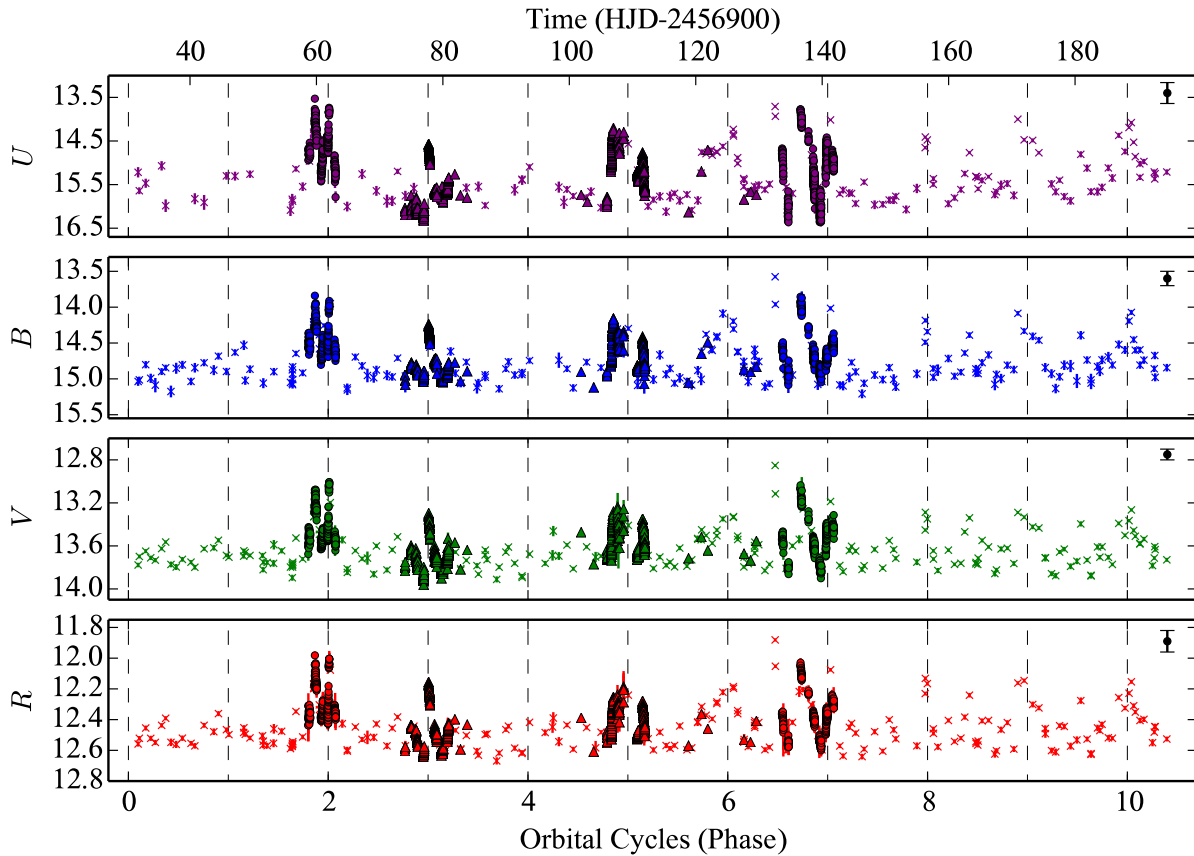


Figure 2.1 DQ Tau $UBVR$ light curves plotted against (arbitrary) orbital cycle number. LCO, ARCSAT, and WIYN 0.9m data are represented as \times , circle, and triangle symbols, respectively. ARCSAT data are transformed from SDSS to Johnson filters. Vertical dashed lines mark periastron passages. Note difference in the y-axis scale for different filters. Large error bar in the top right of each panel represents the systematic error in our photometric calibration. (A machine-readable table of the data presented in this figure is available in the online journal.)

facility for each of the $UBVR$ filters can be found in the online journal associated with Figure 2.1.

2.3 Determining Optical Emission Mechanisms

The optical emission from accretion and from stellar flares is dominated by a combination of Balmer continuum emission and blackbody radiation. During accretion, the flow of disk material along magnetic flux tubes approaches free-fall velocity (supersonic)

toward the stellar surface creating a standing shock above the photosphere. Optically thin material in the post-shock region is responsible for a majority of the blue-optical emission in the form of Balmer continuum. Beneath the post-shock region, the photosphere is radiatively heated creating excess blackbody emission from a hot-spot (Calvet & Gullbring 1998). Hot-spot temperatures have been modeled ranging from 6500 to 10500 K for late M spectral type stars (~ 3000 K photospheric temperatures) with most temperatures in the 8000 to 9000 K range (Herczeg & Hillenbrand 2008).

During a stellar flare, mass-loaded magnetic field lines in the chromosphere or corona develop unstable configurations, leading to magnetic reconnection events that accelerate charged particles towards the footpoints of the new magnetic configuration. In the thick-target electron beam model used to describe solar and stellar flares (Brown 1971), these relativistic particles interact with the chromosphere and photosphere where they deposit their energy creating a white-light excesses (Allred et al. 2006). While the mechanism by which mechanical energy is converted into radiative energy remains an open question, most solar/stellar flares follow this general model (Fletcher et al. 2011, and references therein). Observationally, the blackbody component of stellar flares dominates over Balmer continuum at the flare peak where hot-spot temperatures range between 10000 and 14000 K, reducing to 7000 to 10000 K in the decay phase (Kowalski et al. 2013). The higher blackbody temperatures compared to accretion result from energy deposition directly into the photosphere by the electron beam rather than from radiative heating (Kowalski et al. 2015).

While both accretion and flares emit optical light by depositing energy and mass into the stellar surface, the timescale, morphology, and detailed SED of each processes variation can be distinguished with high-cadence, multi-color optical photometry. Accretion is observed to naturally occur in bursts above a steady accretion rate lasting days at a time

without a consistent light curve morphology (Stauffer et al. 2014). This timescale may be related to the time for instabilities to develop at the disk-magnetosphere interface (Kulkarni & Romanova 2008; Ingleby et al. 2015).

Stellar flare morphologies on the other hand have been extensively characterized in the case of active M dwarfs, through high-cadence, uninterrupted observation with the *Kepler* space telescope. Most flares ($\sim 85\%$) exhibit the “classical” morphology consisting of an impulsive-rise followed by an exponential-decay (Davenport et al. 2014; their Figure 3). The ratio of rise-to-decay times varies from ~ 0.05 to 1, with rise times typically shorter than 10 minutes. Flares also come in non-classical flavors: “complex” or “hybrid”, a superposition of multiple classical flare events, and “gradual” or “slow”, which are less impulsive (Kowalski et al. 2013; Dal & Evren 2010). Regardless of the flare type, the rise-times are generally less than 1 hour. For reference, the longest optical flare observed on any star (M dwarf, pre-MS, or RS CVn) occurred over ~ 10 hours and took ~ 30 minutes to rise (Kowalski et al. 2010, YZ CMi).

We focus on M dwarf flares because the combination of being intrinsically faint (making it possible to detect small flares) and ubiquitous in the galaxy has made them the subject of the most extensive flare studies to date. The observed temporal and morphological characteristics, however, are consistent with the more limited studies of stellar flares on pre-MS stars (Fernández et al. 2004), making them suitable for comparison with DQ Tau. Pre-MS stars appear only to differ in that they have typical flare energies that are a factor of 100 (or more) larger than M dwarfs.

The difference in color between accretion and stellar flares is more subtle than that of the timescale and morphology, especially when only considering the coarse wavelength information presented here (*UBVR*). In general, the peak emission from a stellar flare is bluer than accretion radiation due to the strong, high-temperature blackbody component.

As the flare decays, however, this distinction in color becomes less apparent.

To access the physical mechanism behind the broadband variability seen in DQ Tau, we investigate the morphology, timescale, color, and energy associated with brightening events. First, the qualitative aspects of the light curve morphology and timescale of variation are compared to long-term, space-based campaigns monitoring accreting young stellar objects and active M dwarfs. Before characterizing the properties of accretion in Section 2.4, we define quantitative limits for the detection of flares, characterize the color, timescales, and energy of those that are detected, and place limits on their contribution to the total optical variability. Finally, we place our results in the context of the colliding magnetospheres scenario.

2.3.1 Light Curve Characteristics

Figure 2.1 presents our full DQ Tau, $UBVR$ light curves covering 10.3 orbital periods (~ 163 days). LCO observations are presented as \times symbols with ARCSAT and WIYN 0.9m observations shown with circles and triangles, respectively. The bottom x-axis is an arbitrary orbital cycle number chosen to set the first observed periastron passage to 1. Below, we refer to brightening events using the cycle number as it is presented in this figure. (The top axis displays Heliocentric Julian days.) Each periastron passage is shown with a vertical dashed line. The y-axis scale of each panel is set to match the variability of each filter and differs greatly with photometric band. As expected in either accretion or flare events, the bluest filters display the largest variability; >3 mag in U while <1 mag in R .

Focusing on the U -band light curve in Figure 2.1 (our most sensitive diagnostic of photospheric hot-spots, whether from accretion or flares), brightening events of varying complexity and amplitude are seen around each periastron passage. The duration of these

events varies and can be as long as half the orbital period. A significant amount of variability is also seen outside of periastron, especially near certain apastron passages (e.g. orbital cycles 6.5, 8.5, and 9.5).

Comparing our V -band light curve with that of Mathieu et al. (1997), we find consistent results with brightening events occurring around many, but not all, periastron passages. Simultaneous observations in U -band, however, reveal that “quiescent” V -band periastron passages do indeed have a detectable U -band enhancement, due to the smaller contribution from the stellar photospheres and a larger contribution from accretion luminosity at shorter wavelengths. With the large range in time presented in Figure 2.1, the detailed structure of brightening events are hard to discern but already it is clear that some periastron passages display short, bursty events (orbital cycles 3 and 8), while others display a prolonged elevated state (orbital cycles 5, 6 and 9).

Figure 2.2 provides an expanded view of our high-cadence U -band observations. Each panel presents a different periastron passage listed in the top right, with vertical lines denoting the time of closest approach. Horizontal dotted lines mark the quiescent U -band value from orbital phases $\phi=0.2$ to 0.4 (consistently the quietest phase of the orbit, see Figure 2.7 for reference). These data highlight the complex structure of periastron brightening events showing variability in the morphology, scale, and onset of the event. While variability is seen on a variety of timescales, the underlying large scale evolution takes place over days rather than hours. Each periastron passage observed with high-cadence photometry shows increases above the quiescent level for tens of hours if not days at a time.

Recent space-based campaigns monitoring the variability of accreting young stellar objects and magnetically active M dwarfs provide a wealth of data against which to compare our high-cadence observations. The *CoRoT* space telescope monitored the star-forming

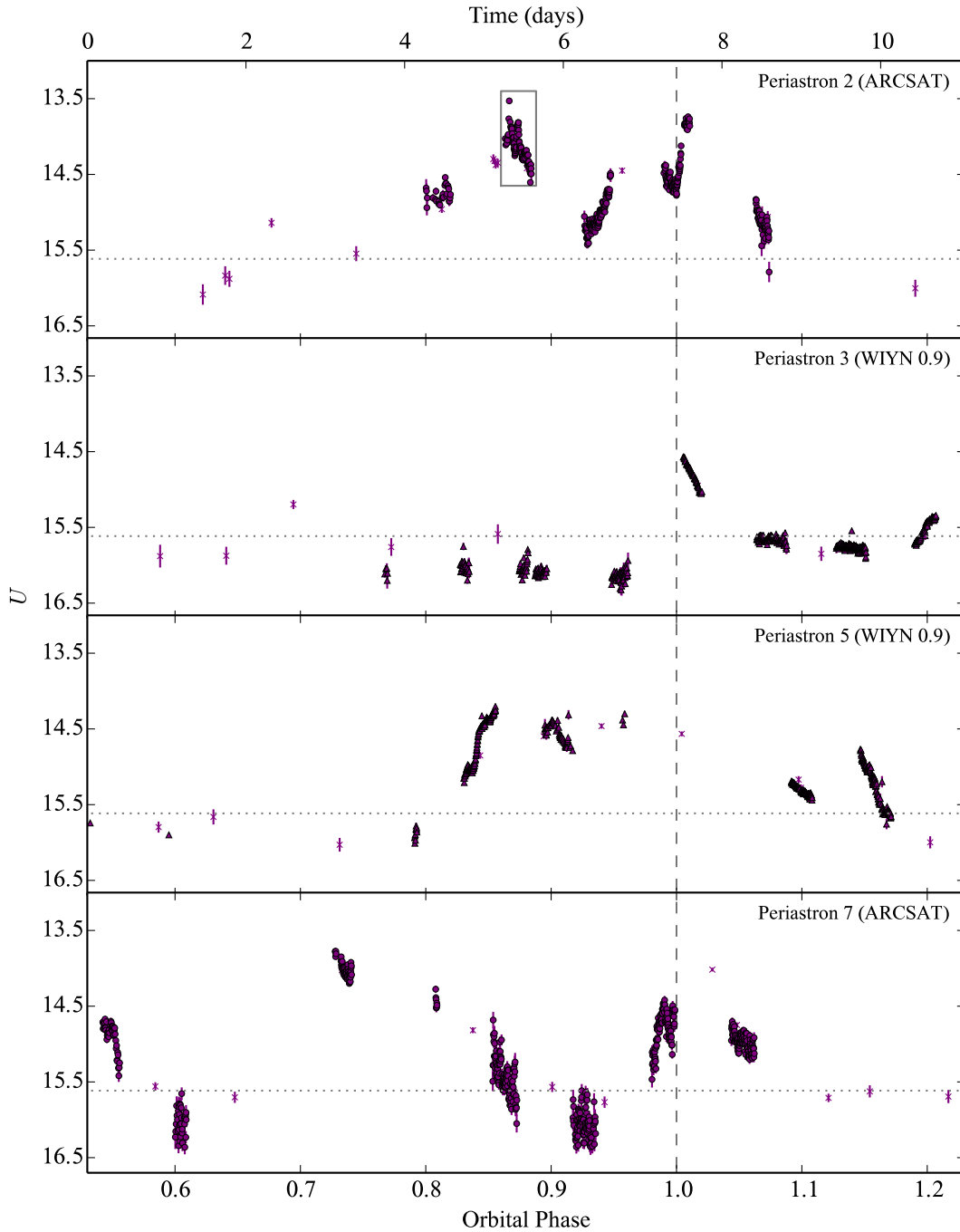


Figure 2.2 DQ Tau high-cadence, U-band light curves highlighting the rise and decline over the course of days near periastron passage. Vertical dashed lines mark periastron passage. Horizontal dotted lines mark the quiescent brightness. Periastron number in relation to Figure 2.1 is provided in the top right of each panel along with the source of the data. LCO observations are \times symbols. The light gray box in the top panel marks the region plotted in Figures 2.4 and 2.5.

region NGC 2264 for ~ 40 days continuously at a 512-second cadence, revealing a myriad of complex variability trends (Cody et al. 2014). Comparing our R -band observations to the *CoRoT* R -band (white-light) light curves, we find many similarities with the class of objects defined as “bursters” (Stauffer et al. 2014; their Figure 1, right panels). These objects make up the dominant light curve class of stars with large UV-excesses and are interpreted as episodic bursts of accretion evolving over days at the few tenths of a magnitude level in *CoRoT* R . The variable morphology of these events as well as their amplitude and timescale, support an accretion dominated interpretation of the observed optical variability.

We also compare our light curves to the Hawley et al. (2014) study of active M dwarfs using *Kepler*, minute-cadence data. Variability in these stars is dominated by sinusoidal star-spot modulations with sharp enhancements from flares. Flares of this type would appear as near-vertical brightening events in Figures 2.1 and 2.2 while the observed enhancements are smoother in nature.

The color of the variability also points to accretion. The observed R -band increases are on the order of ~ 0.5 mag with U -band excesses of ~ 2 mag. This color is redder than what is typical of stellar flares at their peak. Flares with peak R -band enhancements of 0.5 mag are rare and accompanied by U -band components of >4 mag (Hawley & Pettersen 1991; Davenport et al. 2014). Figure 2.3 presents the extinction corrected U - R excess color vs U -band excess above a photospheric model (described in Section 2.4). Most data do not reach the extremely blue U - R colors typical of large flare peaks ($U-R \sim 3.5$).

We explore the presence of flares in more detail in the following section but in general, conclude that large scale changes in the accretion rate are the most plausible source of optical variability based on the morphology, timescale, amplitude, and color of the events.

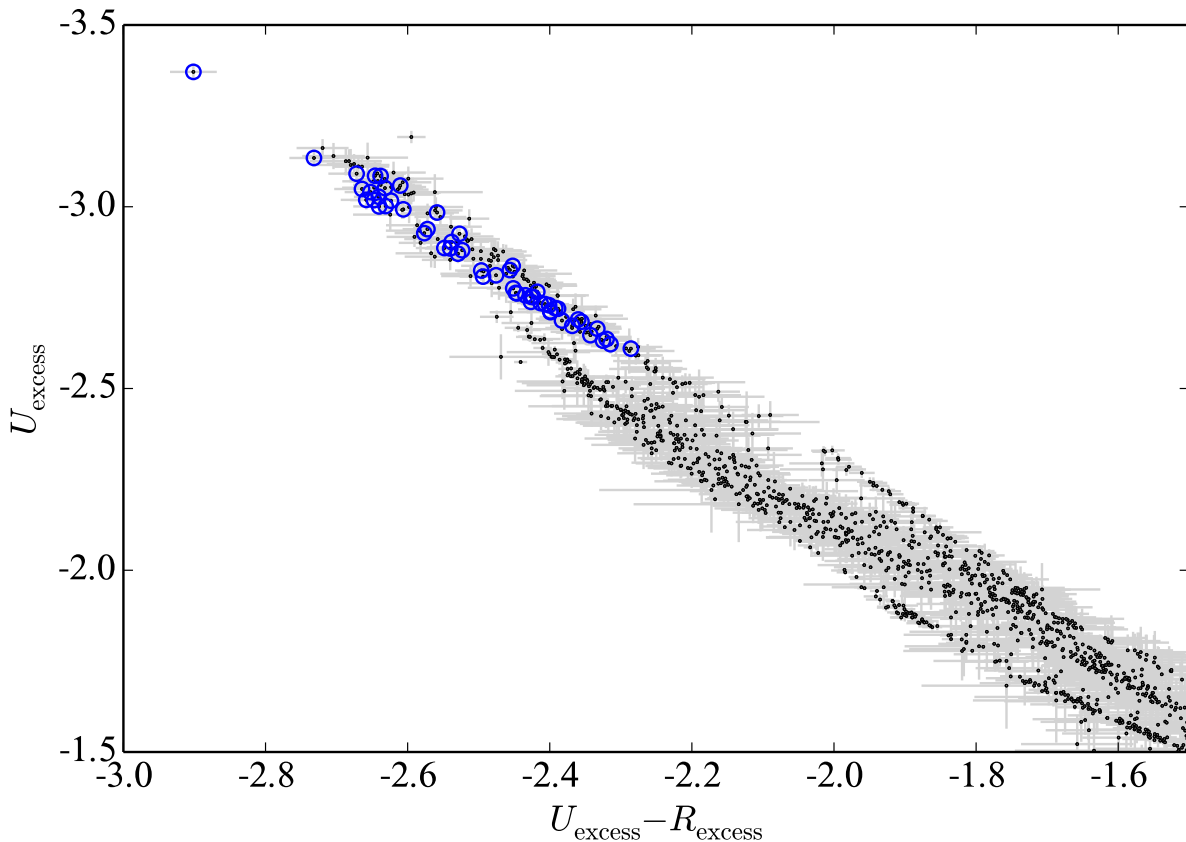


Figure 2.3 Extinction corrected $U-R$ color-magnitude diagram of emission above the stellar photosphere. Encircled points highlight candidate flares from high-cadence light curve analysis. The bluest point observed in $U-R$ is the peak emission of “Flare 1” presented in Figure 2.5 (see text). (Extinction and template determination discussed in Section 2.4.)

2.3.2 Stellar Flares

Although accretion processes appear to dominate the large-scale optical variability on day timescales, we also investigate our nightly, high-cadence light curves to determine the contribution from stellar flares. Based on the empirical M dwarf flare behavior described above, we develop a flare finding scheme aimed at detecting impulsive brightening events on timescales of tens of minutes in our U -band, high-cadence light curves. Our detection scheme is as follows: for each U -band observation the median value of data and its error within the prior 60 minutes is computed (typically 12 to 20 points given our average cadences on each telescope/detector combination). Points falling 10 times above the

median error are then visually inspected as possible flares. This conservative value is taken to compensate for the large underlying variability from accretion. Our flare detection threshold is adaptive in this case and can range from $\Delta U=0.04$ to 1.58 with a median value of 0.32 mags. Using a shorter averaging window of 30 minutes recovers the same results.

Following this procedure, three groups of points fall above our 10σ threshold. The first two are short-timescale events we select as flare candidates and discuss in detail below. The third comes from the steep rise prior to periastron passage 5 (Figure 2.2, third panel, orbital phase ~ 0.83). While a spectacular event in and of itself, rising more than 1 mag in U over the course of >9.5 hours, we do not classify it as a flare given the relatively long timescale over which it is evolving.

Figure 2.3 presents the $U-R$ color-magnitude diagram of emission above the stellar photosphere. Data from the two candidate flares are over-plotted with blue circles. The bluest point observed occurred during the peak of the first candidate flare and is significantly bluer than other measurements that are attributed to accretion. This aligns with our expectation that the peak brightness of a stellar flare will be bluer than the emission from accretion. Most of the rise and decay phase, however, are indistinguishable in color space from the rest of the optical (accretion) variability.

Figure 2.4 presents the night of high-cadence data in which our candidate flares are detected. The fact that these two events fall close together in time (partially overlapping) is not necessarily a concern given that there is evidence for sympathetic flaring (flares triggering subsequent flares) on low-mass stars (Panagi & Andrews 1995; Davenport et al. 2014) and the Sun (Pearce & Harrison 1990). To provide context within the large-scale variability of DQ Tau, these data are highlighted in the top panel of Figure 2.2 with a light gray box. In an attempt to characterize the emission from these events alone, we fit a cubic spline to regions of the light curve devoid of flares in order to remove accretion variability.

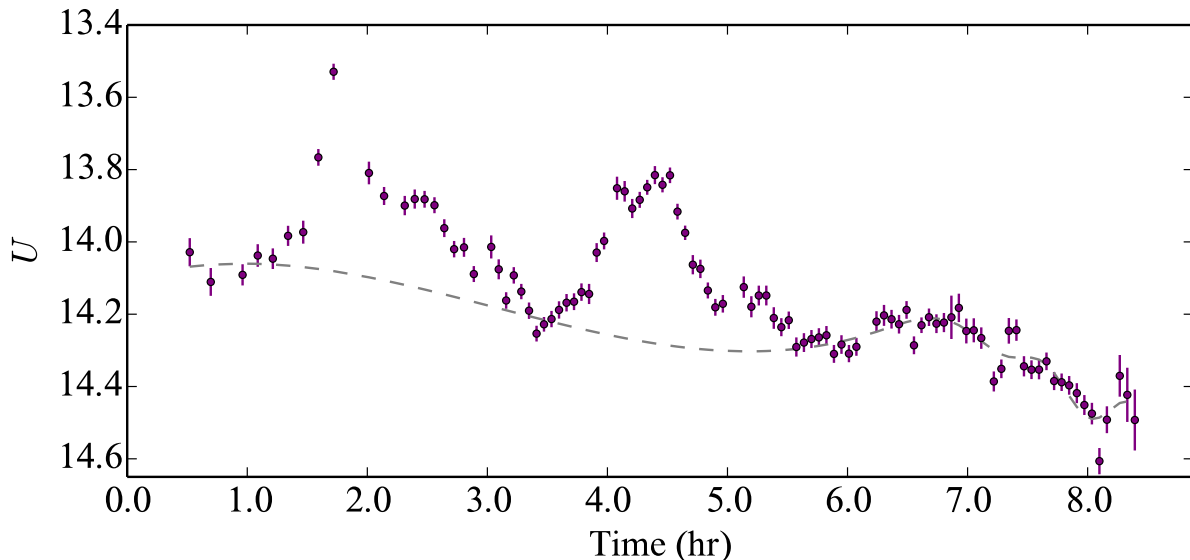


Figure 2.4 ARCSAT U-band light curve during one night of observation in which two flares are present. The gray box in the top panel of Figure 2.2 shows the location of these data with respect to orbital phase and the rest of the observing run. The gray dashed line displays a cubic spline fit to regions of the light curve devoid of flares.

The fit is shown as the gray dashed line in Figure 2.4. Subtracting this crude model and converting to normalized flux results in Figure 2.5.

The first event in Figure 2.5, “Flare 1”, has the morphology of a classical flare. The red line over-plots an empirical classical flare template from Davenport et al. (2014). Constructed from 885 classical white-light flares on the active M dwarf GJ 1243 observed with *Kepler*, this flux normalized model is broken into a rise and decline phase that depends on the event timescale, $t_{1/2}$, the time spent above half the peak flux. A 4th-order power series in $t_{1/2}$ describes the rise phase and a sum of two exponentials describes the decline. We do not fit the template to our data in a χ^2 sense, but over-plot the template using the measured $t_{1/2}$ value and an amplitude normalization. The agreement is not perfect but given the uncertainty in the background subtraction, we find it to be reasonable evidence that this event is a flare from a magnetic reconnection event.

The second event during this night, “Flare 2”, does not have the classical flare

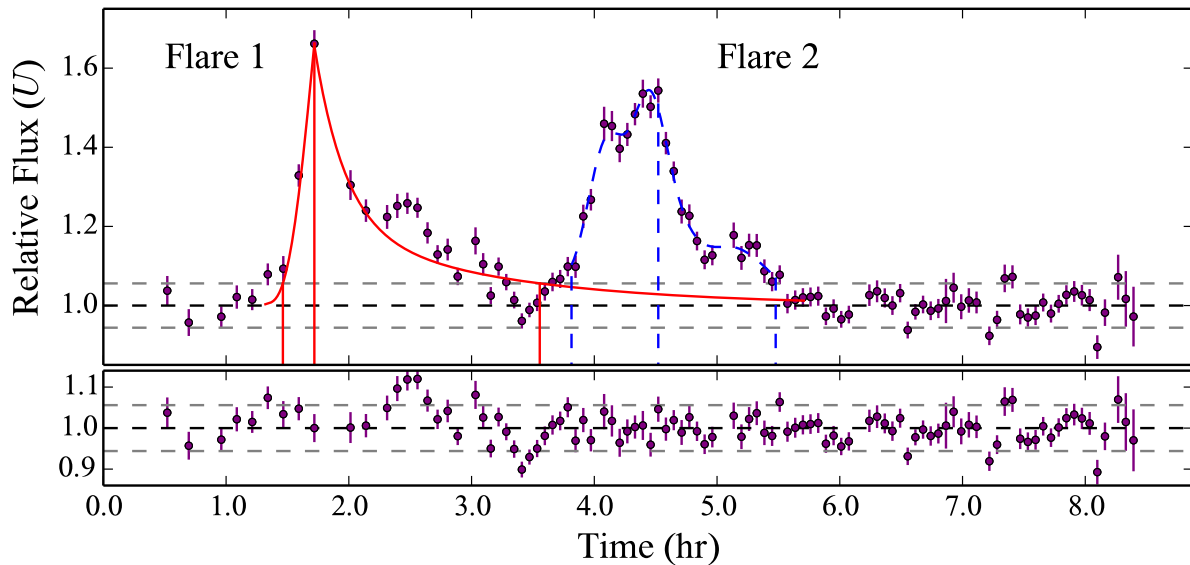


Figure 2.5 Light Curve from Figure 2.4 plotted as relative flux above the background accretion variability model. The red curve displays the classical flare template of Davenport et al. (2014). Vertical red lines mark the beginning, peak, and end of the flare. The blue curve is a cubic spline fit to the classical flare subtracted light curve. Vertical blue dashed lines mark the beginning, peak, and end of the gradual flare. The bottom panel presents the residuals from model subtraction. Horizontal gray dashed lines in both panels mark the standard deviation of data devoid of flares after subtraction of the accretion model.

morphology but may be a slow or gradual flare. Although, our cadence may not be high enough to decompose multiple small classical flares events if it were instead a hybrid or complex flare. Without an empirical model for non-classical flares to compare against, we fit a cubic spline (blue curve in Figure 2.5) to the accretion and classical flare subtracted data.

In addition to the morphology and timescale arguments above, we make a quantitative comparison of the flare energy in the UBV filters to flares observed on other pre-MS stars. We determine the rise and decay times for each flare where our flare templates exceed the non-flaring standard deviation (top dashed line in Figure 2.5; location of start, peak, and end times are marked with vertical lines). The flare energy is then computed with a trapezoidal integration of the excess emission above our accretion model (dashed line is

Figure 2.5) assuming a distance of 140pc and $A_V=1.5$ (see Section 2.4). Table 2.2 presents their temporal characteristics from the U -band light curve and total energy in the UBV filters. Error in the energy comes from applying the maximum and minimum offsets of our photometric systematic error. The derived energies in each filter fall within the spread of flares observed on other pre-MS stars ($2 \times 10^{34} < E_U(\text{ergs}) < 1.1 \times 10^{36}$; Gahm 1990; Fernández et al. 2004; Koen 2015) and the ratio of energy between each filter agrees with the trend seen on pre-MS stars as well as M dwarfs (Lacy et al. 1976; Gahm 1990). This result provides further evidence for a magnetic reconnection origin of these events.

These two flares were the only events in our high-cadence light curves that had the amplitude and timescale typical of magnetic reconnection as we understand them from low-mass dwarfs and pre-MS stars. To quantitatively compare the timescale of our flares to the large-scale variability, we measure the $t_{1/2}$ values of the 10 largest brightening events observed at high-cadence. Using the quiescent brightness level shown in Figure 2.2 as the baseline, we find an average $t_{1/2}$ value of 21.7 hours with the shortest being 2.5 hours. These values are an order of magnitude longer than those calculated for the flares in Table 2.2.

Lastly, to determine the fraction of our data in which flares are present, we first calculate the amount of time in which our data are capable of detecting flares. Hawley et al. (2014) find that a majority of flares are less than 2.5 hours in duration. Setting this as the minimum duration of continuous monitoring (with data gaps less than 30 minutes) required to detect flares, 141 hours of “flare coverage” are obtained. Within this window, only 4.1 hours contain flares at an average level of $\Delta U \sim 0.32$, corresponding to $\sim 3\%$. Here we have assumed a perfect detection efficiency above the detection threshold as each event is visually inspected and characterized, finding it in good agreement with flares on other pre-MS stars. With that in mind, this value should be taken as a lower limit on the

temporal flare contribution given our variable detection threshold. Small flares that would go undetected in our data evolve quickly however, and would not contribute significantly given the ~ 3 magnitude U -band variations observed in the system. We also note that the fraction of time spent flaring derived above is from observation near periastron alone. Our data provide no information on the occurrence of flares near apastron or if any orbital-phase-dependence exists.

We conclude that flares play a very small roll in the amplitude and temporal nature of DQ Tau’s variability, and that the broadband variability is due to a variable accretion rate. For the remainder of our discussion we remove the two flares using the models described above (the residuals of which are shown in the bottom panel of Figure 2.5) and attribute all remaining variability to changes in the accretion rate.

Table 2.2. Flare Characterization Summary

Parameter	Flare 1	Flare 2
$t_{1/2}$ (min)	23.9	41.6
Rise Duration (min)	15.4	42.4
Fall Duration (min)	110.2	57.4
ΔU (mag)	0.55	0.47
U -band Energy (10^{35} ergs)	2.2 ± 0.5	1.6 ± 0.4
B -band Energy (10^{35} ergs)	2.1 ± 0.4	1.0 ± 0.2
V -band Energy (10^{35} ergs)	1.8 ± 0.2	0.5 ± 0.1

Note. — Temporal measurements from U -band light curve.

2.3.3 Colliding Magnetospheres

Here we consider whether the detection of flares near a periastron passage of DQ Tau might be indicative of magnetic reconnection events in colliding magnetospheres. In this scenario, the large-scale magnetic fields of both stars interact during periastron approach (bringing the stars from ~ 43 to $12 R_\star$) leading to unstable magnetic configurations and reconnection in the case of field lines with opposing polarity (see Adams et al. 2011).

Evidence for colliding magnetospheric reconnection in DQ Tau comes from Salter et al. (2010) who find recurrent, mm-wave synchrotron enhancements during three out of four observed periastron passages. With only 8 to 16 hours of observation per periastron passage, the consistency of radio flares points to inter-magnetospheric reconnection being a commonplace event near periastron. The largest of these events reached a peak luminosity of $\sim 10^{28}$ ergs s $^{-1}$ at 2.7 mm (115 GHz; 1 GHz bandpass) and while it was not observed through its return to quiescence, the event was modeled with a ~ 30 hr duration. Radio flares of this amplitude have been observed on the weak-lined T Tauri star (WTTS) binary V773 Tau (Massi et al. 2002, 2006), which were also attributed to colliding magnetospheres. Both, however, are an order of magnitude more luminous than the largest radio events observed on active M dwarfs (Osten et al. 2005) or RS CVn binaries (Trigilio et al. 1993). If optical events similar to stellar flares accompanied these events at amplitudes that scale with the radio component, our observations would easily detect them given the sensitivity to impulsive brightening events derived above.

While we have assumed that magnetic reconnection between colliding magnetospheres is capable of creating an optical, stellar-flare-like counterpart, determining the detailed characteristics of an optical counterpart to radio events of this scale is difficult. Some of the most extensive simultaneous radio and optical monitoring has been on active M dwarfs.

During flares the optical component is seen to evolve on a much shorter timescale than the radio counterpart (Osten et al. 2005; Butler et al. 2015). The prolonged radio decay is attributed to magnetic mirroring near footpoints where field lines converge, increasing the field strength, and reflecting synchrotron producing electrons (e.g. Aschwanden et al. 1998). This effect may have a large impact on magnetic reconnection events far from the stellar surface. The efficiency of magnetic mirroring depends on the ratio of the field strengths that a particle experiences which, for DQ Tau, assuming a simple dipole, would correspond to ~ 245 from $6.3R_\star$ (midpoint between stars at periastron) to the stellar surface. In solar flares where the site of reconnection is in the chromosphere or corona, this ratio is typically measured as 2, or less (Tomczak & Ciborski 2007; Aschwanden et al. 1998).

Moving the site of reconnection further from the surface of the stars also raises concerns of synchrotron radiative losses and the potential for collisional losses with intervening circumstellar material that prevents accelerated electrons from reaching the chromosphere. If the energy from magnetic reconnection remains confined or lost to other processes it will prevent the conversion of mechanical energy to an optical counterpart at the stellar surface. Salter et al. (2010) present some simultaneous optical photometry during the decay phase of one of their radio flares which also shows a general decaying behavior (their Figure 7). While the match between the optical and radio morphology is compelling, this behavior is not seen in standard solar/stellar flares.

Aside from light curve morphology, we also compare the energy of optical and radio brightening events to the available magnetic energy budget. Assuming quasi-static, anti-aligned dipole fields, Adams et al. (2011) estimate the magnetic interaction energy available for reconnection events as a function of the stellar radius, the surface magnetic field strength, and apastron-to-periastron separation (their Equations 13 and 14). The interaction energy is derived from the difference between the lowest energy magnetic field

configurations at periastron and apastron. Energy in this model is provided by the orbital motion which compresses the fields and is only a fraction of the total magnetic energy stored in the fields.

Adopting a surface dipole field strength of 1.5 kG and the parameters listed in Table 2.1, DQ Tau has an available interaction energy of $\sim 10^{35}$ ergs (only $\sim 1\%$ of the combined magnetic energy beyond an interaction distance of $6.3R_*$ for each star). Integrating a synchrotron source function matching the observed 90 GHz flux density from 0 to 90 GHz for a range of power-law electron energy distributions (1.1 to 2.9), we find energies ranging from $0.4\text{--}6.7 \times 10^{35}$ ergs, assuming a 6.55 hr e -folding decay timescale (Salter et al. 2008, 2010). For comparison, trapezoidal integration of our photosphere-subtracted, flux-calibrated observations produces an average of $\sim 10^{38}$ ergs emitted in the combined *UBVR* filters during periastron passage ($\phi = 0.7$ to 1.3), a factor of 10^3 more than the available magnetic energy budget.

Based on the multi-day variability of optical brightening events, the excess of optical energy released near periastron when compared to the colliding magnetosphere energy budget, the paucity of classical optical flare events (for lack of a better model), and the favorable conditions for magnetic mirroring, we conclude that reconnection events from colliding magnetospheres do not contribute significantly to the periodic luminosity increases in our optical light curves. The optical flares that are present do have energies that agree with the colliding magnetosphere energy budget but, they are also typical of flares on single pre-MS stars, are less regular than radio events, and occur at a relatively wide stellar separations ($\sim 24R_*$). These flares may very well be the result of magnetic reconnection on the surface of one of the two stars. Simultaneous optical and radio observation will be required, however, to make a definitive statement on their origin.

2.4 Characterizing Accretion

A measurement of the mass accretion rate can be made by determining the excess emission above the stellar photosphere(s) resulting from accretion. This requires an estimate of the underlying spectral type and extinction in the absence of accretion. We determine these properties following the method described in Herczeg & Hillenbrand (2014). These authors compute a library of low-resolution, pre-MS spectral templates from a grid of 24 flux-calibrated WTTS spectra, spanning spectral types K0 to M9.5. Empirical templates have the advantage over synthetic spectra in that they include chromospheric emission (see Ingleby et al. 2011) and provide more accurate colors for these, typically, highly spotted photospheres (e.g. Grankin et al. 2008; Alencar et al. 2010). Templates are fit to the spectra of accreting CTTSs modifying the intrinsic luminosity, extinction, and additive accretion continuum level as free parameters. Cardelli et al. (1989) extinction curves are used assuming $R_V=3.1$ and the accretion continuum is modeled as a constant flux value across wavelength. As noted above, the true accretion spectrum has structure from the Balmer jump and emission lines; however, the fits here only include wavelength regions redward of 4000\AA and exclude emission lines. Within these continuum-dominated windows, a flat spectrum provides an adequate description of accretion while keeping the degrees of freedom minimal. The binary nature of DQ Tau is ignored in this process but as a near equal-mass binary, the combined spectrum of both stars should not differ greatly from that of a single star at low-spectral resolution.

Applying this procedure to a flux-calibrated spectrum of DQ Tau obtained in January 2008 with the Double Spectrograph (Oke & Gunn 1982) on the Hale 200 inch telescope (originally published in Herczeg & Hillenbrand 2014), we find a spectral type of M0.4 and an extinction of $A_V=1.5$. These values agree with the results of Herczeg & Hillenbrand

(2014) who quote typical uncertainties of 0.3 spectral type subclasses and 0.3 magnitudes of extinction for (single) M stars. Both measurements also lie in the middle of the values found in the literature (Strom et al. 1989; Kenyon & Hartmann 1995; Czekala et al. 2016). Even though this work is primarily concerned with the relative changes of the accretion rate, the importance of extinction on the derived accretion rate baseline should be noted. The ± 0.3 magnitude uncertainty of this method corresponds to a 0.2 dex systematic uncertainty in all accretion luminosities (rates) and flare luminosities (energies).

The WTTS templates extend from 3130-8707Å with a central gap from 5689-6193Å. Before convolving the best-fit template with filter curves we fill this gap in the spectral coverage by finding the best-fit BT-Settl atmospheric model (Baraffe et al. 2015). A best fit is found at a temperature of 3900 K and $\log(g)$ of 4.0, in agreement with Czekala et al. (2016).

With a model for the combined photospheric contribution in DQ Tau, we determine the mass accretion rate by first converting the U -band excess luminosity into an accretion luminosity following the empirical relation found by Gullbring et al. (1998):

$$\log(L_{\text{Acc}}/L_{\odot}) = 1.09 \log(L_{U_{\text{excess}}}/L_{\odot}) + 0.98 \quad (2.1)$$

The U -band photospheric luminosity is computed by convolving the template with a U -band filter curve (Maíz Apellániz 2006; Pickles & Depagne 2010), adopting a distance of 140 pc. This luminosity is then subtracted from the observed, extinction-corrected U -band luminosity, providing $L_{U_{\text{excess}}}$.

In these calculations we have ignored the contribution to variability from star-spots. Spot variations on non-accreting pre-MS stars are typically a few tenths of a magnitude in U -band (Bouvier et al. 1995). This is much smaller than the observed variability and at a high inclination angle (~ 22 degrees), the geometry of hot and cool spot visibility due to

rotation should have a small effect.

From accretion luminosities we calculate mass accretion rates using the following formula,

$$\dot{M} \simeq \frac{L_{\text{Acc}} R_{\star}}{GM_{\star}} \left(1 - \frac{R_{\star}}{R_{\text{in}}}\right)^{-1}, \quad (2.2)$$

where R_{in} is the magnetospheric truncation radius from which accreting material free-falls along field lines. The value of R_{in} depends on the strength of the magnetic field and the ram pressure of accreting material. In the binary environment, where mass flows are predicted to be highly variable and phase dependent (ML2016), the conditions of accreting material are likely not well described by a single value of R_{in} . As we discuss below, the ram pressure of accreting material is likely highest near periastron. If this behavior corresponds to smaller R_{in} values, a constant value of R_{in} will underestimate the accretion rate near periastron and overestimate it at times of low accreting ram pressure (presumably apastron). Without a model for the time variable interaction of the magnetic field with circumstellar material, we resort to the canonical single star value of $R_{\text{in}} = 5R_{\star}$ (Gullbring et al. 1998), even though it is less physically motivated in this case. Fortunately, the mass accretion rate is fairly insensitive to R_{in} (a factor of 2 decrease in R_{in} corresponds to a factor of 0.6 in the mass accretion rate). Given these uncertainties, accretion luminosity measurements are also included in Figures 2.6, 2.7, and 2.10.

Following this procedure we calculate mass accretion rates ranging from 5.9×10^{-10} to $2.2 \times 10^{-8} M_{\odot} \text{yr}^{-1}$, in good agreement with measurements from optical and NIR spectra (Gullbring et al. 1998; Bary & Petersen 2014). The top panel of Figure 2.6 displays the mass accretion rate as a function of orbital cycle. An increase in the accretion rate can be seen at every periastron passage; at some, the accretion rate increases by more than a factor of 10 from the quiescent value.

The bottom panel of Figure 2.6 presents the mass accreted over each full orbital period

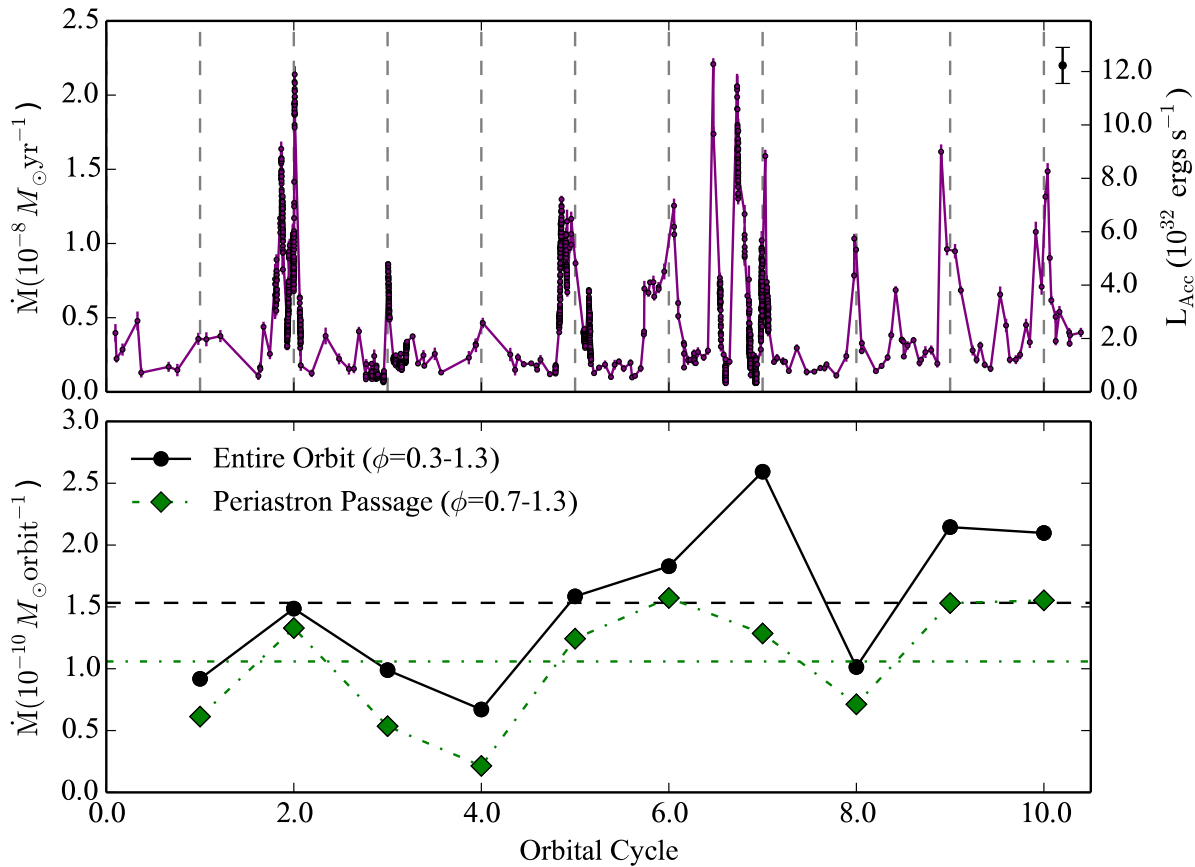


Figure 2.6 Top: Accretion rate (left axis) as a function of orbital cycle. Right axis displays the corresponding accretion luminosity. Dashed vertical lines mark periastron passages. **Bottom:** Integrated mass accreted per orbit. Black circles represent the mass accreted per full orbital period (orbital phases $\phi=0.3$ to 1.3). Green diamonds represent the mass accreted per periastron passage (orbital phases $\phi=0.7$ to 1.3). Horizontal dashed and dot-dashed lines mark the average orbital and periastron accreted masses, respectively.

and over each periastron passage. For the full orbit, we define our integration range to be orbital phases $\phi = 0.3$ to 1.3 in order to include the entire periastron event. For periastron passages, the integration range is over orbital phase $\phi = 0.7$ to 1.3. Black circles and green diamonds mark the full orbit and periastron integrations, respectively, with horizontal lines marking the mean of each. This periastron passage range encloses 60% of the orbital period but has a median contribution of 71% to the total mass accreted per orbital period. Large variability exists, however, with periastron contributions ranging from 49-90% of the total mass accreted per orbital period. We note that some of this variability may result

from changes in the observing cadence. Some periastron passages with sparse observations (orbital cycle 4, for instance) may not accurately sample, or entirely miss, short-duration accretion bursts. The bottom panel of Figure 2.6, however, is not significantly altered when only including the more consistently sampled LCO data.

2.4.1 Periodic Enhanced Accretion

Numerical simulations of the binary-disk interaction predict that in cases of high eccentricity, discrete accretion events should occur near every periastron passage. We test this prediction by performing a Lomb-Scargle periodogram analysis (Scargle 1982) on the mass accretion rates derived from LCO observations. Figure 2.7 displays the mass accretion rate phase-folded about the spectroscopically determined orbital period in the top panel and the periodogram of those data in the middle panel. The red line in the bottom two panels marks the 99% false-alarm-probability (FAP) determined using a Monte Carlo bootstrap simulation (Frescura et al. 2008).

Even with the large variability present near periastron, typical of accretion in CTTSs, a significant peak is found near the spectroscopic period (marked with the dashed vertical line). We find a period of 15.91 ± 0.08 days, in good agreement (1.3σ) with the orbital period. (Periodogram peak errors are calculated by enclosing 68% of a the probability-distribution-function created from a 10^6 iteration Monte Carlo, bootstrap simulation using sampling with replacement in time and \dot{M} (Press et al. 1992).) This spectral peak and the visual inspection of the Figure 2.6 provide compelling evidence that, just as models predict, pulsed accretion events occur periodically near each periastron passage.

A second significant peak found at half the orbital period is powered by apastron accretion events. Most of the power at this frequency comes from the two closely separated LCO observations near orbital cycle 6.5. These two point are encircled in the top panel of

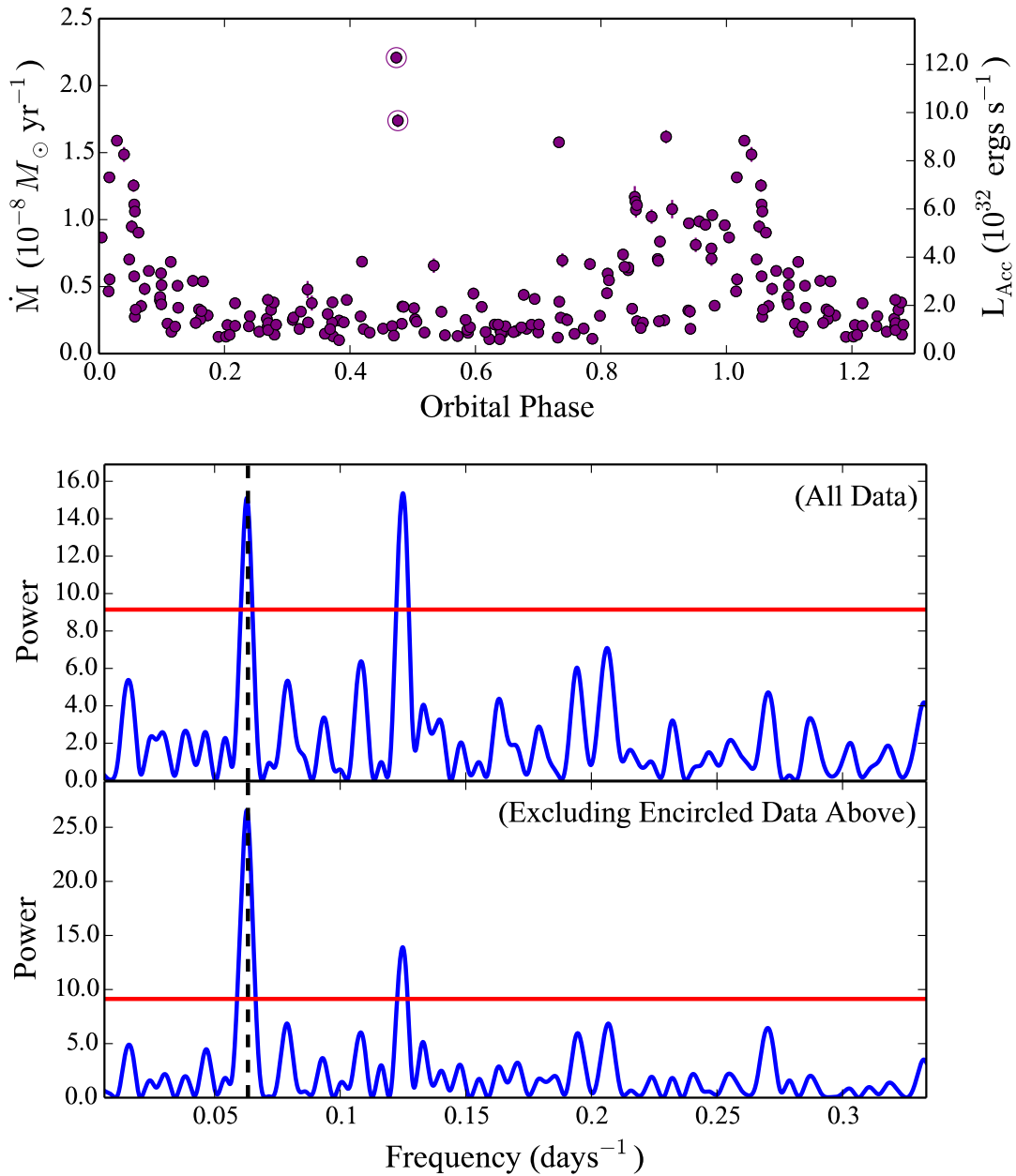


Figure 2.7 Top: Mass accretion rate (left axis) from LCO observations phase-folded about the orbital period. Right axis displays the corresponding accretion luminosity **Middle:** Lomb-Scargle periodogram of all of the above data. **Bottom:** Lomb-Scargle periodogram of the above data excluding the two encircled periastron points. In both periodograms the horizontal red line marks the 99% false-alarm-probability and the vertical dashed line is the radial-velocity determined orbital period.

Figure 2.7. (Other apastron accretion examples can be seen at orbital cycles 8.5 and 9.5 in Figure 2.6.) A periodogram excluding these two points is presented in the bottom panel of

Figure 2.7 where a peak is still present above the 99% FAP. Non-sinusoidal waveforms, like those observed, are capable of producing harmonics above a 99% FAP at integer multiples of the primary frequency. This is potentially the case in the bottom panel of Figure 2.7 but not in the middle panel where the peak at twice the orbital frequency is the highest of the two. We conclude that apastron accretion events are quasi-periodic, occurring at generally lower amplitudes and with less consistency when compared to periastron accretion events. Apastron accretion events are not predicted by the binary pulsed accretion theory and are discussed further in Section 2.4.3.

In addition to the presence of enhanced periastron accretion, the morphology and timing of the observed accretion events also provide a test of numerical simulations. Given that large variability exists from orbit to orbit we create an orbit-averaged accretion rate as a function of orbital phase. First, as to not over-weight the orbital periods with high-cadence observations, while still making use of the morphological information they provide, a linear interpolation of the mass accretion rate is computed and re-sampled at our average moderate-cadence rate (20 times per orbital period). The median value from 10 orbital periods is then calculated in phase bins of $\phi = 0.05$ (10 measurements per bin) resulting in the orbit average accretion event profile in Figure 2.8. The error bars at each bin signify the standard deviation within that bin from orbit-to-orbit. *On average*, accretion rates increase by a factor of ~ 5 above quiescence at periastron ($\phi = 0.95$ to 1.05) with a mostly symmetric rise and decay about periastron.

To compare our results directly with numerical simulations, we create an orbit averaged mass accretion rate from the ML2016 2D hydrodynamical models of binary accretion (D. Muñoz, private communication). These models are novel in that they utilize the adaptive mesh refinement code AREPO (Springel 2010), extend out to radii of $70a$, and run for >2000 orbital periods reaching full relaxation from the initial conditions out

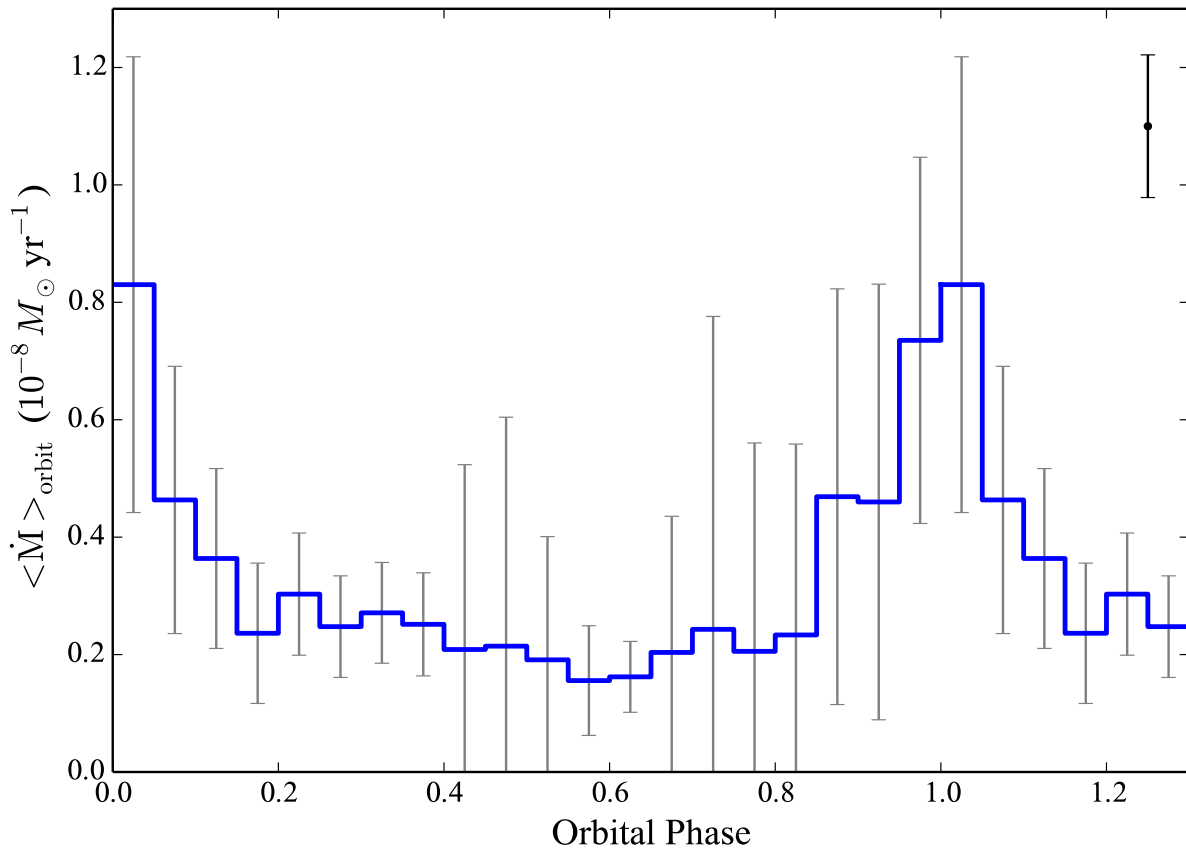


Figure 2.8 Orbit-averaged (median) mass accretion rate from 10 orbital cycles of observation. Error bars are the standard deviation within each phase bin. Black error bar in the top right corner denotes the propagation of the systematic error of our photometric calibration.

to a radius of $\sim 5a$ in the CBD. Using the results from 10 orbital periods of their scale-free, eccentric ($e = 0.5$), equal-mass binary simulation (similar to DQ Tau; $e = 0.568$; $q = 0.94$), we perform the same averaging scheme used on our observations. The simulated accretion rate is normalized by matching the average accretion rate per orbital period to our observations (Figure 2.6). Figure 2.9 presents a comparison of the model and data which, to first order, shows remarkable agreement given the limited input physics of the model (only gas physics and gravity). Both show significantly enhanced accretion from $\phi \sim 0.8$ to ~ 1.1 .

In detail however, the model and data differ in the specific morphology of the average

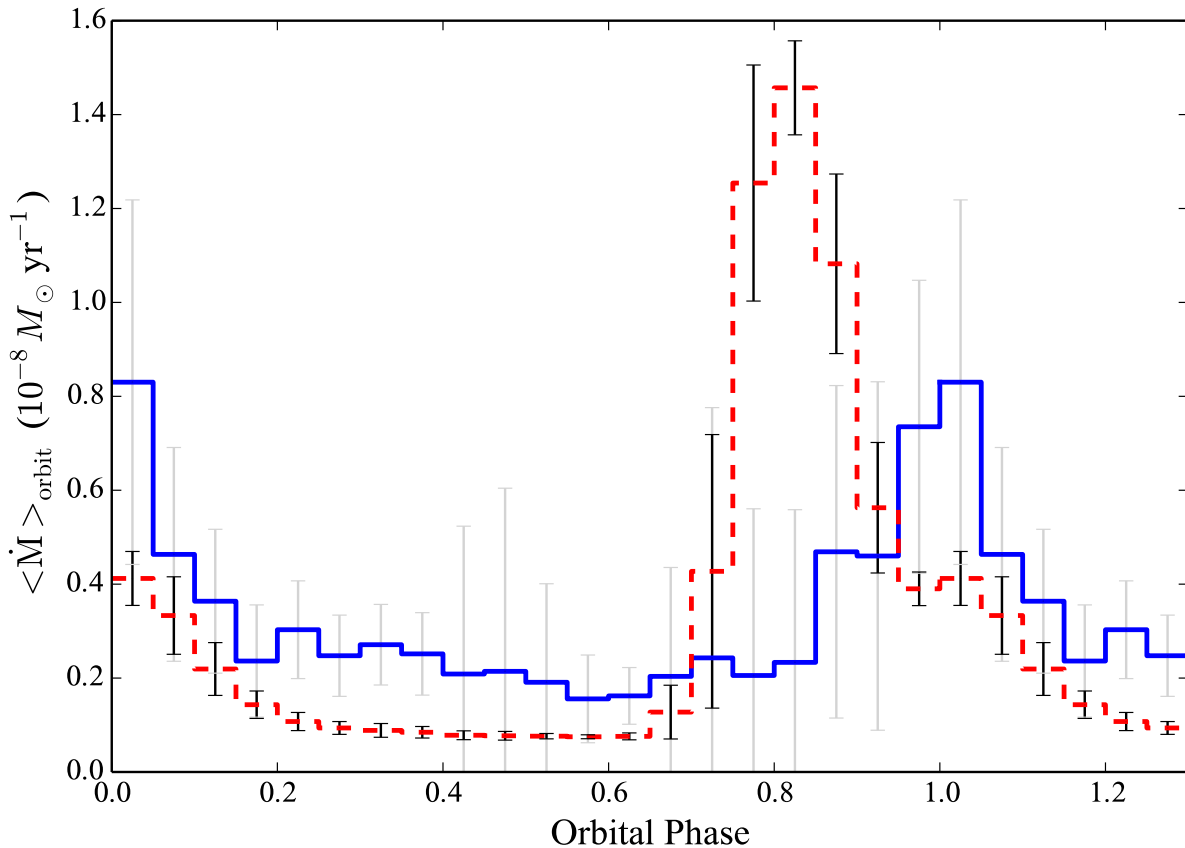


Figure 2.9 Orbit-averaged (median) mass accretion rate from 10 orbital cycles of observation and simulation in blue solid and red dashed lines, respectively. Error bars are the standard deviation of the accretion rate within each phase bin. Simulation results come from Muñoz & Lai (2016) 2D hydrodynamical models.

accretion event, the orbital phase of peak accretion, and the consistency of both compared to the observed variability (apparent when comparing the variability within each phase bin from the model to observations). Exploring these differences acts to highlight the important ingredients missing from numerical simulations. In the ML2016 simulations each star develops a tidally truncated circumstellar disk that extends down to the stellar radius where mass is deposited. With viscous accretion timescales as short as 20 orbital periods for disk of this size, circumstellar disks are replenished each orbital period by a circumbinary accretion stream. This process acts as an accretion buffer that organizes the incoming material before it reaches the stars. Bursts of accretion in this case arise not from

accretion stream material impacting the stars themselves but from companion-induced tidal torques on the circumstellar disks during periastron approach. These gravitational torques induce non-axisymmetric structures in the circumstellar disks (spiral arms) that dissipate orbital energy, funneling material inward.

In the case of DQ Tau however, strong magnetic fields may truncate the inner edge of the circumstellar disks, potentially to the point that no stable circumstellar orbits exist. Dynamical outer truncation radii for binary circumstellar disks are $\sim 0.2a$ or $\sim 5.6R_\star$ for DQ Tau’s orbital parameters (Eggleton 1983; Miranda & Lai 2015). As discussed above, the inner magnetospheric truncation radius is likely to vary with the conditions of incoming material but a typical single-star value is $R_{\text{in}} \sim 5R_\star$, essentially the same as the dynamical truncation. In this case, the efficiency of circumstellar material to buffer accretion streams would be greatly reduced leaving accretion events more subject to the timing and extent of material contained within each accretion stream.

This scenario explains the orbit-to-orbit consistency in amplitude and morphology the ML2016 simulation shows over our observations. The fact that the simulated accretion rates rise and peak well before ours is likely also due to the size/existence of circumstellar disks. If the material constituting DQ Tau’s periastron accretion events is provided by the accretion stream of that orbital period alone, there may be no circumstellar material laying in wait to be torqued by the companion star, delaying the onset of accretion. In addition, periastron passages 5 and 7 (Figure 2.6), for instance, display discrete accretion events at orbital phases 1.18 and 0.72, respectively, where companion-induced tidal torques are likely insignificant given the stellar separation.

It is possible that we have confirmed the observational predictions of numerical simulations without, necessarily, the same dominant physical mechanisms at play. Simulations including treatments of magnetism and radiative transfer may be required for a more in-

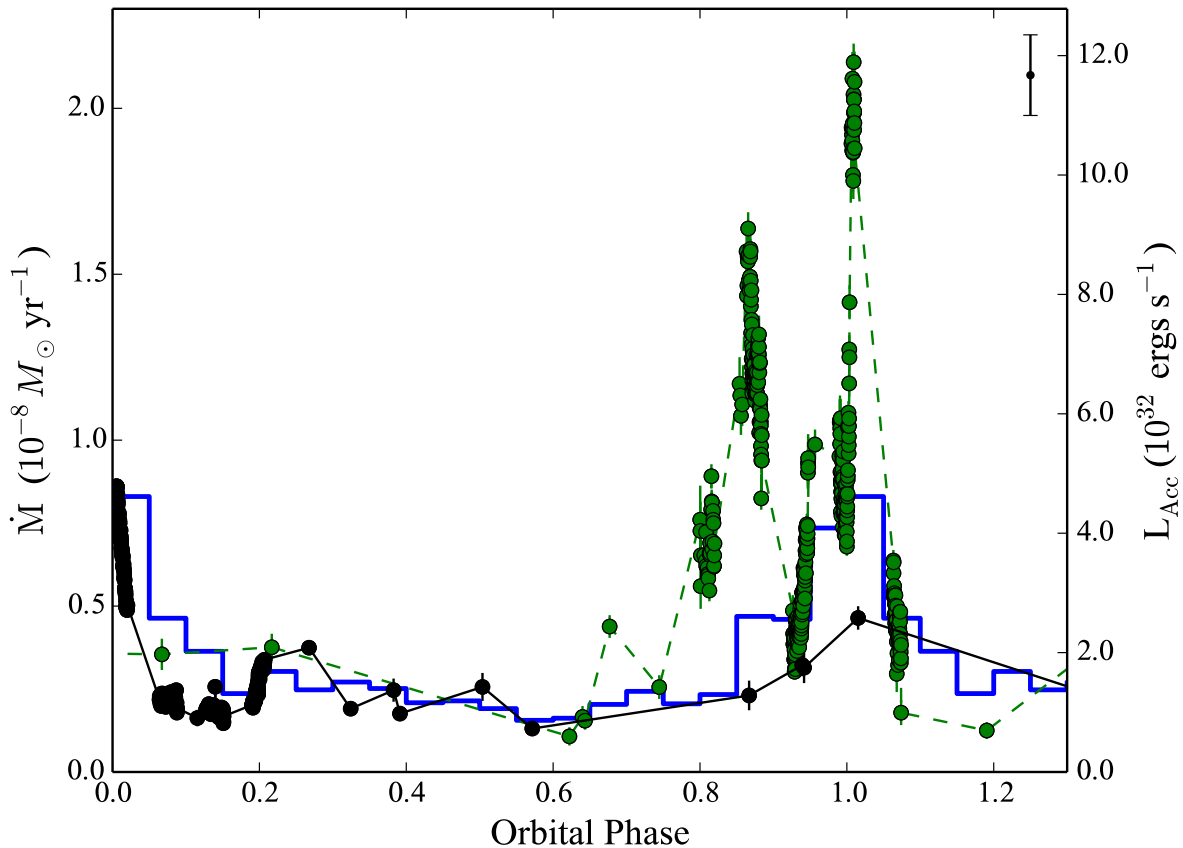


Figure 2.10 The mass accretion rate (left axis) of the most active and passive orbital periods. The green and black data are from orbital cycles 2 and 4, respectively. The blue histogram is orbit-averaged accretion rate from Figure 2.8. The right axis present the corresponding accretion luminosity.

depth comparison with short-period systems like DQ Tau. Long-period binaries where the magnetospheric inner truncation radius is less significant may be well described by these models.

2.4.2 Accretion Variability

The orbit-averaged accretion rate above provides definitive evidence that bursts of accretion primarily occur near periastron, consistent with the predictions of the binary pulsed accretion theory. However, the orbit-averaged accretion rate provides a very poor description of the behavior in a given orbit. Figure 2.10 highlights this variability,

presenting one of the more active and passive orbital periods.

Other than occurring primarily near periastron, accretion events vary in amplitude, duration, and morphology. Our high-cadence observations reveal that, rather than a single rise and decay across periastron, accretion occurs in discrete, short-lived events (Figure 2.10). In some sense, this behavior is not surprising given the large amount of variability seen in single CTTSs (Rucinski et al. 2008; Cody et al. 2014; Stauffer et al. 2014). The Kulkarni & Romanova (2008) 3D MHD simulations of Rayleigh-Taylor unstable accretion, for instance, provide a good qualitative match to the bursty and quasi-period nature of accretion on single CTTSs.

Inspection of the bottom panel of Figure 2.6 shows a factor of ~ 5 variability (min-to-max) in the mass accreted per orbital period. For reference, the ML2016 simulation only vary by $\sim 10\%$ from orbit-to-orbit. The source of this variability must come from either changes in the amount of CBD material supplied from one orbit to the next or changes in the efficiency at which the stars drain their reservoirs of material. If we assume the amount of material brought in through accretion streams is the same for every orbit and only the efficiency at which the stars accrete changes, we would expect orbital periods with low accretion to be followed by those with high accretion, fueled by “leftover” material. Although only 10 orbital cycles are observed, there does not appear to be any obvious connection between the mass accreted from one orbital period to the next.

If instead, each star accretes a majority of its bound material within an orbital period (the case if little/no stable circumstellar material exists), variability in the mass accreted per orbit would reflect variability in the mass supplied by the circumbinary streams. The time-variable nature of gravitational perturbations from an eccentric orbit creates a dynamic and unstable region near the CBD edge that could supply the inhomogeneities required to explain our observations. The ML2016 CBDs, for instance, develop asymmetries that

precess around the central binary as well as over-densities that grow, becoming unstable, and fall inward.

While changes in the stellar accretion efficiency and stream mass are likely both at play, we find the observed variability is most easily explained by assuming a significant portion of the circumstellar material is truncated near the star by magnetic fields, greatly inhibiting the ability to buffer, or hide, variability in accretion streams. This is supported by the variability in the accreted mass from orbit-to-orbit as well as the bursty and varied orbital phases of the near-periastron accretion events. The discrete nature of the observed accretion events (Figure 2.10) may also indicate an inhomogeneous nature to the material within a given stream that provides a non-steady flow of material to the stellar surface(s).

Changes in the magnetic field topology almost certainly plays a role in accretion variability as well. With large-scale magnetic reconnection events and time-variable ram pressure from accreting material, the state of the magnetic fields is largely unknown. We find it unlikely that the magnetic field alone could be responsible for suppressing the accretion rate to the degree that is observed in some orbital cycles, but it may affect the ability of the stars to capture stream material, alter the efficiency at which they drain the reservoir of circumstellar material, and foster the bursty nature of the observed accretion.

In addition to variability in the accretion rate itself, the spectral characteristics of the accretion luminosity is also variable. Figure 2.11 displays the color-magnitude diagram of the U -band excess emission versus the $U-B$ excess color. Here we see complex behavior where the $U-B$ excess color is not simply a function of the U -band excess, a proxy for the mass accretion rate. For a given U -band excess, a wide range of $U-B$ excess colors exists pointing to different physical conditions of emitting material for a single \dot{M} . Tightly grouped streaks in the color-magnitude diagram correspond to individual nights of high-cadence observation where we can see changes in not only the accretion rate, but also the

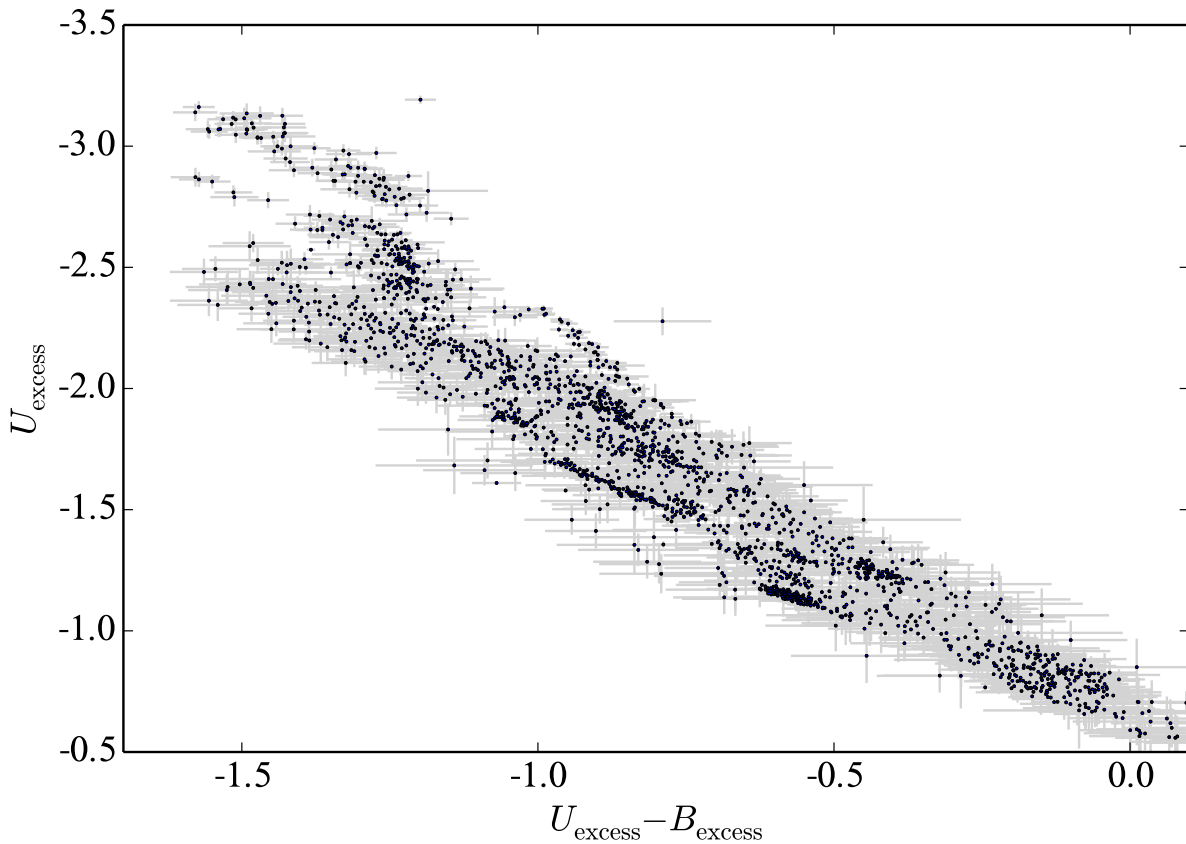


Figure 2.11 $U-B$ color of the excess accretion luminosity versus the U -band excess above the stellar photosphere (flares removed). The U -band excess luminosity is a proxy for the mass accretion rate. For given U -band excess a variety of $U - B$ excess colors are present.

conditions of accretion.

Calvet & Gullbring (1998) have modeled the emission of accreting CTTSs in the magnetic paradigm where, for a given mass and stellar radius, the emergent emission from an accretion column is set by its energy flux, $\rho v^3/2$, and surface filling factor (also see Ingleby et al. 2013). Increasing the energy flux of these models corresponds to an increase in the total emission, specifically blueward of the Balmer jump which, centered in the U -band, is likely the dominant source of $U - B$ excess color variability. Physically, this would require either a change in the density of the accreting material, its velocity, or the size of the accretion site. All three are likely to be changing in DQ Tau. Inhomogeneities in accretion

streams could affect the density of incoming material while simultaneously compressing the magnetic field to small R_{in} values which would correspond to small free-fall velocities (Equation 2.2). This variable accretion scenario is also likely to form Rayleigh-Taylor instabilities leading to unstable accretion flows which can increase the covering fraction of accretion sites (Kulkarni & Romanova 2008). It is also possible that both stars are accreting simultaneously under different conditions.

While our four-color photometry does not provide the spectral leverage to estimate changes in the energy flux or physical size of accretion sites, we note that when comparing the slope of the U -band light curve to the excess $U-B$ color, the rise of accretion events are consistently bluer than the decay. We interpret the bluer color as a larger emission blueward of the Balmer jump in the accretion spectrum, corresponding to a higher energy flux. This behavior suggests that the energy flux is higher at the onset of accretion events than during their decay.

2.4.3 Apastron Accretion Events

Outside of the predicted periastron accretion events, bursts of accretion also occur near periastron. This behavior was first observed in DQ Tau by Bary & Petersen (2014) and is not predicted by any models of eccentric binary accretion. Apastron events are less visually apparent in the light curve (Figure 2.6) than periastron events, but are present at a level capable of producing statistically significant periodicity at twice the orbital frequency (see Figure 2.8 and Section 2.4.1). Prominent examples can be seen at orbital cycles 6.5, 8.5, and 9.5 (Figure 2.6). While only three strong apastron events are seen, all three precede some, but not all, of the periastron passages with large integrated mass accretion.

We speculate that the source of the apastron events are either “leftovers” from inefficient draining during the preceding orbital cycle, or direct accretion from CBD. In the

ML2016 simulations, each star passes through the remnants of their companion’s unbound accretion stream near apastron that, without a buffering circumstellar disk, could lead to an accretion event. Alternatively, asymmetries in the CBD gap may also place material in the orbital path of the stars leading to direct accretion. If this scenario were the case, it might explain why subsequent periastron accretion events are large. A favorable alignment of the orientation of a CBD asymmetry at apastron passage might produce an apastron accretion event while placing more material than average under the gravitational influence of the star resulting in a larger accretion stream for the ensuing periastron.

2.5 Summary & Conclusions

With moderate-cadence photometry from LCO, supplemented with high-cadence photometry from the WIYN 0.9m and ARCSAT telescopes, we have obtained a comprehensive data set capable of characterizing variability and its physical mechanism in the T Tauri binary DQ Tau. Critically, our observations combine multi-orbit coverage, the time-resolution necessary to distinguish stellar flares from accretion variability, and *U*-band photometry capable of determining accretion rates.

Analysis of the light curve morphology reveals few events that resemble the characteristic shape of stellar flares. We develop a flare finding scheme aimed at detecting impulsive brightening events based on the characteristics of M dwarf flares that are then visually inspected. Two flares are identified, one classical and one gradual/slow above an average detection threshold of $\Delta U = 0.32$ mag. Modeling the classical flare with the Davenport et al. (2014) template places its integrated energy in good agreement with flares observed on other pre-MS stars. We find that optical flares are responsible for a very small portion of the optical variability, occurring in $\sim 3\%$ of our high-cadence coverage.

Under the assumption that the optical counterpart to the large mm-wave flares

observed by Salter et al. (2010) resemble those of active M dwarfs, we further conclude that magnetic reconnection events from colliding magnetospheres do not have a significant effect on the optical light curve. With the site of energy generation in these events occurring far from the stellar surfaces ($\sim 6R_\star$), the transport of energy to the photosphere to create an optical counterpart (the classical solar/stellar flare scenario) is complex and may suffer from confinement and energy losses. Even if that energy were deposited efficiently in the the stellar surface, the predicted energy budget from colliding magnetospheres is a factor of 10^3 less than the observed optical output near periastron. The two flares events that are found are in all likelihood magnetic reconnection events in a single magnetosphere near the stellar surface.

Removing the contribution from flares, we characterize the accretion variability in DQ Tau by converting the U -band excess luminosity into an accretion rate. Statistically significant periodicity in the mass accretion rate is present at the orbital period, powered by consistent periastron accretion events, that confirms the theoretical prediction of accretion in eccentric binaries. During some orbits, 90% of the mass accreted in that orbital period occurs near periastron ($\phi=0.7-1.3$). We determine the median accretion rate as a function of orbital phase to characterize the average morphology and amplitude of accretion events. On average, accretion rates increase by a factor of 5 near periastron. This result is in good agreement with the Muñoz & Lai (2016) hydrodynamical models.

Moving beyond the orbit-averaged accretion rate, we find complex variability from one orbital passage to the next. Broadly speaking, the results of hydrodynamic simulations match our observations, supporting the picture that streams of circumbinary disk (CBD) material are periodically brought into the central gap that feed accretion events near periastron. In detail however, the way in which these flows interact with the stars is more complex than the models depict. The scale of DQ Tau's orbit results in a close

match between inner and outer truncation radii of a circumstellar disk; the inner set by the stellar magnetosphere and the outer set by orbital resonances. The lack of extensive, stable circumstellar disks around the DQ Tau primary and secondary leaves accretion responsive to variability in the streams themselves and therefore the CBD. A picture emerges of inhomogeneity at the inner edge of the CBD providing streams to the central binary that are variable in mass from one orbit to the next, and streams that are non-steady or discrete in nature. These inhomogeneities translate into variations in the amount and timing of material accreted per orbital period and the discrete, bursty nature of the observed accretion events. Variability in the spectral characteristics of the accretion events reveal changes in the combined density and velocity (energy flux) of accretion flows as well as physical size of the accretion column. We attribute this behavior as changes in the characteristics of the accretion streams and their impact on the topology of the stellar magnetic fields.

Quasi-periodic accretion events near apastron are also observed. Elevated apastron accretion has been detected in DQ Tau previously (Bary & Petersen 2014), but this is the first time in which these events are seen to be (quasi-)periodic in nature. In general, they occur less frequently and at smaller amplitudes when compared to periastron accretion. Although apastron accretion events are not predicted by the binary accretion theory, they may be a unique feature of very-short-period, eccentric binaries where the absence of stable circumstellar material leads to direct accretion of unbound material within the CBD gap or from CBD material itself in the orbital path.

While confronting the complex nature of binary accretion is daunting from both an observational and theoretical perspective, efforts to characterize these types of systems have far-reaching implications for accretion, disk physics, binary stellar evolution, and planet formation in the binary environment.

As co-authors on the published version of this work, I would like to acknowledge the guidance and input of Robert Mathieu, David Ardila, Rachel Akeson, David Ciardi, Christopher Johns-Krull, Gregory Herczeg, and Alberto Quijano-Vodniza. I would also like to thank Diego Muñoz and Dong Lai for providing the results of their simulations and for many useful discussions. I thank Suzanne Hawley and the Astrophysical Research Consortium (ARC) for their generous allocation of ARCSAT commissioning time as well as Flynn Hasse and the WIYN 0.9m synoptic observers, Stephen Gilliam, François Dufour, and William Romanishin. This work makes use of observations from the LCO network and observations obtained with Apache Point Observatory's 0.5-m Astrophysical Research Consortium Small Aperture Telescope. I gratefully acknowledge support from a Sigma Xi Grant-in-Aid of Research and the University of Wisconsin–Madison Graduate School.

References

- Adams, F. C., Cai, M. J., Galli, D., Lizano, S., & Shu, F. H. 2011, *ApJ*, 743, 175
- Alcalá, J. M., Natta, A., Manara, C. F., et al. 2014, *A&A*, 561, A2
- Alencar, S. H. P., Teixeira, P. S., Guimarães, M. M., et al. 2010, *A&A*, 519, A88
- Alexander, R., Pascucci, I., Andrews, S., Armitage, P., & Cieza, L. 2014, *Protostars and Planets VI*, 475
- Allred, J. C., Hawley, S. L., Abbett, W. P., & Carlsson, M. 2006, *ApJ*, 644, 484
- Andrews, S. M., Wilner, D. J., Espaillat, C., et al. 2011, *ApJ*, 732, 42
- Artymowicz, P., & Lubow, S. H. 1994, *ApJ*, 421, 651
- . 1996, *ApJL*, 467, L77
- Aschwanden, M. J., Schwartz, R. A., & Dennis, B. R. 1998, *ApJ*, 502, 468
- Baraffe, I., Homeier, D., Allard, F., & Chabrier, G. 2015, *A&A*, 577, A42
- Bary, J. S., & Petersen, M. S. 2014, *ApJ*, 792, 64
- Basri, G., Johns-Krull, C. M., & Mathieu, R. D. 1997, *AJ*, 114, 781
- Beck, T. L., Bary, J. S., Dutrey, A., et al. 2012, *ApJ*, 754, 72
- Bertin, E., & Arnouts, S. 1996, *Astron. Astrophys. Suppl. Ser.*, 117, 393
- Boden, A. F., Akeson, R. L., Sargent, A. I., et al. 2009, *ApJL*, 696, L111
- Bouvier, J., Covino, E., Kovo, O., et al. 1995, *A&A*, 299, 89

- Brown, J. C. 1971, *Sol. Phys.*, 18, 489
- Brown, T. M., Baliber, N., Bianco, F. B., et al. 2013, *PASP*, 125, 1031
- Butler, C. J., Erkan, N., Budding, E., et al. 2015, *MNRAS*, 446, 4205
- Calvet, N., & Gullbring, E. 1998, *ApJ*, 509, 802
- Cardelli, J. A., Clayton, G. C., & Mathis, J. S. 1989, *ApJ*, 345, 245
- Carr, J. S., Mathieu, R. D., & Najita, J. R. 2001, *ApJ*, 551, 454
- Cody, A. M., Stauffer, J., Baglin, A., et al. 2014, *AJ*, 147, 82
- Czekala, I., Andrews, S. M., Torres, G., et al. 2016, *Astrophys. J.*, 818, 156
- Dal, H. A., & Evren, S. 2010, *AJ*, 140, 483
- Davenport, J. R. A., Hawley, S. L., Hebb, L., et al. 2014, *Astrophys. J.*, 797, 122
- de Val-Borro, M., Gahm, G. F., Stempels, H. C., & Pepliski, A. 2011, *Mon. Not. R. Astron. Soc.*, 413, 2679
- Eggleton, P. P. 1983, *ApJ*, 268, 368
- Fernández, M., Stelzer, B., Henden, A., et al. 2004, *A&A*, 427, 263
- Fletcher, L., Dennis, B. R., Hudson, H. S., et al. 2011, *Space Sci. Rev.*, 159, 19
- Frescura, F. A. M., Engelbrecht, C. A., & Frank, B. S. 2008, *MNRAS*, 388, 1693
- Gahm, G. F. 1990, in *IAU Symposium, Vol. 137, Flare Stars in Star Clusters, Associations and the Solar Vicinity*, ed. L. V. Mirzoyan, B. R. Pettersen, & M. K. Tsvetkov, 193–206

- Gómez de Castro, A. I., López-Santiago, J., Talavera, A., Sytov, A. Y., & Bisikalo, D. 2013, *ApJ*, 766, 62
- Grankin, K. N., Bouvier, J., Herbst, W., & Melnikov, S. Y. 2008, *A&A*, 479, 827
- Gullbring, E., Hartmann, L., Briceno, C., & Calvet, N. 1998, *ApJ*, 492, 323
- Günther, R., & Kley, W. 2002, *A&A*, 387, 550
- Harris, R. J., Andrews, S. M., Wilner, D. J., & Kraus, A. L. 2012, *ApJ*, 751, 115
- Hartmann, L., Hewett, R., & Calvet, N. 1994, *ApJ*, 426, 669
- Hawley, S. L., Davenport, J. R. A., Kowalski, A. F., et al. 2014, *Astrophys. J.*, 797, 121
- Hawley, S. L., & Pettersen, B. R. 1991, *ApJ*, 378, 725
- Herczeg, G. J., & Hillenbrand, L. A. 2008, *ApJ*, 681, 594
- . 2014, *ApJ*, 786, 97
- Honeycutt, R. K. 1992, *PASP*, 104, 435
- Ingleby, L., Espaillat, C., Calvet, N., et al. 2015, *ApJ*, 805, 149
- Ingleby, L., Calvet, N., Bergin, E., et al. 2011, *ApJ*, 743, 105
- Ingleby, L., Calvet, N., Herczeg, G., et al. 2013, *ApJ*, 767, 112
- Jensen, E. L. N., & Mathieu, R. D. 1997, *AJ*, 114, 301
- Jensen, E. L. N., Mathieu, R. D., & Fuller, G. A. 1996, *ApJ*, 458, 312
- Jester, S., Schneider, D. P., Richards, G. T., et al. 2005, *AJ*, 130, 873
- Johns-Krull, C. M. 2007, *ApJ*, 664, 975

- Johnstone, C. P., Jardine, M., Gregory, S. G., Donati, J.-F., & Hussain, G. 2014, MNRAS, 437, 3202
- Kenyon, S. J., Dobrzycka, D., & Hartmann, L. 1994, AJ, 108, 1872
- Kenyon, S. J., & Hartmann, L. 1995, ApJS, 101, 117
- Koen, C. 2015, MNRAS, 449, 1704
- Kowalski, A. F., Hawley, S. L., Carlsson, M., et al. 2015, Sol. Phys., 290, 3487
- Kowalski, A. F., Hawley, S. L., Holtzman, J. A., Wisniewski, J. P., & Hilton, E. J. 2010, Astrophys. J., 714, L98
- Kowalski, A. F., Hawley, S. L., Wisniewski, J. P., et al. 2013, ApJS, 207, 15
- Kraus, A. L., Ireland, M. J., Martinache, F., & Hillenbrand, L. A. 2011, ApJ, 731, 8
- Kulkarni, A. K., & Romanova, M. M. 2008, Mon. Not. R. Astron. Soc., 386, 673
- Lacy, C. H., Moffett, T. J., & Evans, D. S. 1976, ApJS, 30, 85
- Maíz Apellániz, J. 2006, AJ, 131, 1184
- Massi, M., Forbrich, J., Menten, K. M., et al. 2006, A&A, 453, 959
- Massi, M., Menten, K., & Neidhöfer, J. 2002, A&A, 382, 152
- Mathieu, R. D., Stassun, K., Basri, G., et al. 1997, AJ, 113, 1841
- Miranda, R., & Lai, D. 2015, MNRAS, 452, 2396
- Muñoz, D. J., & Lai, D. 2016, ApJ, 827, 43
- Oke, J. B., & Gunn, J. E. 1982, PASP, 94, 586

- Orlando, S., Bonito, R., Argiroffi, C., et al. 2013, *A&A*, 559, A127
- Osten, R. A., Hawley, S. L., Allred, J. C., Johns-Krull, C. M., & Roark, C. 2005, *ApJ*, 621, 398
- Panagi, P. M., & Andrews, A. D. 1995, *MNRAS*, 277, 423
- Pearce, G., & Harrison, R. A. 1990, *A&A*, 228, 513
- Pickles, A., & Depagne, É. 2010, *PASP*, 122, 1437
- Press, W. H., Teukolsky, S. A., Vetterling, W. T., & Flannery, B. P. 1992, *Numerical recipes in FORTRAN. The art of scientific computing*
- Raghavan, D., McAlister, H. A., Henry, T. J., et al. 2010, *ApJS*, 190, 1
- Rucinski, S. M., Matthews, J. M., Kuschnig, R., et al. 2008, *MNRAS*, 391, 1913
- Salter, D. M., Hogerheijde, M. R., & Blake, G. A. 2008, *A&A*, 492, L21
- Salter, D. M., Kóspál, Á., Getman, K. V., et al. 2010, *A&A*, 521, A32
- Scargle, J. D. 1982, *ApJ*, 263, 835
- Shu, F., Najita, J., Ostriker, E., et al. 1994, *ApJ*, 429, 781
- Springel, V. 2010, *MNRAS*, 401, 791
- Stauffer, J., Cody, A. M., Baglin, A., et al. 2014, *AJ*, 147, 83
- Strom, K. M., Strom, S. E., Edwards, S., Cabrit, S., & Skrutskie, M. F. 1989, *AJ*, 97, 1451
- Tomczak, M., & Ciborski, T. 2007, *A&A*, 461, 315
- Trigilio, C., Umana, G., & Migenes, V. 1993, *MNRAS*, 260, 903

Venuti, L., Bouvier, J., Flaccomio, E., et al. 2014, A&A, 570, A82

Williams, J. P., & Best, W. M. J. 2014, ApJ, 788, 59

Chapter 3

Pulsed Accretion in the T Tauri Binary

TWA 3A

*Success consists of going from failure
to failure without loss of enthusiasm.*

Winston Churchill

*A version of this chapter has previously appeared
in the Astrophysical Journal Letters
Tofflemire, et al. 2017, ApJL, 842, L12*

Abstract

TWA 3A is the most recent addition to a small group of young binary systems that both actively accrete from a circumbinary disk and have spectroscopic orbital solutions. As such, it provides a unique opportunity to test binary accretion theory in a well-constrained setting. To examine TWA 3A's time-variable accretion behavior, we have conducted a two-year, optical photometric monitoring campaign, obtaining dense orbital phase coverage (~ 20 observations per orbit) for ~ 15 orbital periods. From U -band measurements we derive the time-dependent binary mass accretion rate, finding bursts of accretion near each periastron passage. On average, these enhanced accretion events evolve over orbital phases 0.85 to 1.05, reaching their peak at periastron. The specific accretion rate increases above the quiescent value by a factor of ~ 4 on average but the peak can be as high as an order of magnitude in a given orbit. The phase dependence and amplitude of TWA 3A accretion is in good agreement with numerical simulations of binary accretion with similar orbital parameters. In these simulations, periastron accretion bursts are fueled by periodic streams of material from the circumbinary disk that are driven by the binary orbit. We find that TWA 3A's average accretion behavior is remarkably similar to DQ Tau, another T Tauri binary with similar orbital parameters, but with significantly less variability from orbit to orbit. This is only the second clear case of orbital-phase-dependent accretion in a T Tauri binary.

3.1 Introduction

TWA 3, also known as Hen 3-600, is a pre-main-sequence (pre-MS) star system composed of two spatially resolved components: TWA 3A, a spectroscopic binary hosting a circumbinary accretion disk, and TWA 3B, a diskless tertiary at a separation of $1''.5$ (~ 52.5 AU in projection; de la Reza et al. 1989; Jayawardhana et al. 1999; Andrews et al. 2010; Kellogg et al. 2017). This multi-star architecture offers a unique opportunity to investigate the impact multiplicity has on the distribution and evolution of circumstellar material during star formation. In this Letter we focus on the spectroscopic binary, TWA 3A, monitoring its accretion behavior in order to characterize accretion flows in the binary environment. Table 3.1 presents the relevant binary and disk characteristics for TWA 3A.

Binary and higher-order multiple systems are observed as a frequent outcome of star formation (Raghavan et al. 2010; Kraus et al. 2011). Our understanding of binary population statistics has advanced with large-scale imaging and spectroscopic surveys, yet the impact binarity has on the star-disk interaction and planet formation remains poorly understood. The ubiquity of binaries, along with the growing number of planets found in, and around, binary systems (Orosz et al. 2012; Kaib et al. 2013; Mugrauer et al. 2014), motivates a detailed characterization of the binary-disk interaction.

Close binaries deviate most from the single-star paradigm where orbital dynamics are capable of sculpting the distribution and flows of disk material. For systems with semi-major axes less than ~ 100 au, orbital resonances are capable of dynamically clearing a region of disk material around the binary, opening the possibility for three stable disks: a circumstellar disk around each star and an encompassing circumbinary disk (Artymowicz & Lubow 1994). Theory predicts that rather than completely damming the inflow of

material from the circumbinary disk, accretion will proceed in discrete, periodic streams that form at the inner edge of the circumbinary disk. These streams cross the cleared gap supplying mass to small circumstellar disks or accreting directly onto the stars themselves (Artymowicz & Lubow 1996; Günther & Kley 2002; Muñoz & Lai 2016).

The frequency of these streams and their impact on the stellar mass accretion rate are predicted to be highly dependent on the binary orbital parameters. Focusing on eccentric, equal-mass binaries, similar to TWA 3A, numerical simulations predict that every apastron

Table 3.1. TWA 3A System Characteristics

Parameter	Value	References
P (days)	34.87846 ± 0.00090	1
γ (km s^{-1})	$+10.17 \pm 0.40$	1
e	0.6280 ± 0.0060	1
T_{peri} (HJD-2,400,000)	52704.554 ± 0.063	1
a (R_{\odot})	46.51 ± 0.49	1
$q \equiv M_2/M_1$	0.841 ± 0.014	1
M_1 (M_{\odot})	0.6027 ± 0.0207	1
M_2 (M_{\odot})	0.5072 ± 0.0158	1
Periastron Separation (R_{\odot})	17.30 ± 0.33	1
Apastron Separation (R_{\odot})	75.72 ± 0.85	1
i_{disk} ($^{\circ}$)	36	2
Disk M_{dust} (M_{\odot})	7×10^{-6}	2
$v \sin i$ (km s^{-1})	20	3
d (pc)	30 ± 3	1,4 ^a
A_V	0.04 ± 0.3	5

References. — ¹Kellogg et al. (2017, assuming $i_{\text{binary}}=i_{\text{disk}}=36^{\circ}$), ²Andrews et al. (2010), ³Torres et al. (2003), ⁴Ducourant et al. (2014), ⁵This work

^aKinematic distance derived using the Ducourant et al. (2014) position, proper motion, and convergent point with the Kellogg et al. (2017) γ velocity.

passage ($\phi=0.5$) will induce a stream of circumbinary material that leads to an accretion event near periastron passage ($\phi=0;1$). These episodes are predicted to increase the specific accretion rate by up to a factor of 10. This periodic accretion behavior has been observed in the T Tauri binary DQ Tau (Mathieu et al. 1997; Tofflemire et al. 2017).

The accretion streams predicted by the binary-disk interaction are likely important astrophysical phenomena at a variety of scales. From giant planet formation spurring streams across disk gaps (Lubow & D’Angelo 2006) to accretion onto binary black holes (Bowen et al. 2017), the same physical processes are at play. Interferometry and adaptive optics techniques are beginning to spatially resolve such structures in pre-MS systems (Beck et al. 2012; Casassus et al. 2013; Yang et al. 2017), but they are unable to describe their temporal characteristics. Accretion in short-period, pre-MS binaries offers a unique regime to probe the dynamics of accretion streams.

3.2 Observations & Data Reduction

In order to characterize the accretion behavior of TWA 3A, we have conducted a long-term, moderate-cadence, optical photometric monitoring campaign using the Las Cumbres Observatory (LCO) and SMARTS queue-scheduled facilities.

3.2.1 LCO 1m Network

The LCO 1m network comprises nine 1m telescopes located across four global sites: Siding Springs Observatory (Australia), SAAO (South Africa), CTIO (Chile), and McDonald Observatory (USA). Spanning ~ 12 TWA 3A orbital periods, our observations were made between 2014 May and 2016 April. Observing visits were scheduled 20 times per orbit while the target was visible (airmass < 2), corresponding to a cadence of 42 hr. Each visit consisted of three images in the *UBVR* filters. All data are reduced by the

LCO pipeline applying bad-pixel, bias, dark, and flat-field corrections. The three images per filter per visit are then aligned, combined, and fit with astrometric solutions using standard IRAF tasks.

3.2.2 SMARTS 1.3m

The SMARTS 1.3m telescope at CTIO is outfitted with the ANDICAM detector. Our program requested every-other-night visits of TWA 3A while it was visible (airmass < 2) between 2014 December and 2016 July. Each visit consisted of three images in the B and V filters. Data are reduced with the SMARTS pipeline, which applies bias and flat-field corrections. Each set of images per visit are aligned, combined, and fit with an astrometric solution using standard IRAF tasks.

3.2.3 Photometry and Calibration

For each telescope (LCO; SMARTS) and filter set ($UBVR$; BV), SExtractor (Bertin & Arnouts 1996) is used to perform automated source detection and photometry on each image producing time-series instrumental magnitudes. A source catalog for each data set is then created from spatial matching of the astrometric solutions. Due to poor seeing and/or telescope focus, flux from TWA 3A and TWA 3B could not be consistently separated. As such, SExtractor parameters were optimized to photometer the entire TWA 3 system.

Each source catalog is then fed into an ensemble photometry routine following the Honeycutt (1992) formalism. By selecting non-varying comparison stars interactively, variations from airmass and nightly observing conditions are corrected, resulting in relative-magnitude light curves for each star in the field of view (FOV). We note that this correction does not include color information, which leaves some small systematic error, especially in U -band where atmospheric corrections are most color dependent.

Relative ensemble magnitudes are then transformed to apparent magnitudes using non-varying stars in the LCO FOV for which published empirical or derived photometry exists. Five such stars are present in the LCO FOV (TYC 7213-797-1, 7213-391-1, 7213-1239-1, 7213-933-1, 7213-829-1). Their V magnitudes range from 11.18 to 11.57 and $(B-V)$ colors span 0.71 to 2.00. Using empirical measurements where available, we draw B and V values from the All-Sky Compiled Catalogue (Kharchenko 2001). For R -band, we use a colorless transformation from the Carlsberg Meridian Catalog 15 (CMC15 Niels Bohr Institute et al. 2014) r' to R ($R=r'-0.22\pm 0.12$) derived from 3690 overlapping stars between CMC15 and the Lowell Observatory Near-Earth Object Search (Skiff 2007). Without empirical U -band measurements available, we use the fitted apparent U -band magnitudes derived by Pickles & Depagne (2010). From these five stars we compute zero-point and color transformations that are applied to the rest of the field. Systematic errors associated with this calibration procedure are determined from the root-mean-squared deviation between the transformed published values of the calibrating stars in color-magnitude space. They are 0.18, 0.22, 0.25, and 0.07 mag for U , B , V , and R bands, respectively. (Systematic errors are propagated through the mass accretion rate derivation that follows and are presented in Figure 3.3.)

Not all five of the calibration stars in the LCO FOV are present in the smaller $6'$ FOV of the ANDICAM CCD. To transform the SMARTS data to apparent magnitudes, we bootstrap the apparent magnitudes derived for non-varying stars in the LCO FOV that overlap with the SMARTS FOV and use those to determine zero-point and color transformations.

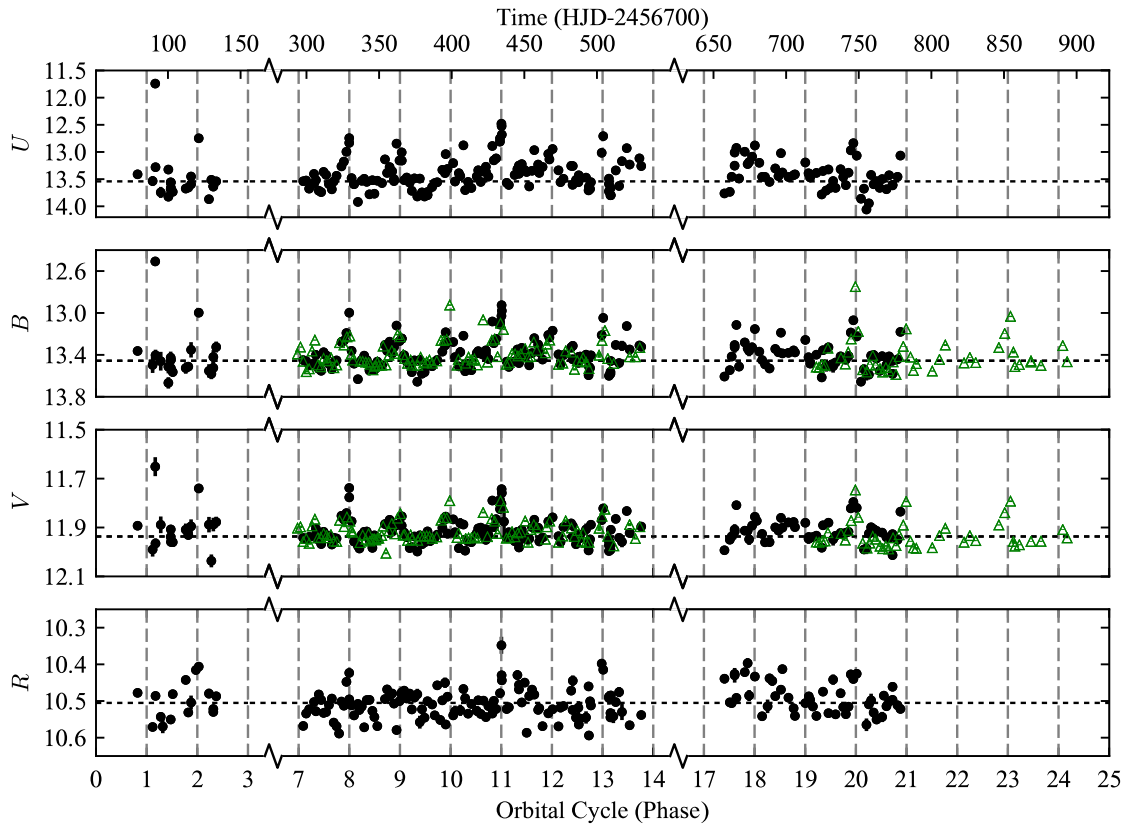


Figure 3.1 TWA 3 $UBVR$ light curves plotted against arbitrary orbital cycle number. The corresponding heliocentric Julian date (HJD) is presented on the top y-axis. LCO and SMARTS data are represented as circles and triangles, respectively. Vertical dashed lines mark periastron passages. Horizontal dashed lines mark the quiescent flux level.

3.3 Analysis

3.3.1 Light Curve Variability

Figure 3.1 presents the U -, B -, V -, and R -band light curves for TWA 3 plotted against an arbitrary orbital cycle number set to 1 for the first observed periastron passage. In each panel, vertical dashed lines mark the TWA 3A periastron passage and horizontal dotted lines mark the quiescent value (average of orbital phases 0.2 to 0.4). Brightening events near periastron passages are seen consistently, having the largest increase in U -band. These events very closely match the accretion behavior predicted for eccentric binaries.

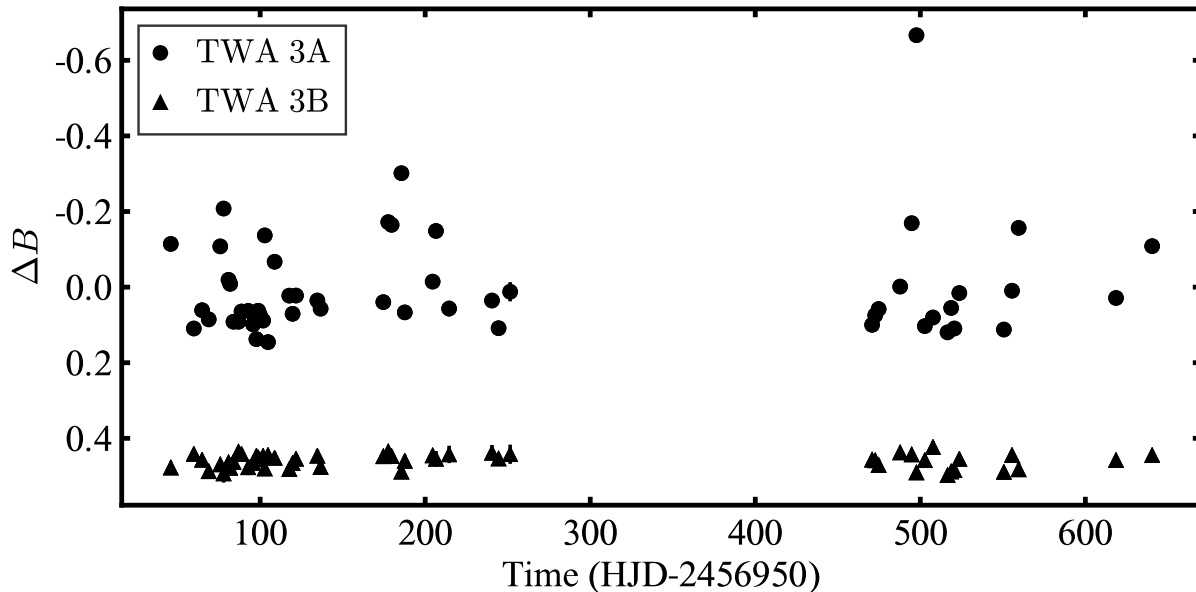


Figure 3.2 SMARTS B -band light curve of TWA 3A (circles) and TWA 3B (triangles) from observations in which point-spread-function photometry can separate the contribution from both components. The TWA 3A quiescent magnitude is ~ 0.38 mag brighter than TWA 3B.

To ensure variability observed in the TWA 3 system is indeed from the disk-bearing binary and not the tertiary, we perform point-spread-function photometry on a subset of the SMARTS B -band images where the light from each component can be reliably separated. Figure 3.2 displays the result where TWA 3A is the clear source of variability. The standard deviation of these light curves are 0.14 and 0.02 mag for TWA 3A and TWA 3B, respectively. In the following, we assume all variability in the TWA 3 system results from the spectroscopic binary.

Before assigning all optical variability to changes in the TWA 3A accretion rate, we inspect our light curves for contributions from stellar flares (magnetic reconnection events at stellar surfaces). In high-cadence photometry of DQ Tau, stellar flares with amplitudes greater than $\Delta U = 0.32$ mag were found to have a temporal contribution of $\sim 3\%$ (Tofflemire et al. 2017). Assuming the same contribution in TWA 3A corresponds to six measurements. In moderate-cadence photometry, however, these events would likely go undetected having

similar amplitudes and colors as accretion variability. Only if a measurement were to contain a large flare or a flare peak, where the photometric color is typically bluer than accretion, would it stand out from the underlying accretion variability (Kowalski et al. 2016).

One measurement in our light curves has a color, magnitude, and temporal behavior that suggest it contains a stellar flare. Occurring at orbital cycle ~ 1.2 in Figure 3.1, it is the brightest U -band measurement by 0.7 mag and the bluest in $(U-B)$ by 0.2 mag, well separated from both observed distributions. The associated flux would correspond to a factor of ~ 15 increase in the mass accretion rate compared to other measurements at similar orbital phases and a factor of two greater than the next highest measurement. A measurement only 5 hr later, however, falls securely within the remaining spread for that orbital phase. Accretion events of this scale are expected to be rare and to evolve over much longer timescales (e.g. Cody et al. 2014). And critically, the three U -band images combined in this measurement show a rapid ~ 0.2 mag decline over ~ 3 minutes. Given these characteristics, we conclude this measurement contains a stellar flare and remove it. In the following analysis, we assume the remaining variability is due to changes in the TWA 3A accretion rate.

3.3.2 Mass Accretion Rate

Flux-calibrated U -band photometry can be used to derive a mass accretion rate with knowledge of the distance and extinction to the source, the photospheric U -band flux in the absence of accretion, and the stellar mass and radius. With values for the distance and stellar parameters, we determine the extinction and photospheric properties following Herczeg & Hillenbrand (2014). First, we fit a spatially resolved Keck LRIS spectrum of TWA 3A (Herczeg et al. 2009) with a library of empirical weak-lined T Tauri star (WTTS)

spectra. The spectra are fit with three free parameters: a flux normalization, an additive accretion spectrum, and the extinction. Our results are consistent with those in Herczeg & Hillenbrand (2014), namely, $A_V=0.04$ (± 0.30 mag) and a combined TWA 3A spectral type of M4.1 (± 0.3 subclasses). Second, the best-fitting WTTS spectrum is convolved with a U -band filter to determine the underlying photospheric contribution of the binary.

Because our U -band measurements are for the entire TWA 3 system, we use a spatially resolved Keck LRIS spectrum of TWA 3B (Herczeg et al. 2009) to determine its U -band contribution. Assuming a distance of 30 pc, we extinction correct the U -band measurements and convert them to U -band luminosities. Subtracting the contribution from TWA 3B and the underlying TWA 3A photosphere, we arrive at the TWA 3A U -band accretion luminosity. Using the model-dependent, empirical relation derived in Gullbring et al. (1998), we calculate the total accretion luminosity from the U -band as follows:

$$\log(L_{\text{Acc}}/L_{\odot}) = 1.09 \log(L_{U_{\text{excess}}}/L_{\odot}) + 0.98. \quad (3.1)$$

For a single star, the mass accretion rate can be determined from the accretion luminosity with the following:

$$\dot{M} \simeq \frac{L_{\text{Acc}} R_{\star}}{GM_{\star}} \left(1 - \frac{R_{\star}}{R_{\text{in}}}\right)^{-1}, \quad (3.2)$$

where R_{in} is the magnetospheric disk truncation radius from which material free falls along magnetic field lines (typically assumed to be $5R_{\star}$; e.g. Johnstone et al. 2014).

Our measurements, however, are of the combined accretion luminosity from two stars with different masses and radii. Without a theoretical consensus for which star should predominantly receive the mass from circumbinary accretion flows, we assume that each star accretes at the same rate. The accretion luminosity emitted from the primary star alone, $L_{\text{Acc},1}$, becomes

$$L_{\text{Acc},1} = L_{\text{Acc,Total}} \left(1 + q \frac{R_{\star,1}}{R_{\star,2}}\right)^{-1}, \quad (3.3)$$

where q is the mass ratio. The total mass accretion rate for the binary is then

$$\dot{M} \simeq 2 \frac{L_{\text{Acc},1} R_{\star,1}}{GM_{\star,1}} \left(1 - \frac{R_{\star,1}}{R_{\text{in}}} \right)^{-1}. \quad (3.4)$$

For the stellar radii, we use the Dotter et al. (2008) stellar evolution models to compute the average radii for 0.6 and 0.5 M_{\odot} stars between 5 and 10 Myr. They are 1.06 and 0.99 R_{\odot} , respectively. R_{in} is set to the canonical single-star value of $5R_{\star}$. The derived accretion rates range between 0.8×10^{-11} and 2.4×10^{-10} $M_{\odot} \text{ yr}^{-1}$, in good agreement with previous measurements (Muzerolle et al. 2000; Herczeg et al. 2009). Since the stars have near equal masses, the choice to split the accretion rate equally between the two corresponds to only a $\pm \sim 5\%$ difference from assigning all the accretion to one star.

The top panel of Figure 3.3 presents the mass accretion rate phase-folded about the orbital period. The repeated enhanced accretion events observed near periastron increase the accretion rate by a factor of ~ 3 – 10 from the quiescent value.

3.3.3 Accretion Periodicity

To determine the significance of the periodic accretion behavior, we perform a Lomb-Scargle periodogram (Scargle 1982) on the accretion rate measurements. The bottom panel of Figure 3.3 presents the power spectrum. A significant peak is observed above the 99% false-alarm probability with a period of 34.67 ± 0.14 days, in good agreement (1.5σ) with the binary orbital period. (Error in the accretion rate period is derived from a 10^6 iteration Monte Carlo bootstrap simulation using random sampling with replacement of the \dot{M} and HJD measurement pairs Press et al. 1992.) Additional higher-frequency peaks occurring at two and three times the peak frequency result from the varying and non-sinusoidal morphology of the enhanced accretion events. The small peak to the left of the primary does not remain significant after filtering the data at the primary frequency.

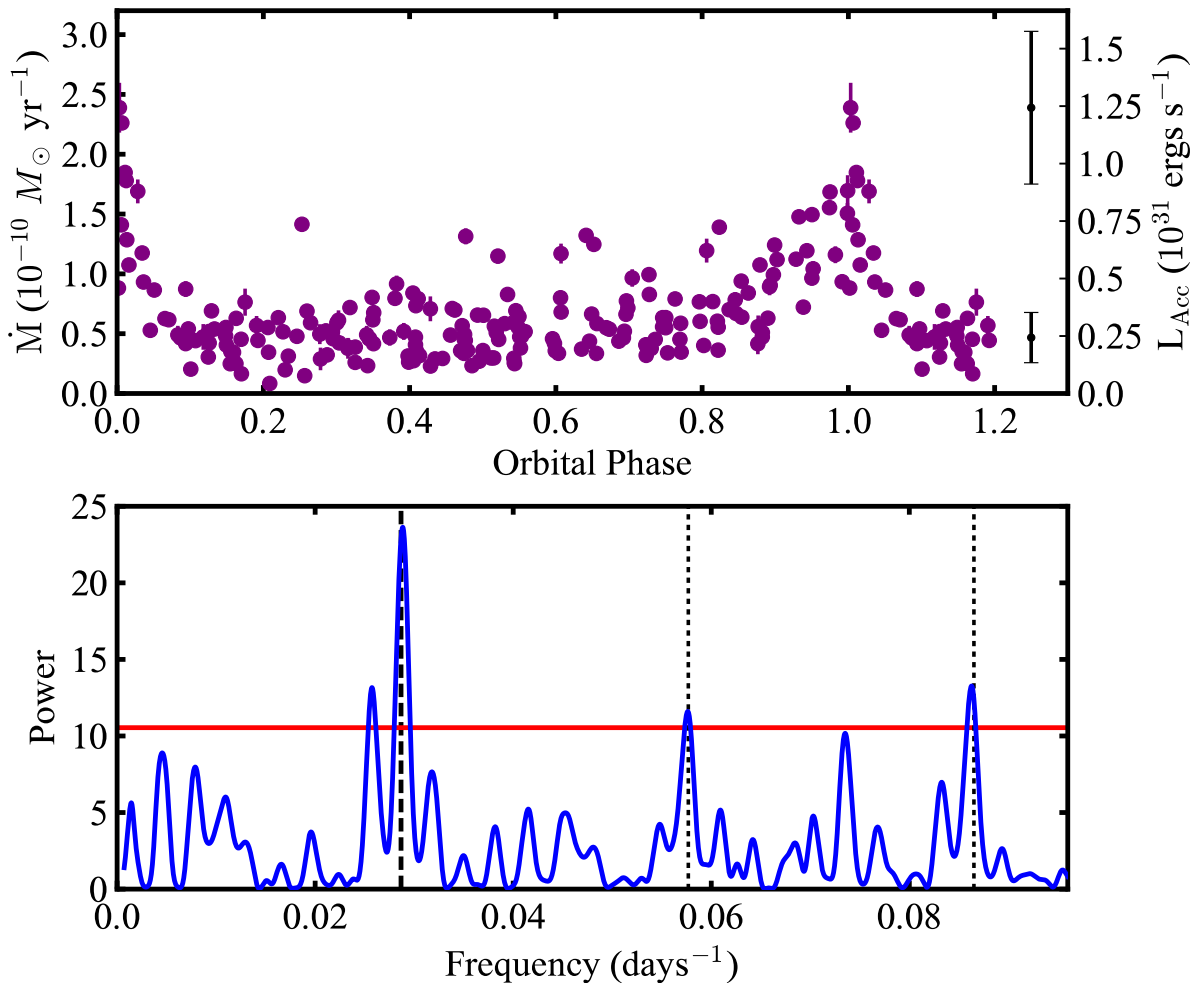


Figure 3.3 Top: TWA 3A mass accretion rate and accretion luminosity phase-folded about the orbital period. Black error bars on the right correspond to the propagation of the systematic error of our photometric calibration. Because the systematic error is relative, we present it for the quiescent and peak accretion rate values. **Bottom:** Periodogram of the mass accretion rate measurements. Significant power is found above the 99% false-alarm probability (horizontal red line) consistent with the orbital period (vertical dashed line).

3.3.4 Accretion Rate Profile

The morphology of enhanced accretion events contains information on the interaction between the binary orbit and the circumbinary mass flows. In order to compare our observations with numerical simulations, we create an average accretion rate profile as

a function of orbital phase. Breaking the orbital-phase-folded data into bins of $\phi=0.05$ (our sampling rate), we calculate the median mass accretion rate for each bin and set the bin error as its standard deviation. The result is presented in the top panel of Figure 3.4 where, on average, the accretion rate is elevated between orbital phases 0.85 and 1.05, reaching a peak near periastron of ~ 4 times the average quiescent value.

In the bottom panel of Figure 3.4 we compare the TWA 3A accretion rate profile to a simulation of binary accretion (Muñoz & Lai 2016) and to the DQ Tau accretion rate profile (Tofflemire et al. 2017). Both have been normalized to the TWA 3A average mass accretion rate. The Muñoz & Lai (2016) simulation shown is a 2D hydrodynamical model using the adaptive-mesh-refinement code AREPO (Springel 2010) for an equal-mass binary with an eccentricity of 0.5. Ten consecutive orbital periods of the simulation were used to create the accretion profile.

3.4 Discussion

Figures 3.3 and 3.4 provide conclusive evidence that accretion in TWA 3A is strongly influenced by the binary orbit, leading to periodic accretion bursts near periastron passage. This behavior is largely consistent with the prediction of numerical simulations supporting the scenario that periodic streams of mass are capable of carrying material across a cleared gap to the central binary. Similar behavior has only been this clearly observed in one other binary, DQ Tau. The binary UZ Tau E (Jensen et al. 2007) and the protostar LRL 54361 (Muzerolle et al. 2013, unknown period) are also intriguing sources that have shown hints of phase-dependent accretion.

Direct comparisons to numerical simulations can begin to constrain the dynamics of accretion streams. Despite a notable phase offset, there is good agreement between TWA 3A and the Muñoz & Lai (2016) model. Making more in-depth comparisons, however, is

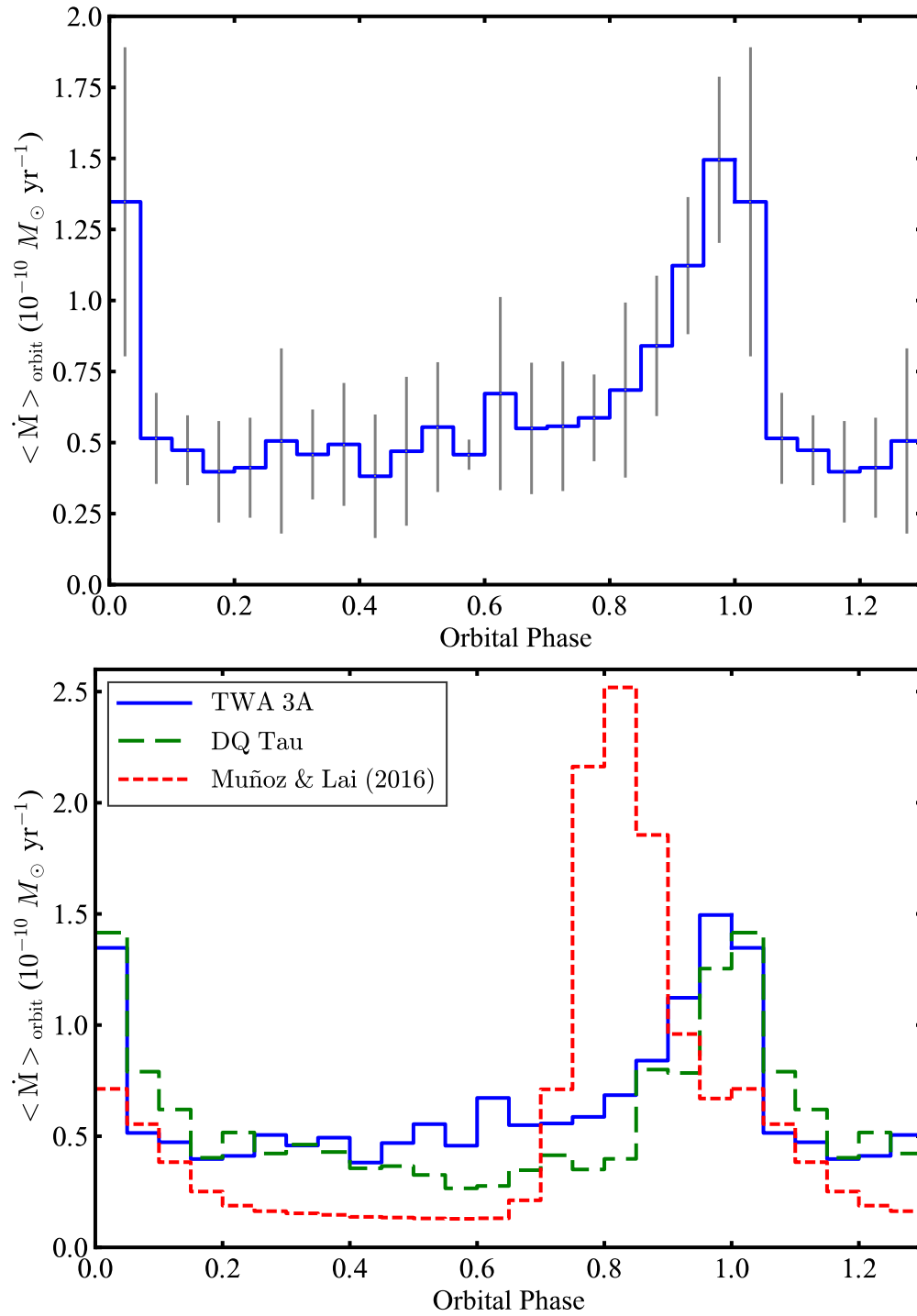


Figure 3.4 **Top:** TWA 3A median accretion rate as a function of orbital phase. Error bars represent the standard deviation within each phase bin. **Bottom:** Comparison of the TWA 3A accretion rate profile with DQ Tau (Tofflemire et al. 2017) and a numerical simulation from Muñoz & Lai (2016) for a binary with similar orbital parameters.

not straightforward. The difficulty lies in the relevant hydrodynamic and magnetic scales that effect stable circumstellar disk material in short-period systems.

In high-resolution hydrodynamic simulations, each star develops a stable circumstellar disk that collects and organizes incoming circumbinary stream material. Accretion events in this case result from a combination of tidal torques that each star induces on its companion's disk and the interaction of the circumbinary streams with the circumstellar disks. Without magnetic fields, material is accreted once it reaches the stellar surfaces. These stable circumstellar disks have the effect of regularizing accretion events from orbit-to-orbit.

In short-period systems, however, there is a close match between the outer dynamical truncation radii of circumstellar disks imposed by binary orbital resonances and the inner magnetic truncation radii typically assumed for single stars. If magnetic fields are capable of disrupting or reducing the size of stable circumstellar disks, there may be a direct interaction of stream material with the stellar magnetosphere that is not captured by current models.

We note that in lower-resolution simulations by Günther & Kley (2002), each star develops a marginally resolved circumstellar disk, yet their accretion rate profile peaks directly at periastron, matching the observations of TWA 3A and DQ Tau. It is unclear whether resolved circumstellar disks or different disk treatments (viscosity, radiative cooling, viscous heating, etc.) are responsible for these differences in the timing and amplitude of accretion events. Short of including magnetic fields in three dimensions, a study varying the disk properties and inner accretion radii would provide a more suitable comparison with the data presented here.

Finally, the TWA 3A and DQ Tau average accretion rate profiles are strikingly similar. Although they have similar orbital parameters, DQ Tau exhibits much more variability from orbit to orbit (compare Figure 3.3 to Figure 7 in Tofflemire et al. 2017). Yet, on average, their profiles are very similar in shape and amplitude. Regularity in TWA 3A accretion

events when compared to DQ Tau, may be the result of a lower overall accretion rate ($\sim 10^{-2}$), or perhaps its larger semi-major axis permits some amount of stable circumstellar disk material that regularizes accretion events.

3.5 Summary

With a long-term, densely sampled, optical photometric monitoring campaign, we have characterized the accretion behavior of the young binary TWA 3A. Here, we summarize the main results of our work:

1. Spatially resolved photometry reveals that accretion variability from the spectroscopic binary, TWA 3A, is the dominant source of optical variability in the combined light of the TWA 3 system.
2. From *U*-band observations we derive the TWA 3A mass accretion rate as a function of time. Periodic accretion events are observed near each periastron passage. On average, the accretion rate is elevated between orbital phases 0.85 to 1.05, reaching a peak of ~ 4 times the quiescent value.
3. The observed behavior is in good agreement with numerical simulations, providing strong evidence for periodic circumbinary accretion streams in TWA 3A. This is only the second clear case of orbital-phase-dependent accretion in a pre-MS binary.
4. These are some of the first data that can begin to constrain the dynamical properties of accretion flows. Comparisons with current models are limited, however, as they do not include the disruptive effect magnetic fields have on stable circumstellar disks.
5. The TWA 3A average accretion rate profile is remarkably similar to that of DQ Tau (a shorter-period system with similar mass ratio and eccentricity; Tofflemire et al.

2017) despite DQ Tau's larger variability from orbit to orbit.

As co-authors on the published version of this work I would like to acknowledge the guidance and input of Robert Mathieu, Gregory Herczeg, Rachel Akeson, and David Ciardi. I would like to thank Lisa Prato for providing the TWA 3A spectroscopic orbital solution prior to its publication. This work makes use of observations from the LCO network and the CTIO 1.3 m telescope operated by the SMARTS Consortium. This research has made use of the VizieR catalogue access tool, CDS, Strasbourg, France. I gratefully acknowledge funding from Sigma Xi Honors Society and from the University of Wisconsin-Madison Graduate School.

References

- Andrews, S. M., Czekala, I., Wilner, D. J., et al. 2010, *ApJ*, 710, 462
- Artymowicz, P., & Lubow, S. H. 1994, *ApJ*, 421, 651
- . 1996, *ApJL*, 467, L77
- Beck, T. L., Bary, J. S., Dutrey, A., et al. 2012, *ApJ*, 754, 72
- Bertin, E., & Arnouts, S. 1996, *Astron. Astrophys. Suppl. Ser.*, 117, 393
- Bowen, D. B., Campanelli, M., Krolik, J. H., Mewes, V., & Noble, S. C. 2017, *ApJ*, 838, 42
- Casassus, S., van der Plas, G., M, S. P., et al. 2013, *Nature*, 493, 191
- Cody, A. M., Stauffer, J., Baglin, A., et al. 2014, *AJ*, 147, 82
- de la Reza, R., Torres, C. A. O., Quast, G., Castilho, B. V., & Vieira, G. L. 1989, *ApJL*, 343, L61
- Dotter, A., Chaboyer, B., Jevremović, D., et al. 2008, *ApJS*, 178, 89
- Ducourant, C., Teixeira, R., Galli, P. A. B., et al. 2014, *A&A*, 563, A121
- Gullbring, E., Hartmann, L., Briceno, C., & Calvet, N. 1998, *ApJ*, 492, 323
- Günther, R., & Kley, W. 2002, *A&A*, 387, 550
- Herczeg, G. J., Cruz, K. L., & Hillenbrand, L. A. 2009, *ApJ*, 696, 1589
- Herczeg, G. J. & Hillenbrand, L. A. 2014, *ApJ*, 786, 97
- Honeycutt, R. K. 1992, *PASP*, 104, 435

- Jayawardhana, R., Hartmann, L., Fazio, G., et al. 1999, *ApJL*, 520, L41
- Jensen, E. L. N., Dhital, S., Stassun, K. G., et al. 2007, *AJ*, 134, 241
- Johnstone, C. P., Jardine, M., Gregory, S. G., Donati, J.-F., & Hussain, G. 2014, *MNRAS*, 437, 3202
- Kaib, N. A., Raymond, S. N., & Duncan, M. 2013, *Nature*, 493, 381
- Kellogg, K., Prato, L., Torres, G., et al. 2017, *ApJ*, 844, 168
- Kharchenko, N. V. 2001, *Kinematika i Fizika Nebesnykh Tel*, 17, 409
- Kowalski, A. F., Mathioudakis, M., Hawley, S. L., et al. 2016, *ApJ*, 820, 95
- Kraus, A. L., Ireland, M. J., Martinache, F., & Hillenbrand, L. A. 2011, *ApJ*, 731, 8
- Lubow, S. H., & D'Angelo, G. 2006, *ApJ*, 641, 526
- Mathieu, R. D., Stassun, K., Basri, G., et al. 1997, *AJ*, 113, 1841
- Muñoz, D. J., & Lai, D. 2016, *ApJ*, 827, 43
- Mugrauer, M., Ginski, C., & Seeliger, M. 2014, *MNRAS*, 439, 1063
- Muzerolle, J., Calvet, N., Briceño, C., Hartmann, L., & Hillenbrand, L. 2000, *ApJL*, 535, L47
- Muzerolle, J., Furlan, E., Flaherty, K., Balog, Z., & Gutermuth, R. 2013, *Nature*, 493, 378
- Niels Bohr Institute, U. o. C., Institute of Astronomy, UK, C., & Real Instituto y Observatorio de La Armada en San Fernando. 2014, *VizieR Online Data Catalog*, 1327

Orosz, J. A., Welsh, W. F., Carter, J. A., et al. 2012, *Science*, 337, 1511

Pickles, A., & Depagne, É. 2010, *PASP*, 122, 1437

Press, W. H., Teukolsky, S. A., Vetterling, W. T., & Flannery, B. P. 1992, *Numerical recipes in FORTRAN. The art of scientific computing*

Raghavan, D., McAlister, H. A., Henry, T. J., et al. 2010, *ApJS*, 190, 1

Scargle, J. D. 1982, *ApJ*, 263, 835

Skiff, B. A. 2007, *VizieR Online Data Catalog*, 2277

Springel, V. 2010, *MNRAS*, 401, 791

Tofflemire, B. M., Mathieu, R. D., Ardila, D. R., et al. 2017, *ApJ*, 835, 8

Torres, G., Guenther, E. W., Marschall, L. A., et al. 2003, *AJ*, 125, 825

Yang, Y., Hashimoto, J., Hayashi, S. S., et al. 2017, *AJ*, 153, 7

Chapter 4

Kinematics of Accretion in the T Tauri

Binary TWA 3A: Evidence for Preferential

Accretion onto the TWA 3A Primary

*Well I'm no hero, that's understood.
The only redemption I can offer, girl,
is beneath this dirty hood.*

Bruce Springsteen

To be submitted to the Astrophysical Journal

Abstract

We present time-series, high-resolution optical spectroscopy of the eccentric T Tauri binary TWA 3A. Our analysis focuses mainly on the velocity structure of the accretion tracing emission lines H α and He I 5876 Å as probes of the kinematic properties of binary accretion. We find accretion-tracing emission line strengths display the same orbital-phase dependent behavior found with time-series photometry. Namely, bursts of accretion near periastron passages which are in good agreement with numerical simulations of eccentric binary accretion. Away from periastron, our spectra are consistent with pure chromospheric emission suggesting the absence of accretion outside of discrete bursts. When accretion is present, the emission of He I 5876 Å consistently traces the velocity of the primary star. We interpret this as preferential accretion onto the TWA 3A primary. This results is in contrast to most numerical simulations which predict the secondary should be the dominant recipient of circumbinary accretion flows. Our finding may support a model in which the precession of an eccentric circumbinary disk gap alternates between preferentially supplying mass to the primary and secondary.

4.1 Introduction

Protoplanetary disks are integral to the formation of low-mass stars and planets. In the case of single stars, well-established theory has been developed describing the star-disk interaction (Koenigl 1991; Calvet & Hartmann 1992). In this model, a star's magnetic field mediates the inward flow of disk material, channeling it along field lines before impacting the stellar surface (Shu et al. 1994). The magnetic accretion scenario has been able to describe many of the observational characteristics of accreting systems, commonly referred to as classical T Tauri stars (CTTSs). Specifically, the presence of recombination line and continuum emission from shock-heated material (Hartmann et al. 1994; Gullbring et al. 1998), outflows of material in winds and jets (Hartigan et al. 1995), and the rotational evolution of pre-main sequence (pre-MS) stars (Shu et al. 2000; Sills et al. 2000; Gallet & Bouvier 2013). Much of the theory for disk evolution and stellar evolution in the pre-MS phase are underpinned by this theory of the star-disk interaction.

Binary systems, however, are a common outcome of star formation (Raghavan et al. 2010; Kraus et al. 2011) that have the ability to fundamentally alter the canonical star-disk interaction. This departure is most significant in the case of short-period systems where orbital resonances are capable of dynamically clearing the central region of disk material (Artymowicz & Lubow 1994). In this architecture, the viscous flow of disk material is predicted to give way to periodic streams that bridge the gap between a circumbinary disk and the central stars (Artymowicz & Lubow 1996; Günther & Kley 2002; de Val-Borro et al. 2011). For binaries with circular orbits, these streams are predicted to occur on the inner-disk orbital timescale, where a buildup of material becomes unstable and falls into the cleared region, leading to enhanced accretion (Farris et al. 2014).

In the presence of even slight eccentricities, circumbinary streams are predicted every orbital period as the binary apastron passages draw in material from the inner edge of the disk gap (Miranda et al. 2017). These streams fuel bursts of accretion whose timing and amplitude depend on the binary orbital parameters. In the case of highly eccentric binaries, like TWA 3A considered in this work, accretion bursts are predicted near each periastron passage that increase the specific accretion rate by a factor of ~ 10 (Muñoz & Lai 2016). Evidence for such orbit-modulated accretion has been shown in the eccentric binaries DQ Tau ($e=0.57$; Mathieu et al. 1997; Tofflemire et al. 2017a) and TWA 3A ($e=0.63$; Tofflemire et al. 2017b) through long-term photometric monitoring. Additionally, DQ Tau has also shown periodic increases in the level of absorption line veiling and H α luminosity near periastron (Basri et al. 1997).

While these observations provide a fair match to numerical simulations, they bring into question the exact way in which material reaches the stellar surface. In high-resolution hydrodynamic simulations, each star develops a small circumstellar disk that collects incoming stream material. Periastron accretion bursts in this scenario are driven more by tidal torques that each star induces on its companion’s disk rather than from the introduction of new material to their circumstellar disks via streams (Muñoz & Lai 2016). Short-period systems ($P \leq 35$ d), however, have close periastron passages (~ 10 stellar radii) and when considering the disruptive effect stellar magnetic fields have on inner disk material (assumed to truncate material at $\sim 5R_*$; Johnstone et al. 2014), it becomes unlikely that either star hosts a stable circumstellar disk. Under these binary orbital parameters, it is uncertain how stream material interacts with the stars and their magnetic fields. No simulations to date have ventured into this domain.

To gain further insight into accretion processes in short-period binaries, we have monitored the eccentric, T Tauri binary TWA 3A with high-resolution optical spectroscopy.

These observations overlap with the long-term, moderate-cadence photometry presented in Tofflemire et al. (2017b). Our observations focus on ~ 3 orbital periods in which we seek to characterize the kinematic properties of accretion during the rise of periastron accretion bursts. We achieve this through the analysis of accretion-tracing emission lines that probe the foot-points of magnetic accretion flows. We also investigate the emission of outflow-tracing lines with respect to variable accretion and orbital motion. These observations, coupled with the wealth of information known about this system make it a unique setting to constrain the dynamical properties of binary accretion.

4.2 The TWA 3 System

In this section we describe the stellar orbits and distribution of disk material in the young, hierarchical triple system TWA 3. Much of the following is a summary of the recent study by Kellogg et al. (2017), where we highlight their results for the inner binary, TWA 3A. Where relevant, we update certain measurements to include distance information from *Gaia* DR2 (Gaia Collaboration et al. 2016, 2018).

TWA 3 is a member of the ~ 10 Myr-old TW Hya association (Mamajek 2005), composed of an inner spectroscopic binary, TWA 3A, and an outer triple companion, TWA 3B, separated by $1''.55$ on the sky. With parallax distances of 36.6 pc and 37.3 pc for TWA 3A and 3B, respectively (see Appendix B.1), a geometric calculation suggests a separation of ~ 0.7 pc or $\sim 1.4 \times 10^5$ AU. While there remain uncharacterized systematic errors in *Gaia* DR2, the fractional uncertainties on both parallax measurements are small ($\sim 10^{-3}$). This value is much larger than the previous attempts to constrain the 3A–3B orbit would suggest (Kellogg et al. 2017). The relevance of this large separation for the current work is that the influence of TWA 3B on the inner binary and its disk material is negligible over the time scales we consider here.

The inner binary, TWA 3A, hosts an extended circumbinary disk with signatures of active accretion (Herczeg et al. 2009; Tofflemire et al. 2017b). TWA 3B, however, shows no evidence for disk material (Jayawardhana et al. 1999; Andrews et al. 2010) and has the spectral properties of a non-accreting, weak-lined T Tauri star (Herczeg & Hillenbrand 2014). Table 4.1 presents the TWA 3A spectroscopic orbital solution and properties of the circumbinary disk.

The distribution of stars and disk material in this system suggest that multiplicity has had a large influence on the system’s evolution. First, it is unclear what processes lead to circumstellar material surrounding one component of the system, TWA 3A, while not the other. Second, the TWA 3A circumbinary disk has been modeled as having inner and outer truncations (340 GHz; Andrews et al. 2010). The inner at ~ 0.3 AU is presumably formed by binary orbital resonances and agrees fairly well with the predicted inner disk gap of $2-3a$ (Artymowicz & Lubow 1994). The outer truncation is at a projected radius of ~ 20 AU, which possibly resulted from an interaction with TWA 3B.

And third, there is evidence that the TWA 3A binary orbital plane may be misaligned with the bulk of the circumbinary disk (Kellogg et al. 2017). A spatially resolved observation of TWA 3Aa–3Ab with VLTI/PIONEER (Anthonioz et al. 2015), coupled with the spectroscopic orbital parallax, results in two families of allowed inclinations. The first family has small mutual binary-disk inclinations, ψ , which include coplanarity ($\psi < 20^\circ$), while the second includes large mutual inclinations ($\psi \sim 90^\circ$).

Additional support for a higher binary inclination than the circumbinary disk (i.e. $i > 36^\circ$) comes from the mismatch between the dynamical mass assuming disk-binary coplanarity ($M_1=0.6 M_\odot$; $M_2=0.5 M_\odot$), and the observed spectral type of M3–M4, which would correspond to $\sim 0.3 M_\odot$ stars (Herczeg & Hillenbrand 2014). Even with known systematic offsets in measurements of pre-main sequence spectral types (see Gully-Santiago

et al. 2017 and references therein), these measurements disagree. Notably though, both families of solutions include inclinations that eliminate this tension.

As this study is aimed at characterizing the interaction between short-period binaries and their inner disk material, the mutual inclination of the binary and disk orbital planes is highly relevant. Analytic theory and numerical simulations of misaligned binary-disk

Table 4.1. TWA 3A System Characteristics

Parameter	Value	References
P (days)	34.87846 ± 0.00090	(1)
γ (km s^{-1})	$+10.17 \pm 0.40$	(1)
e	0.6280 ± 0.0060	(1)
ω ($^\circ$)	80.5 ± 1.2	(1)
T_{peri} (HJD-2,400,000)	51239.659 ± 0.063	(1) ^a
$a \sin i$ (R_\odot)	27.31 ± 0.39	(1)
$q \equiv M_2/M_1$	0.841 ± 0.014	(1)
$M_1 \sin^3 i$ (M_\odot)	0.1224 ± 0.0055	(1)
$M_2 \sin^3 i$ (M_\odot)	0.1030 ± 0.0043	(1)
$v \sin i$ (km s^{-1})	< 8	(1)
i_{binary} ($^\circ$)	$\sim 35 - 53$	(1) ^b
i_{disk} ($^\circ$)	36	(2) ^b
Disk M_{dust} (M_\odot)	7×10^{-6}	(2)
Parallax (mas)	27.31 ± 0.12	(3)
d (pc)	36.6 ± 0.1	(4)
A_V	0.04 ± 0.3	(5)

References. — (1) Kellogg et al. (2017), (2) Andrews et al. (2010), (3) Gaia Collaboration et al. (2018), (4) This work, following Astraatmadja & Bailer-Jones (2016) (see Appendix B.1), (5) Tofflemire et al. (2017b)

^aThe T_{peri} value presented is 42 orbital periods prior to the value in Kellogg et al. (2017), placing the earliest archival spectra at an orbital cycle of zero. The error is assumed to be the same.

^b $i-180^\circ$ ambiguity from unknown line of ascending nodes.

orbital planes have been developed recently to explain the growing observational evidence for binary-disk misalignments (e.g. KH 15D - Capelo et al. 2012; GG Tau - Cazzoletti et al. 2017; 99 Herc - Kennedy et al. 2012). In the low-misalignment regime, Juhász & Facchini (2017) find steady-state disk warps that agree with linear wave-propagation theory for misalignments $\psi < 30^\circ$ (Papaloizou & Lin 1995; Lubow & Ogilvie 2000). In this scenario, the inner part of the disk is coplanar with the binary orbit.

For larger misalignments ($\psi > 40^\circ$) the interaction between the binary and disk is predicted to become non-linear, producing a break in the disk at radii $\sim 10a$ that precesses around the binary’s angular momentum vector (Facchini et al. 2018). This precession can lead to retrograde motion at the disk break boundary that becomes dynamically unstable and leads to large accretion events on the precession timescale (many hundreds of binary orbital periods). While intriguing, none of the numerical simulations that probe the inner disk regions have been run long enough to reach a steady state. At the same time, Martin & Lubow (2017) find that low-mass disks around high-eccentricity binaries can quickly become polar given a large initial misalignment ($\psi \gtrsim 40^\circ$). The result of this process leaves the disk’s angular momentum vector parallel to the binary’s eccentricity vector, i.e. the apastron passage is directly out of the plane of the disk (also see Lubow & Martin 2018).

Comparing these two possible scenarios to the time-series photometry in Tofflemire et al. (2017b), we find that the agreement between the observed accretion variability to models of coplanar binary accretion, and also to DQ Tau (a binary with known binary-disk alignment; Czekala et al. 2016), supports modest mutual inclinations (i.e. a coplanar inner disk). For the remainder of this work we assume a binary inclination of $i_{\text{binary}}=44^\circ$ (average of the low-mutual inclination solutions) that is coplanar with the inner disk, and adopt the following system parameters: stellar masses of $0.37 M_\odot$ and $0.31 M_\odot$, and a semi-major axis of $39.3 R_\odot$ with periastron and apastron separations of 14.7 and $64.0 R_\odot$, respectively. We

set the radius of the primary and secondary stars to 0.86 and 0.80 R_{\odot} , respectively, from the average of Dotter et al. (2008) stellar evolution models with ages between 5–10 Myr at the corresponding masses. These choices and the updated distance slightly increase the mass accretion rate values presented in Tofflemire et al. (2017b), which assumed binary-disk coplanarity.

4.3 Observations & Data Reduction

From 2014 May to 2016 April, TWA 3 was the target of a multi-site, time-series monitoring campaign combining multi-color optical photometry and high-resolution optical spectroscopy. To show the relative sequencing of these two campaigns, Figure 4.1 presents the U -band light curve obtained from the Las Cumbres Observatory (LCO) 1m Network with spectroscopic observations from the Southern African Large Telescope (SALT) High Resolution Spectrograph (HRS) marked with vertical blue bands. Vertical dashed lines denote TWA 3A periastron passages.

The following subsections describe the observation and data reduction methods for SALT–HRS spectroscopy and LCO imaging. A description of archival optical spectroscopy that is also presented in this paper is included below.

4.3.1 SALT–HRS

Located at the SAAO observatory in Sutherland, South Africa, SALT is a fixed-elevation telescope with a 10-m class primary mirror. It hosts a suite of instruments that are located or fed at prime focus (Buckley et al. 2006). Observations of TWA 3 were made with the dual-beam, fiber-fed echelle, HRS (Bramall et al. 2010, 2012). In the medium-resolution mode, a 500 μm ($2''.2$) fiber is image-sliced into a vertical pseudo-slit providing spectral resolutions up to $R \sim 40,000$ across a broad optical wavelength range in a separate

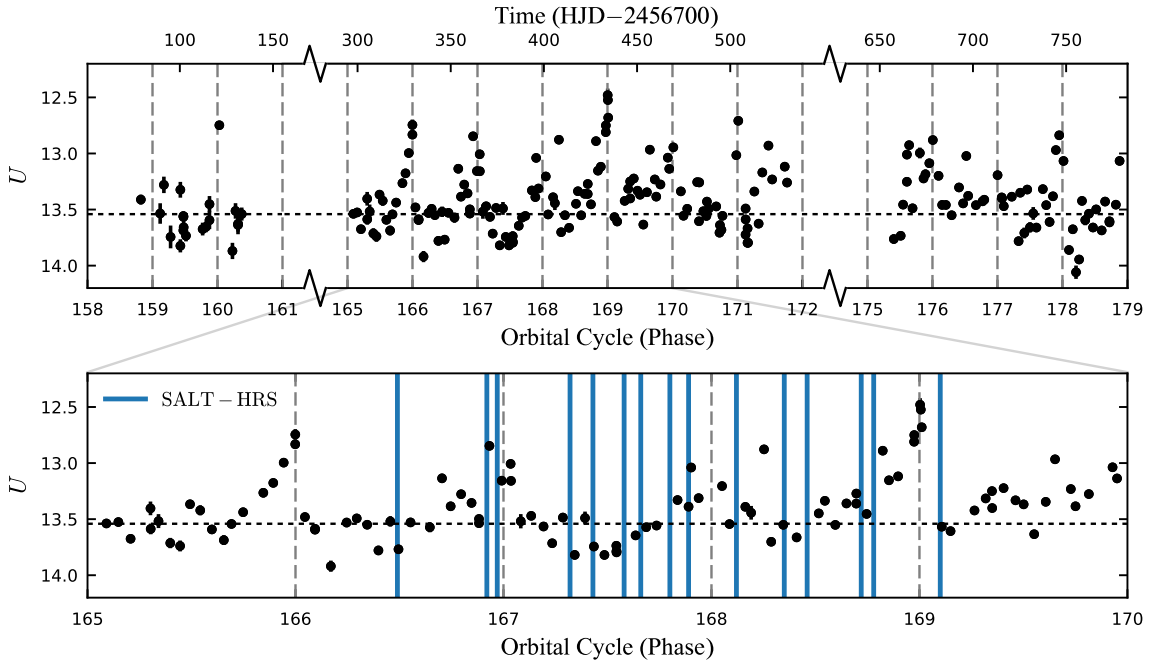


Figure 4.1 Overview of our LCO-SALT time-series monitoring campaign of TWA 3. **TOP:** Combined TWA 3A U -band light curve of as a function of TWA 3A orbital cycle on the bottom and heliocentric Julian date on the top x-axis. Vertical dashed lines mark TWA 3A periastron passages and the horizontal dotted line marks the quiescent U -band luminosity (average of orbital phases $\phi = 0.2$ – 0.4). These data were originally published in Tofflemire et al. (2017b). **Bottom:** A zoom-in of 5 TWA 3A orbital periods where SALT-HRS observations are denoted with vertical blue bands.

blue (3700–5500 Å) and red (5500–8900 Å) arm.

Critically for this study, SALT makes use of queue scheduling, allowing for observations of specific TWA 3A orbital phases spread over multiple orbital periods. Our observing program aimed to detect the rise of the accretion rate towards periastron by making targeted observations near apastron passages and at orbital phases leading up to, and just prior to, periastron passage. Over 107 days, 15 observations were made spanning ~ 3 TWA 3A orbital periods. Each visit consisted of three ~ 12 minute integrations with some variability due to the SALT track length. Table 4.2 presents the heliocentric Julian date of our SALT observations, their corresponding orbital phase, relevant spectroscopic measurements, and the mass accretion rate at the time of the observation (determined from an interpolation

of the nearest mass-accretion rate measurement derived from U -band photometry).

The reduction of HRS spectroscopy was performed with standard IRAF¹ tasks within a PyRAF script. Reduction steps include basic CCD calibrations (gain correction, over scan subtraction, bias subtraction, and image trimming), spectral flat correction, cosmic ray rejection (van Dokkum 2001), and a scattered light correction. The three target spectra per visit are then extracted and dispersion corrected by a nightly ThAr comparison spectrum before being median combined and blaze corrected by the extracted flat. Red-arm spectral orders are then combined, weighted by the blaze function.

In the blue arm, however, many orders do not detect the stellar continuum, or only detect it at the peak of the order’s throughput. Combining orders becomes problematic in this case, where the relative height of emission lines to the “continuum” is different in adjacent orders. For instance, an emission line in a low-sensitivity region of one order with no detected stellar continuum will have a relative height that is less than the same line in the adjacent order where continuum is detected. Combining these orders would artificially reduce the relative height and EW of the line. For this reason, blue-arm orders are not combined and the analysis of spectral lines is done in the order with the highest sensitivity.

We note that with SALT’s median seeing of $1''.3$ and HRS’s $2''.2$ fiber, our spectra contain light from TWA 3A and its tertiary companion TWA 3B. Below we note where the contribution of the companion’s light may be relevant.

¹IRAF is distributed by the National Optical Astronomy Observatory, which is operated by the Association of Universities for Research in Astronomy (AURA) under a cooperative agreement with the National Science Foundation.

Table 4.2. Dates, Equivalent Widths, and Mass Accretion Rates for SALT-HRS

Observations										
HJD	Orbital Phase	H α (\AA)	H β (\AA)	He I 5876 \AA (\AA)	[O I] 6300 \AA (\AA)	Li I 6707 \AA (\AA)	\dot{M} ($10^{-11} M_{\odot} \text{ yr}^{-1}$) ^a			
2457046.4476	166.49	-8.87 \pm 0.11	-5.64 \pm 0.04	-0.47 \pm 0.02	-0.26 \pm 0.02	0.56 \pm 0.02	6.4 \pm 0.6			
2457061.4090	166.92	-20.46 \pm 0.02	-9.82 \pm 0.04	-1.00 \pm 0.02	-0.22 \pm 0.01	0.56 \pm 0.01	26.4 \pm 1.0			
2457063.3984	166.97	-30.13 \pm 0.03	-10.56 \pm 0.05	-0.70 \pm 0.01	-0.24 \pm 0.01	0.54 \pm 0.01	24.2 \pm 0.8			
2457075.3713	167.32	-8.55 \pm 0.07	-7.08 \pm 0.05	-0.51 \pm 0.02	-0.26 \pm 0.01	0.54 \pm 0.01	7.4 \pm 0.7			
2457079.3610	167.43	-12.17 \pm 0.05	-7.30 \pm 0.07	-0.63 \pm 0.04	-0.29 \pm 0.02	0.56 \pm 0.01	6.7 \pm 0.6			
2457084.5985	167.58	-12.63 \pm 0.05	-6.19 \pm 0.08	-0.59 \pm 0.03	-0.29 \pm 0.02	0.54 \pm 0.02	6.4 \pm 0.5			
2457087.3351	167.66	-8.98 \pm 0.08	-5.99 \pm 0.04	-0.59 \pm 0.02	-0.25 \pm 0.01	0.61 \pm 0.01	8.6 \pm 0.5			
2457092.3205	167.80	-13.70 \pm 0.02	-8.24 \pm 0.05	-0.63 \pm 0.02	-0.32 \pm 0.01	0.55 \pm 0.01	13.0 \pm 0.6			
2457095.3155	167.89	-16.96 \pm 0.01	-9.43 \pm 0.05	-1.17 \pm 0.03	-0.38 \pm 0.01	0.56 \pm 0.01	13.6 \pm 1.0			
2457103.5442	168.12	-8.76 \pm 0.02	-7.48 \pm 0.04	-0.63 \pm 0.01	-0.29 \pm 0.02	0.54 \pm 0.01	11.5 \pm 0.7			
2457111.5225	168.35	-10.77 \pm 0.04	-8.20 \pm 0.04	-0.74 \pm 0.03	-0.36 \pm 0.02	0.54 \pm 0.01	9.6 \pm 0.5			
2457115.2590	168.46	-8.95 \pm 0.11	-5.44 \pm 0.10	-0.57 \pm 0.03	-0.18 \pm 0.02	0.48 \pm 0.01	9.7 \pm 0.6			
2457124.4924	168.72	-17.94 \pm 0.03	-10.09 \pm 0.05	-0.77 \pm 0.02	-0.40 \pm 0.01	0.59 \pm 0.01	14.3 \pm 0.5			
2457126.4848	168.78	-25.70 \pm 0.02	-12.83 \pm 0.05	-1.08 \pm 0.03	-0.37 \pm 0.01	0.57 \pm 0.01	19.7 \pm 0.7			
2457137.4515	169.10	-14.13 \pm 0.02	-10.69 \pm 0.05	-0.82 \pm 0.02	-0.34 \pm 0.01	0.50 \pm 0.01	11.7 \pm 0.6			

^aMass accretion rate interpolate from adjacent photometric measurements.

4.3.1.1 HRS Red Arm-Specific Reductions

In the SALT–HRS red arm, two separate distortions of the slit image are present that affect the width of the spectral resolution element across a given order. The first is that the width of the imaged slit is wider (larger FWHM) on the long-wavelength side of an order. This effect is minor and we do not correct for it.

The second is that the slit image is tilted by an angle that increases with pixel column (increasing toward the long-wavelength edge of the chip). This variable tilt causes significant spectral smearing that increases across the spectral order. This becomes problematic when combining adjacent orders where the resultant line shapes would depend on the combination of two different spectral resolutions.

In Appendix A.1 we provide a full description of our method for correcting this distortion. In short, we use the emission lines in Th-Ar comparison images to measure the horizontal pixel shift across the vertical extent of the slit. With multiple lines spanning the spectral order, we map the slit tilt (represented by an emission line’s peak across the vertical extent of the order) as a function of the pixel column (dispersion axis) and pixel row (slit axis). For each order, a function is fit to the slit location in each row that is used to perform a transformation along the pixel columns (dispersion axis). This amounts to a stretch or a compression, aligning it with the order’s center.

We note that this process involves interpolation which can introduce a covariance between pixels. This may be relevant in the determination of equivalent width (EW) uncertainties, which is discussed in Section 4.4.1. Flux conservation can also be a concern during interpolation, but with measures described in Appendix A.1, flux values are preserved to better than 1% in these transformations.

4.3.2 Archival Spectroscopic Observations

To determine whether the trends observed over the ~ 3 orbital periods monitored here are long lasting, we also compile archival observations of TWA 3, which are presented in Kellogg et al. (2017). Specifically, we make use of the FEROS spectra, which have similar wavelength coverage (3600 to 9200 Å), spectral resolution ($R \sim 44,000$), and orbital phase coverage to our SALT-HRS observations.

FEROS is a fiber-fed echelle spectrograph on the ESO 1.5m telescope in La Silla, Chile. Between 1999 March and 2000 July, 9 spectra were obtained spanning ~ 15 orbital cycles while sampling diverse orbital phases. Table 4.3 provides a list of the FEROS observation dates, their orbital cycle and phase, and measurements from selected spectral lines. For a full description of these data we refer readers to Kellogg et al. (2017). We note that due to the FEROS 2'' fiber, these spectra also contains light from TWA 3B.

4.3.3 LCO 1m Network

LCO is a network of queue-scheduled telescopes at multiple global sites that is able to provide near-continuous coverage of the night sky (Brown et al. 2013). Observations of

Table 4.3. Dates and Equivalent Widths of FEROS Observations

HJD	Orbital Phase	H α (Å)	He I 5876Å (Å)
2,451,260.5221	0.60	-13.26 ± 0.05	-0.96 ± 0.03
2,451,331.5915	2.64	-9.64 ± 0.05	-0.66 ± 0.02
2,451,621.5378	10.94	-41.17 ± 0.06	-1.57 ± 0.03
2,451,622.5731	10.98	-41.58 ± 0.11	-1.39 ± 0.03
2,451,623.6000	11.01	-21.54 ± 0.12	-1.67 ± 0.04
2,451,624.5913	11.04	-13.72 ± 0.07	-0.82 ± 0.03
2,451,625.5186	11.06	-10.54 ± 0.03	-0.70 ± 0.02
2,451,733.4665	14.16	-9.95 ± 0.03	-0.44 ± 0.02
2,451,737.5133	14.27	-11.71 ± 0.05	-0.57 ± 0.02

TWA 3 made use of three of the southern hemisphere sites hosting 1m telescopes: Siding Springs Observatory (Australia), SAAO (South Africa), CTIO (Chile).

With the goal of detecting fast changes in the binary accretion rate, while establishing the periodicity of periastron accretion bursts, we made observations spanning ~ 12 TWA 3A orbital periods obtaining roughly 20 visits per orbit (a cadence of ~ 42 hours). Each visit consisted of three images in each of a suit of filters. Only U -band photometry is discussed here; see Tofflemire et al. (2017b) for additional discussion of the BVR photometry. All data are processed by the LCO pipeline applying bad-pixel, bias, dark, and flat-field corrections.

Here we briefly describe our photometry and calibration schemes, referring interested readers to Tofflemire et al. (2017a,b) for a more thorough discussion. In short, source location and photometry are performed with SExtractor (Bertin & Arnouts 1996) providing time-series instrumental magnitudes. These are then input to an ensemble photometry routine following the Honeycutt (1992) formalism. Output differential ensemble magnitudes are then calibrated using non-variable stars in the LCO field-of-view for which empirical or derived photometry exists. From these stars, zero-point and color transformations are derived and applied to all stars in the field. In the U -band we derive a systematic error of 0.18 mag.

U -band photometry presented here is the combined light of the TWA 3 system (i.e. TWA 3A and TWA 3B). Flux from the two components could not be reliably separated at each epoch due to poor seeing and/or telescope focus. A subset of spatially resolved observations has shown TWA 3A to be the source of variability, however, and this is assumed to be the case throughout these data (Tofflemire et al. 2017b)

4.4 Results

In this section we begin by presenting equivalent-width (EW) measurements and their orbital phase dependence for selected lines. A more detailed analysis of the velocity structure of emission and absorption lines then follows.

4.4.1 Equivalent Width Measurements

For emission and absorption lines of interest we measure EWs by numerically integrating $(1 - F_\lambda/F_0)$ for line profiles above or below a locally determined continuum flux level. For accretion-tracing emission lines with variable widths, like H α , we integrate the continuous flux above the continuum level. For the absorption line Li I 6707 Å and the emission line [O I] 6300 Å, the integration is made over ± 60 km s⁻¹ from the line center in the binary center-of-mass rest frame. Measured EWs are provided in Tables 4.2 and 4.3. These measurements likely have a contribution from TWA 3B, but this component should be relatively constant across our sample.

EW uncertainties are determined with a Monte Carlo (MC) approach. Gaussian noise at the level of adjacent continuum regions is added to the spectrum and the EW is recomputed for 10^3 iterations. The standard deviation of these simulations is provided as the uncertainty in Tables 4.2 and 4.3. EW uncertainties may be underestimated for spectral lines in the red arm ($\lambda > 5500$ Å) due to a pixel-to-pixel covariance that is introduced in the image transformations described in Section 4.3.1.1 and Appendix A.1. However, the derived uncertainties do not differ greatly between red- and blue-arm measurements (e.g. H α and H β). It may be the case that low-level spectroscopic features in the “continuum” regions are a non-negligible source of the deviation used in our MC process.

A few of the lines discussed in this work suffer from terrestrial sky emission, namely [O I] 6300 Å and the Na I D doublet. Before measuring EWs or investigating the velocity

structure of these lines, we remove the terrestrial component by fitting a Gaussian and linear slope model to a narrow wavelength region centered on the sky emission. In practice, for nights with high sky emission, a two component Gaussian is required for lines that combined overlapping orders ($[\text{O I}] 6300 \text{ \AA}$) to account for the combination of slightly different resolution elements from the separate orders (see Section 4.3.1.1 and Appendix A.1).

Due to the limited track lengths of SALT observations, our HRS spectra do not consistently obtain detectable photospheric continuum levels at the shortest wavelengths of the blue arm. For this reason, we do not compute EWs for lines blueward of $\text{H } \beta$. For FEROS spectra we only measure $\text{H } \alpha$ and $\text{He I } 5876 \text{ \AA}$ lines for the same reason.

Figure 4.2 presents the EW measurements for the accretion-tracing emission lines $\text{H } \alpha$ and $\text{He I } 5876 \text{ \AA}$ as a function of orbital phase. Black and blue points mark SALT–HRS and FEROS observations, respectively. Most prominently seen in $\text{H } \alpha$, the increase in EW near periastron confirms the presence of enhanced accretion events previously observed with photometry in Tofflemire et al. (2017b).

During quiescence, the $\text{H } \alpha$ EW hovers between ~ -8 and -15 \AA . For M3-4 spectral types (similar to TWA 3A; Herczeg & Hillenbrand 2014; Kellogg et al. 2017), Fang et al. (2009) define an $\text{H } \alpha$ EW of -15 \AA as the boundary between classical and weak-lined T Tauri stars (WTTSs), meant to separate accreting and non-accreting systems. This $\text{H } \alpha$ EW value cleanly separates our observations into two groups based on their proximity to periastron. This behavior suggests that outside of periastron accretion events, stellar accretion may occur at very low rates, or be completely absent.

While a similar CTTS–WTTS boundary does not exist in the literature for $\text{He I } 5876 \text{ \AA}$ EWs, the same behavior is present where $\sim -0.8 \text{ \AA}$ may mark a similar chromosphere-accretion boundary. The contribution of chromospheric emission will be relevant for our

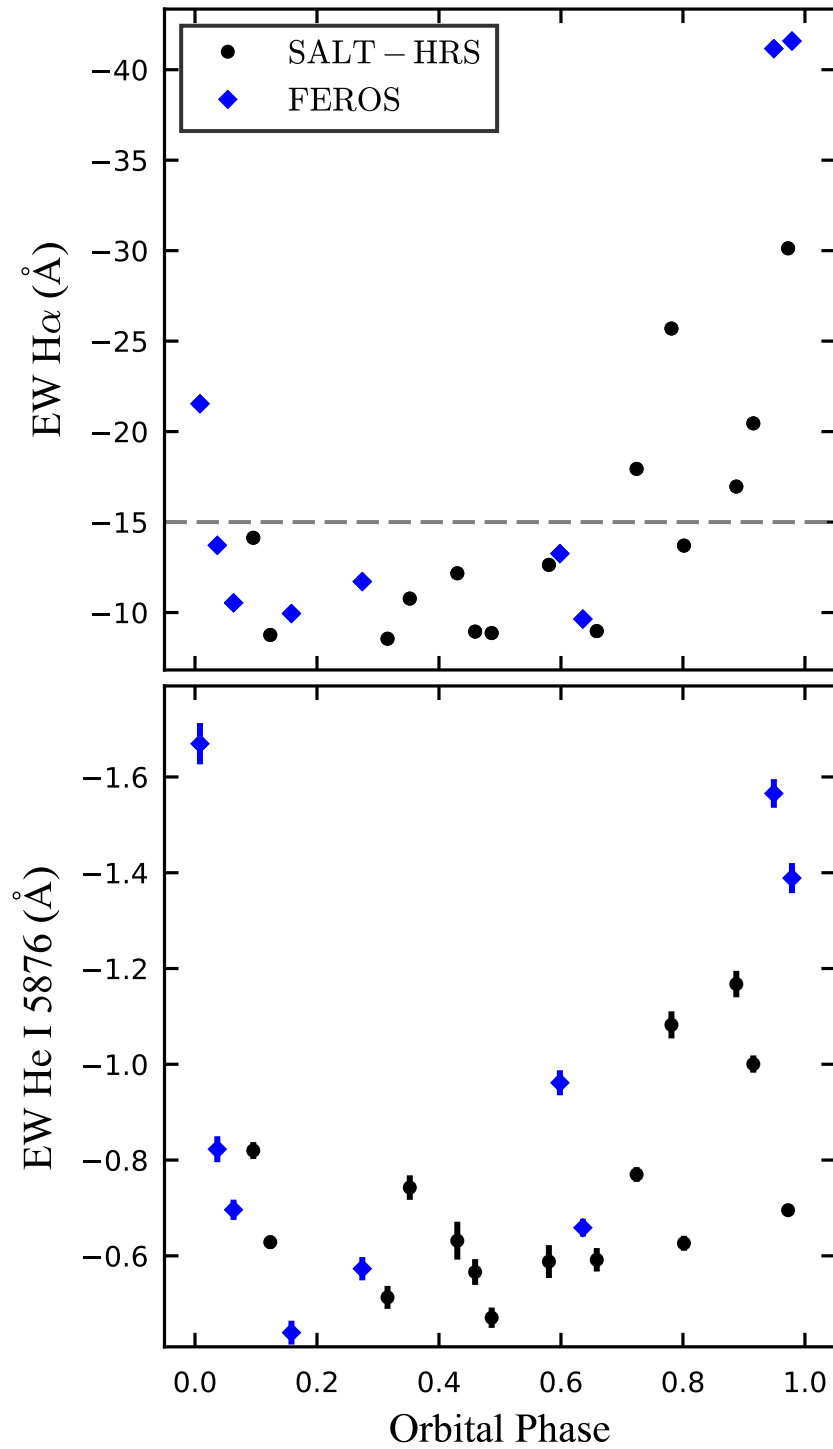


Figure 4.2 Equivalent widths of accretion-tracing emission lines as a function of orbital phase. Black circles are SALT-HRS observations; blue diamonds are FEROS observations.

analysis of the emission and velocity structure of accretion-tracing emission lines below. We explore the relative contribution of accretion and chromospheric emission mechanisms in Section 4.5.1.

Here we find it pertinent to note the limitations of EW measurements for accretion studies. EWs are measured with respect to the observed continuum. While line fluxes increase with increasing accretion, so too does the optical continuum emission through both Balmer and Paschen continuum emission as well as black-body radiation. Continuum emission is observed photometrically and in absorption-line veiling. This competition between an increasing line and continuum flux makes changes in the EW less representative of actual changes in the line's flux.

Though not presented graphically, we also measure the EWs of [O I] 6300 Å and Li I 6707 Å. [O I] is typically assumed to probe diffuse outflowing material (Hartigan et al. 1995) and Li I, in addition to being a tracer of youth, is a prominent absorption feature that can be used to measure the contribution of TWA 3B. These lines are discussed in Sections 4.4.2.4 and 4.4.2.5 below where their velocity profiles are presented.

4.4.2 Spectral Line Velocity Structures

To examine the kinematic structure of accretion-, outflow-, and photospheric-tracing spectral lines, the following subsections present the radial-velocity profiles of select spectral features in the TWA 3A binary center-of-mass rest frame. Figures 4.3 through 4.10 present continuum normalized spectral lines in the following format: spectra are ordered from bottom to top by increasing orbital phase, which is presented to the left or right of each curve. The line color and parenthetical in each label displays the orbital cycle in which the observation was made. For each spectrum the primary and secondary stellar radial velocities are presented as vertical blue and red lines, respectively. Continuum

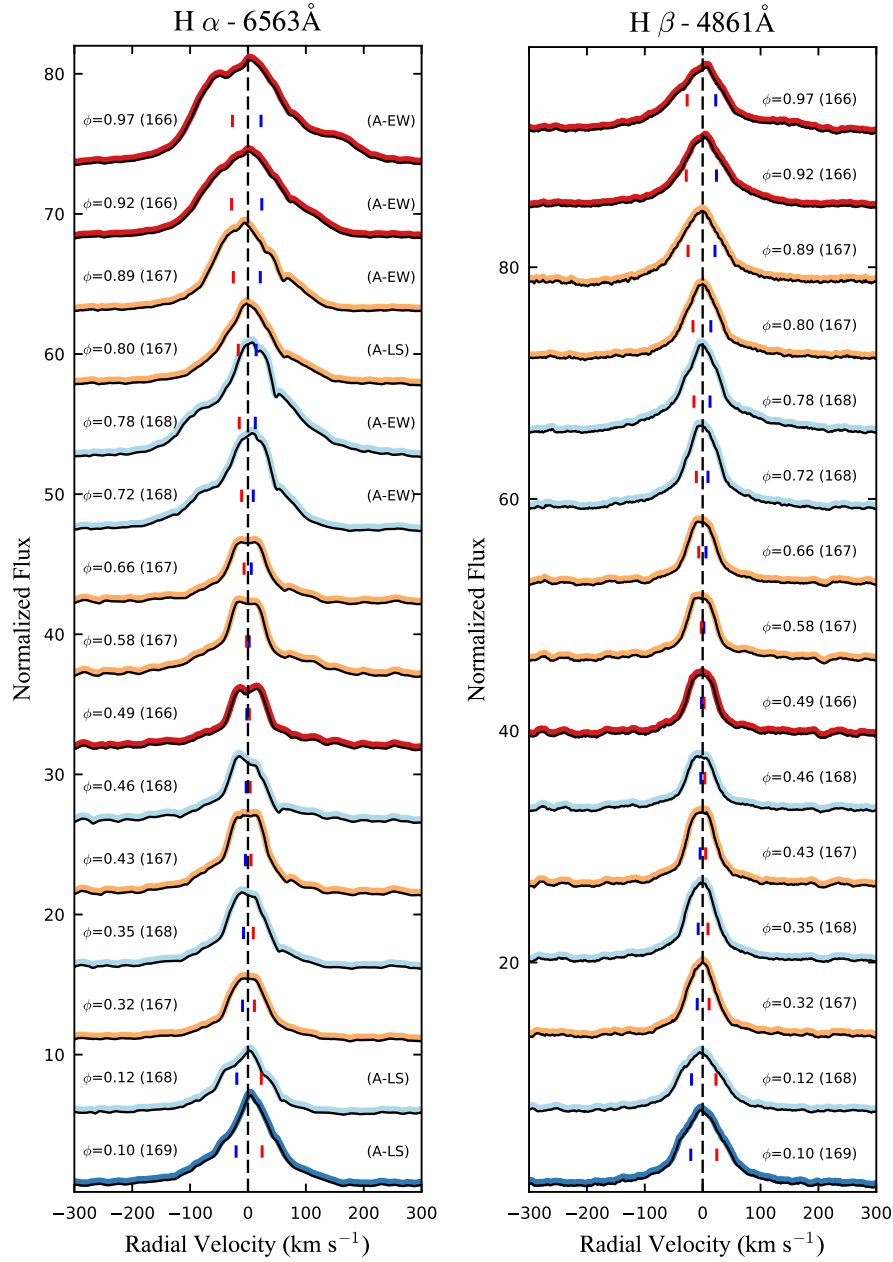


Figure 4.3 Velocity structure of continuum normalized Balmer emission lines $H\alpha$ and $H\beta$ from SALT-HRS observations. Velocities are presented with respect to the TWA 3A center-of-mass velocity (also marked with a dashed line). Spectra are ordered from bottom to top by increasing orbital phase, which is labeled adjacent to each spectrum. The line color marks the orbital cycle of the observation, which is listed in the label parentetical. Vertical dashes associated with each spectrum mark the stellar velocities of the primary and secondary in blue and red, respectively. The “(A-EW)” and “(A-LS)” labels mark the presence of active accretion based on the $H\alpha$ equivalent width and line structure, respectively (see Section 4.5.1).

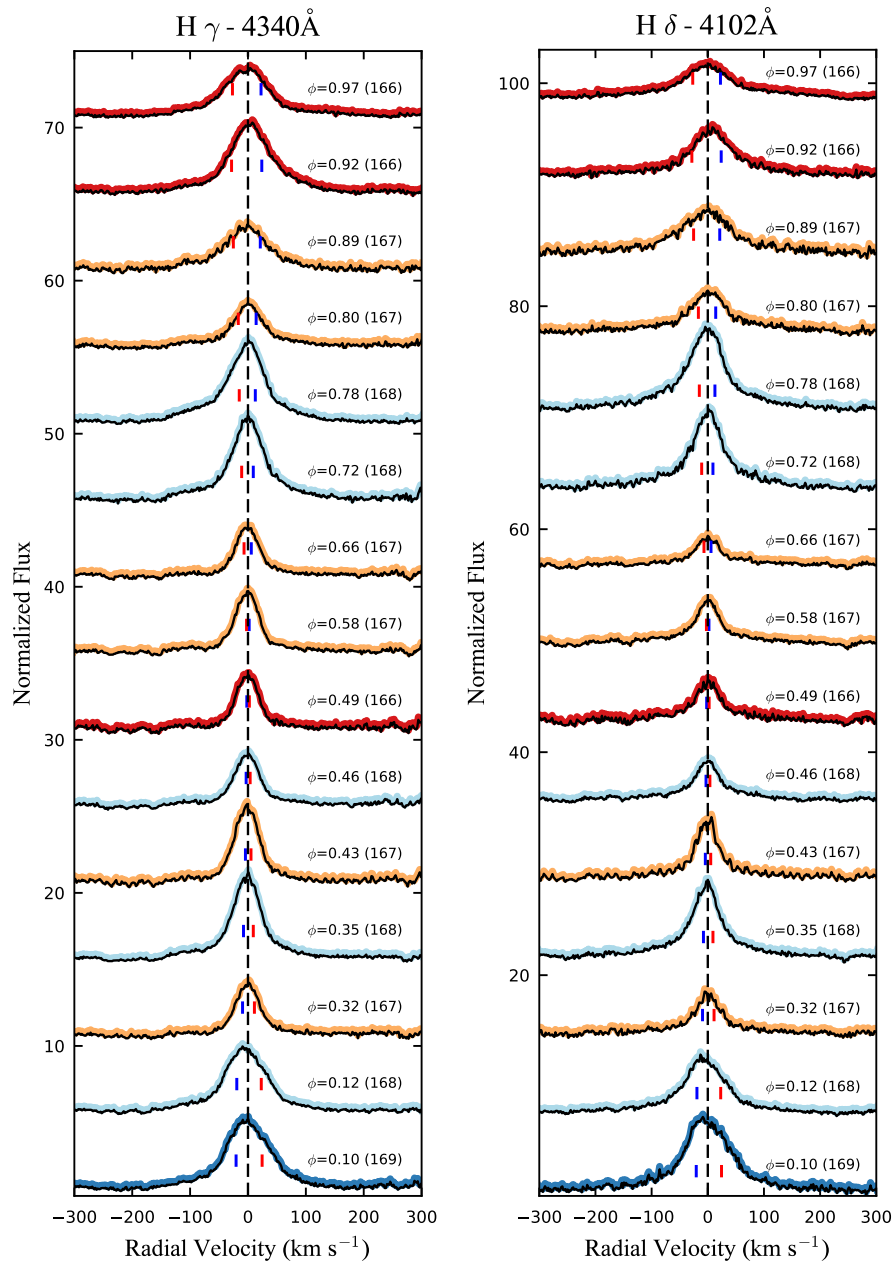


Figure 4.4 Velocity structure of normalized Balmer emission lines H γ and H δ from SALT-HRS observations. The stellar continuum is not consistently detected at these wavelengths; normalization is with respect to the sky/detection background. Only lines shapes are comparable between these spectra. (See Figure 4.3 for a full description of figure details.)

normalization has been performed locally for each line. In some figures (4.3, 4.6, 4.10) we include a note opposite the phase label signifying where we have determined the presence

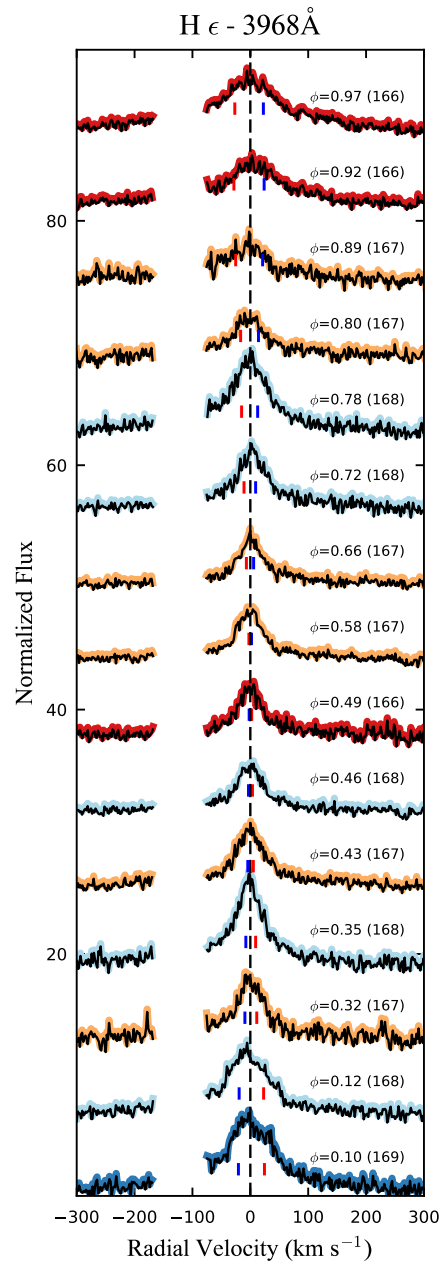


Figure 4.5 Velocity structure of Balmer emission line $H \epsilon$ from SALT-HRS observations. Gap at negative velocities is made to exclude $\text{Ca II H } 3986\text{\AA}$. The stellar continuum is not consistently detected at these wavelengths; normalization is with respect to the sky/detection background. Only lines shapes are comparable between these spectra. (See Figure 4.3 for a full description of figure details.)

of accretion based on the $H \alpha$ EW (“A-EW”), or the $H \alpha$ line structure (“A-LS”) compared to chromospheric emission. A full description of this determination is provided in Section

4.5.1.

For reference, the radial velocity of TWA 3B with respect to the TWA 3A center-of-mass is $\sim -1 \text{ km s}^{-1}$ (Kellogg et al. 2017).

4.4.2.1 H Balmer Series

Figures 4.3 through 4.5 presents the velocity structure of H α , β , γ , δ , and ϵ . Inspection of the H α and H β panels reveals strong increases in their emission strengths near periastron, mirroring the EW behavior in Figure 4.2 above. The velocity width and amount of line structure also increases near periastron, typical of accretion variability. Near apastron (spectra in the middle of the figure) emission is relatively narrow and stable, and is likely chromospheric in origin (see Houdebine et al. 2012). We discuss the relative contributions of accretion and chromospheric emission in Section 4.5.1 below.

Figures 4.4 and 4.5 present H δ , γ , and ϵ . Here we find narrow emission near apastron that becomes broader near periastron (top and bottom). Emission is mostly centered and symmetric with exceptions at $\phi=0.10$, 0.12, and 0.92 where there are asymmetries that skew toward the primary stellar velocity. We note that low levels of the stellar continua at these wavelengths result in line emission above our sky/background detection limit. The spectra in these panels are normalized to this background level. This makes the relative amplitude of lines dependent on the conditions of individual observations (e.g. atmospheric transparency) rather than their intrinsic strength with respect to a continuum.

4.4.2.2 He I 5876 Å & 4471 Å

In Figure 4.6 we present the velocity structure of the He I lines 5876 Å and 4471 Å. These lines are unique among most accretion tracing emission lines in that they have relatively narrow profiles, suffering less from self-absorption and optical depth effects than

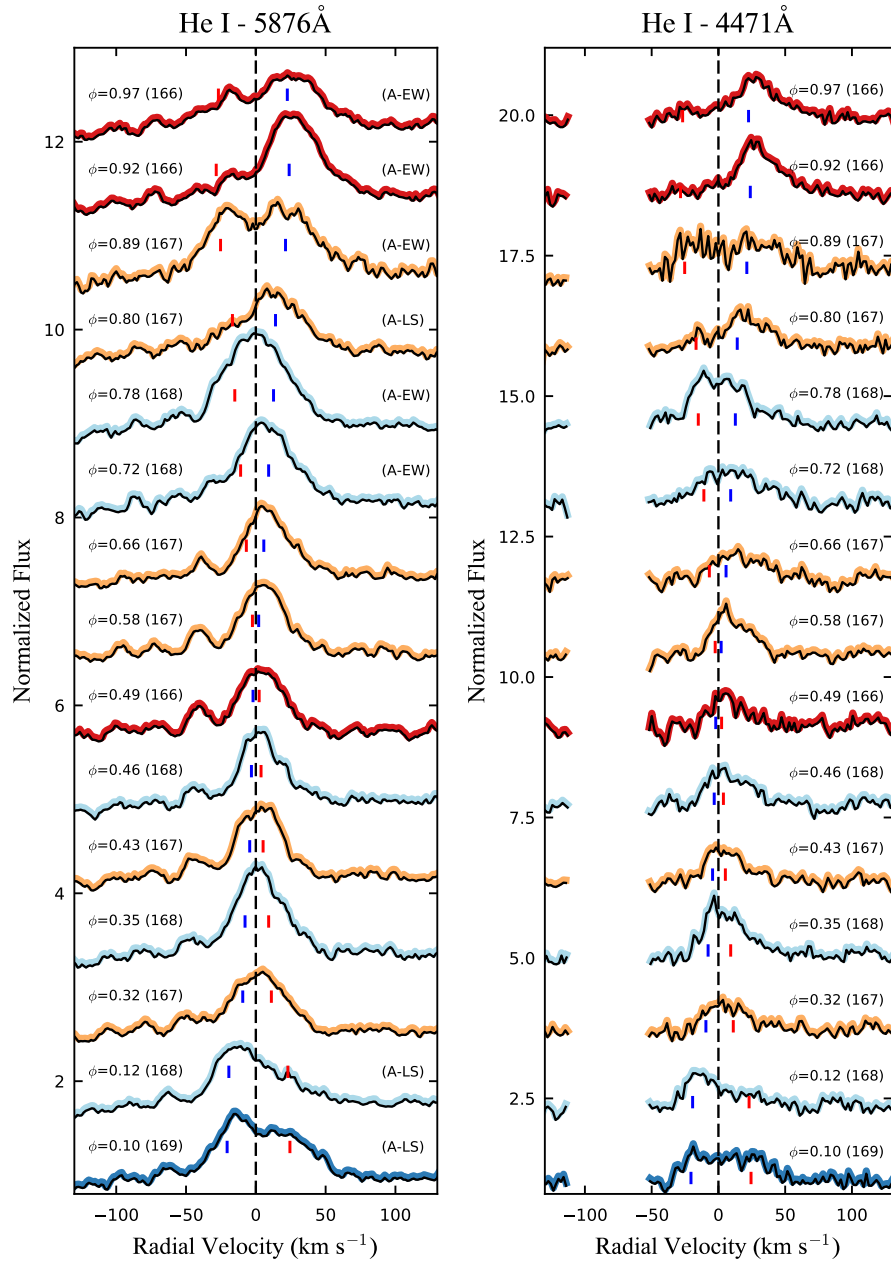


Figure 4.6 Velocity structure of He I emission lines 5876 Å and 4471 Å from SALT-HRS observations. Gap at negative velocities in the right panel corresponds to a chip defect. The “(A-EW)” and “(A-LS)” labels mark the presence of active accretion based on the H α equivalent width and line structure, respectively (see Section 4.5.1). (Same layout as Figure 4.3, see full description there.)

the H Balmer series (Muzerolle et al. 1998; Dahm 2008; Alencar et al. 2012). In these spectra we find similar trends to those seen in H α where emission strength, velocity width,

and velocity structure increase near periastron passage. Strikingly, in many of the highest EW observations the dominant component of emission is centered on the primary's stellar velocity. The observation at $\phi=0.92$ is the most dramatic example, but this behavior is present at some level in all of the high-EW epochs. In Sections 4.5.2 we discuss the prospect of using this line to determine the relative accretion rate onto each star.

4.4.2.3 Ca II H & K

In Ca II H and K (Figure 4.7), we find a similar behavior to He I 5876 Å where emission from the primary and secondary star appears to be resolved. With a narrow line width, multiple observations show double peaked profile ($\phi=0.10, 0.12, 0.78, 0.89$). While these lines likely have a chromospheric component to their emission (e.g. Houdebine 2012), the line widths and relative amplitudes between the primary and secondary are variable, for example, when comparing the $\phi=0.12$ and 0.78 epochs. At these wavelengths the lack of a consistent photospheric continuum prevent the measurement of EWs and comparison of emission strengths for each star across observations. Still, their variability in line widths and relative line strengths reveal orbital phase dependent behavior that is different for the primary and secondary.

4.4.2.4 [O I] 6300 Å

Forbidden O emission is an important tracer of low-density gas in the outflows of young star-disk systems. In high accretion rate systems [O I] emission can be broken into a high-velocity component which is spatially extended and a low-velocity component whose emission is unresolved near the central star (Hartigan et al. 1995; Hirth et al. 1997). It is thought that the high velocity component traces accretion-powered jet or micro-jet processes (Ray et al. 2007), while the low-velocity component traces a photoevaporative

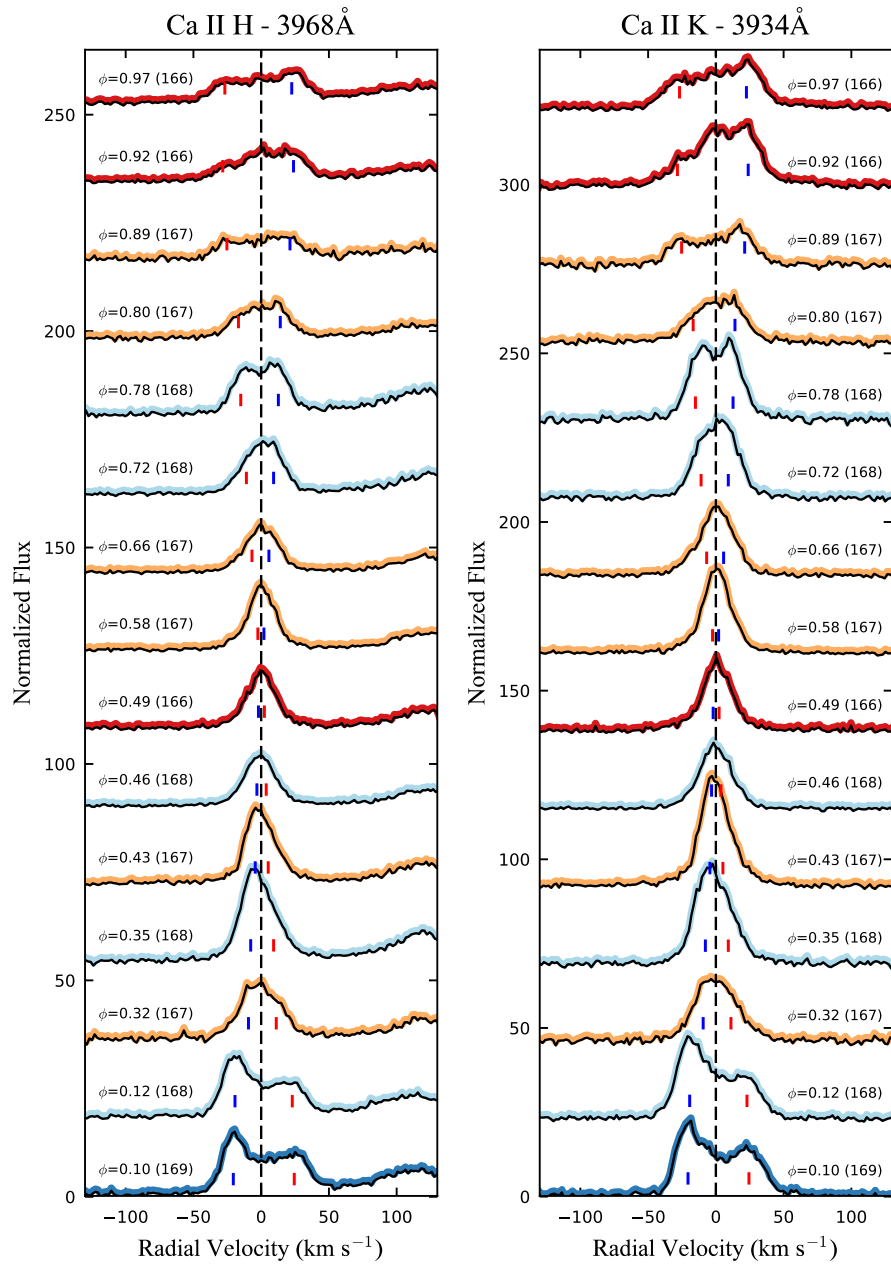


Figure 4.7 Velocity structure of Ca II H and K emission lines from SALT-HRS observations. Rising flux values at positive velocities in the left panel is the contribution of H ϵ . The stellar continuum is not consistently detected at these wavelengths; normalization is with respect to the sky/detection background. Only lines shapes are comparable between these spectra. (Same layout as Figure 4.3, see full description there.)

(Ercolano & Owen 2010, 2016) or magneto-centrifugal disk wind (Bai et al. 2016).

In Figure 4.8 we present the velocity profiles of [O I] 6300 Å in the same format as

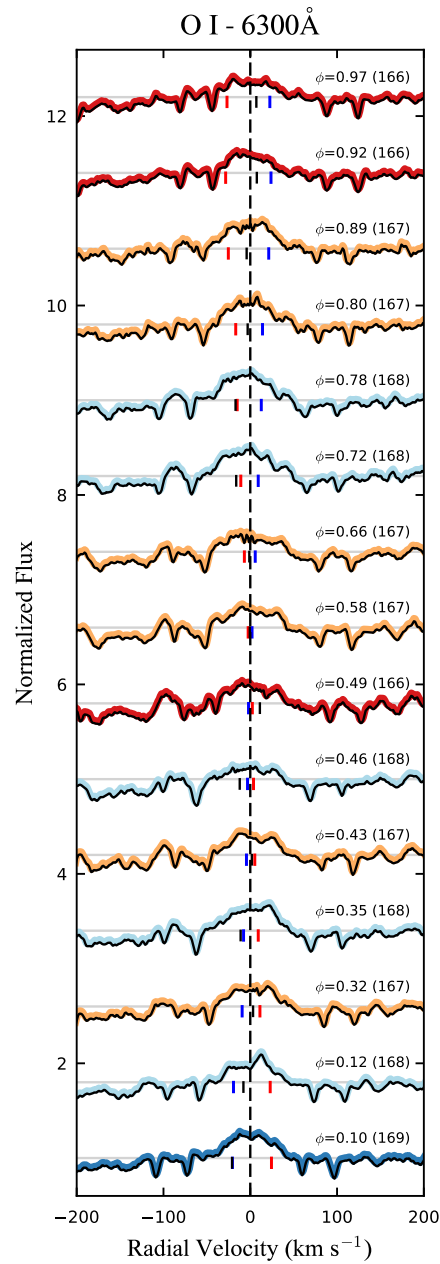


Figure 4.8 Velocity structure of [O I] 6300 Å from SALT-HRS observations. The additional black vertical line associated with each spectrum is the velocity of the terrestrial [O I] sky line in the binaries center-of-mass rest frame. At these velocities some artifacts of sky subtraction remain. Horizontal gray lines mark the continuum level. (Same layout as Figure 4.3, see full description there.)

previous figures, but with the addition of a black vertical line for each spectrum marking the location of the terrestrial sky line that has been removed. We find stable emission

from a low-velocity, broad component that is invariant with changes in the stellar velocities and the mass accretion rate. Small changes in EW are likely due in an increase in the continuum level during enhanced accretion.

This behavior is in general agreement with Simon et al. (2016), who find this broad, low-velocity component is stable over decade timescales and most likely originates at the base of a MHD disk wind being launched from $\sim 0.05\text{--}0.5$ AU scales (although a photoevaporative process is not strictly ruled out). The fact that TWA 3A has likely carved out the central portion of its circumbinary disk at $0.3\text{--}0.5$ AU scales may indicate that the emission region has a larger spatial extent, or that the presence of stable disk material is not a necessity for this emission origin. This stellar velocity and accretion rate invariance is also observed in the short-period, T Tauri binaries DQ Tau and UZ Tau E (Huerta et al. 2005).

4.4.2.5 Li I

The velocity profiles of Li I are presented in Figure 4.9 where clear splitting in the spectral line can be seen that follows the stellar velocities. At near-periastron epochs, a component from the tertiary is visible just blueward of zero velocity, most notably in the top spectrum, $\phi=0.97$. We find that the EW of this line varies at about the 1.5σ level, which is likely due to continuum veiling and small changes in the contribution of TWA 3B due to seeing and pointing variations. The relatively low accretion rate in this system, with the potential for zero accretion outside of discrete bursts, also gives rise to small levels of veiling at this wavelength. This can also be seen in the low variability of the *V*-band light curve (probing the same continuum region) in Tofflemire et al. (2017b, Figure 1).

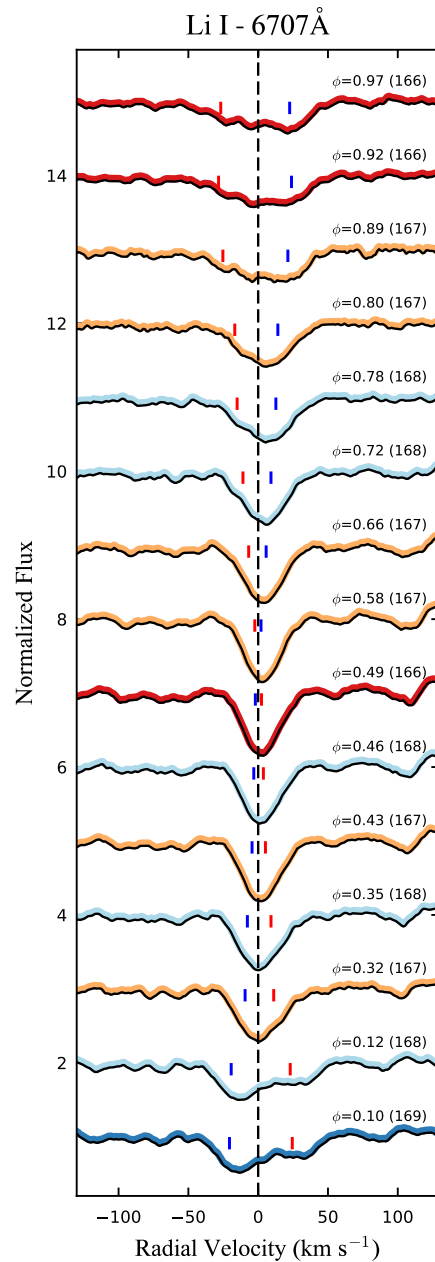


Figure 4.9 Velocity structure of Li I 6707 Å from SALT-HRS observations. (Same layout as Figure 4.3, see full description there.)

4.4.2.6 Other Spectral Features of Note

Two sets of lines, the Ca II Infrared triplet and Na I D doublet, also displayed orbital-phase dependent variability. We do not supply plots of these lines for brevity but note that they display variable emission cores, specifically Ca II 8662 Å and Na I 5890 Å, that vary

in strength and also follow the primary’s radial velocity.

4.4.2.7 Archival FEROS Observations: H α & He I 5876 Å

Drawn from ~ 15 orbital periods that predate our SALT–HRS observations by ~ 150 orbital cycles, the FEROS spectra allow us to comment on the longevity of observed trends while increasing the phase coverage and number of periastron accretion outbursts observed. We focus on two lines from this dataset, H α and He I 5876 Å, which are plotted in Figure 4.10. In this figure and in Figure 4.2 we find the same trends from the 2015 epochs still hold where the EW, velocity width, and velocity structure increase near periastron passage. He I emission also continues to preferentially trace the primary’s stellar velocity.

4.5 Discussion

In the following subsections we discuss the velocity structure of accretion-tracing emission features as a means to inform our understanding of accretion flows in the TWA 3A system. A significant piece of this interpretation relies on determining the intrinsic chromospheric emission of these lines in order to determine when and where accretion is taking place. We then present evidence for preferential accretion onto the TWA 3A primary, and comment on the implication of this result for the binary-disk interaction.

4.5.1 Accretion and Chromospheric Emission

Chromospheric line emission is a staple of magnetically active stars. WTTSs in particular have high levels of chromospheric emission due to their high magnetic field strengths (Johns-Krull 2007). Chromospheric emission can produce either emission cores or complete emission in many lines that are also used to trace stellar accretion (e.g. H α , H β , Na I D, Ca II H and K, He I 5876 Å).

There are three empirical characteristics of chromospheric emission that distinguish it

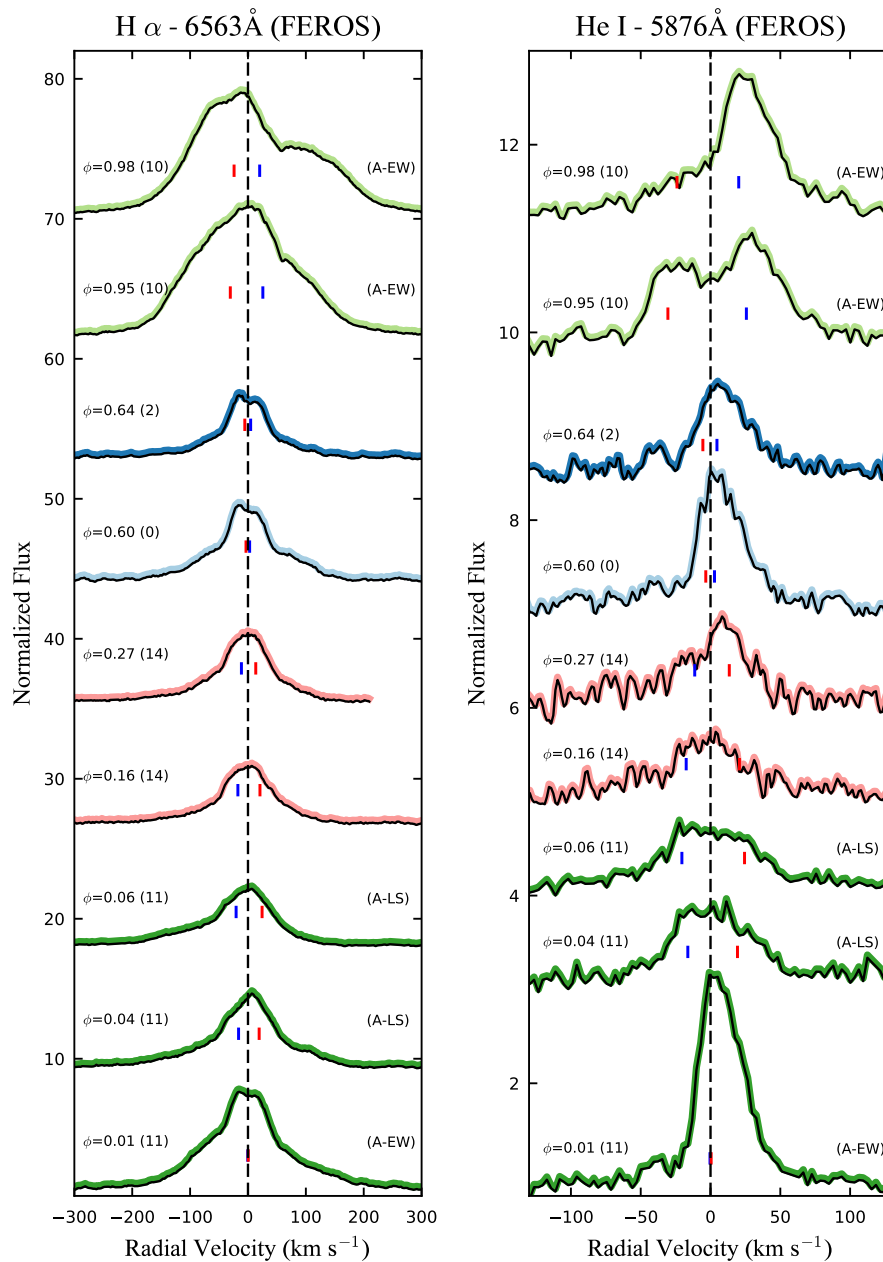


Figure 4.10 Velocity structure of $H\alpha$ and $He\ I\ 5876\ \text{\AA}$ from archival FEROS observations. For the bottom spectrum, near periastron, the stellar velocities are overlapping. The “(A-EW)” and “(A-LS)” labels mark the presence of active accretion based on the $H\alpha$ equivalent width and line structure, respectively (see Section 4.5.1). (Same layout as Figure 4.3, see full description there.)

from accretion emission. We use these, focusing on $H\alpha$, to temporally isolate the presence of accretion in our TWA 3A spectra.

The first is stability. While chromospheric emission has some level of variability, in the absence of stellar flares (Schmidt et al. 2012; Kowalski et al. 2013), typical EW variability is on the $\lesssim 20\%$ level (Flores Soriano et al. 2015). Accretion processes, however, are exemplified by their variability in emission strength, line width, and line shape (e.g. Dupree et al. 2012; Sousa et al. 2016).

In Figure 4.11 we present the EWs of He I 5876 Å as a function of the H α EW. In the bottom left corner, a cloud of measurements fall below the H α chromospheric EW cutoff for M3–M4 stars, -15 Å, marked with the vertical dashed line (Fang et al. 2009). These points have a small spread consistent with chromospheric variability. Based on their variability and location in this figure we confirm that the -15 Å EW value for H α is a good, first-order indicator of the presence of accretion in TWA 3A.

A similar behavior is also seen in Figure 4.12 where the EWs of H α and He I 5876 Å are presented as a function of the photometrically derived mass accretion rates. The \dot{M} values represent a linear interpolation of adjacent photometric measurements (see Figure 4.1) that introduce some additional scatter to this plot. (\dot{M} measurements are updated from Tofflemire et al. (2017b) accounting for the *Gaia* distance and the update stellar parameters discussed in Section 4.2.)

For the remainder of our discussion we assume observations with H α EW ≤ -15 Å include active accretion. These epochs are signified with an “A-EW” opposite to their label in the H α panel of Figure 4.3, the He I 5876 Å panel of Figure 4.6, and Figure 4.10.

The line width and structure are the remaining characteristics we consider. Chromospheric emission is typically narrow, with line widths comparable to $v \sin i$ rotational velocities (FWHM ~ 10 – 50 km s $^{-1}$; Houdebine et al. 2012; Houdebine 2012). The shape of this emission is symmetric about the systemic velocity with a dominant narrow component (López-Santiago et al. 2003). In deep photospheric absorption lines (H α ; Ca II H and K),

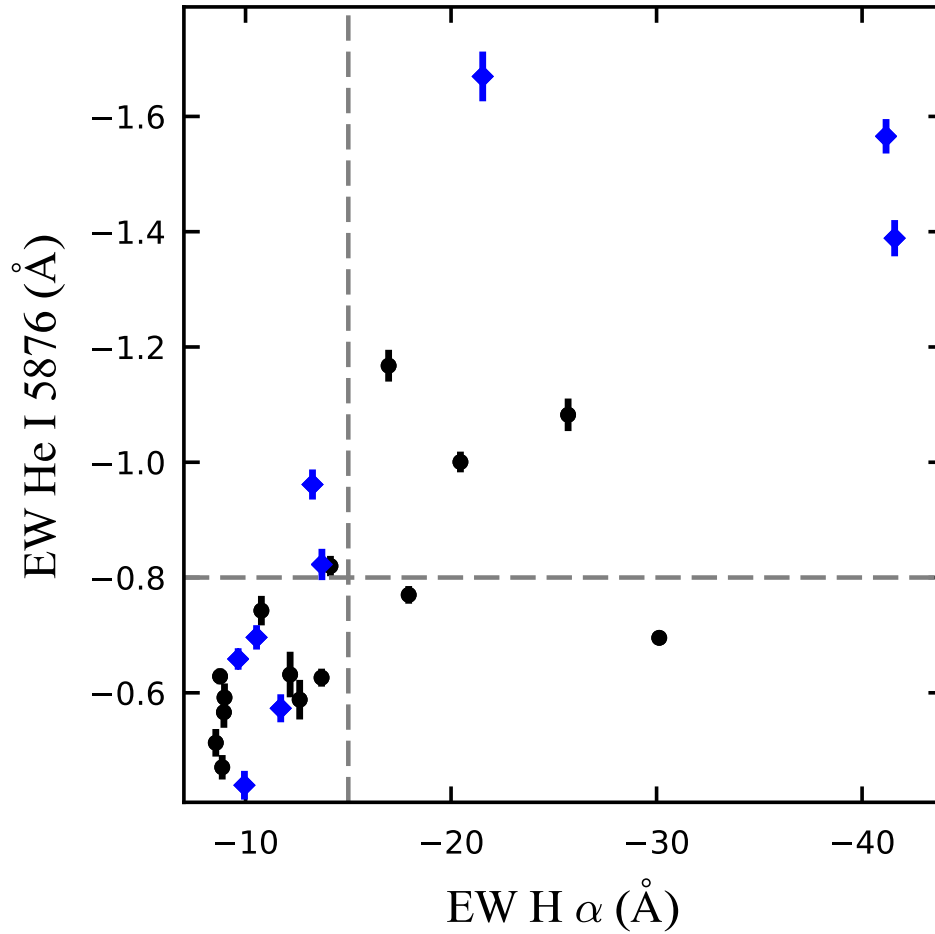


Figure 4.11 Equivalent width of He I 5876 Å as a function of the H α equivalent width. Black circles are SALT-HRS observations; blue diamonds are FEROS observations. The vertical gray line marks the H α EW boundary between chromospheric- and accretion-based emission (Fang et al. 2009). The horizontal gray line is a similar cutoff we propose for He I 5876 Å EWs. Observations in the bottom left are likely chromospheric while those in the rest of the figure indicate the presence of active accretion.

the combined emission results in a double peaked profile due to self absorption.

Conversely, accretion shock dominated line emission, especially in a high optical depth lines like H α , can reach widths of hundreds of km s^{-1} . White & Basri (2003), for instance, propose an accretion-chromospheric boundary for H α at full-width of 10%-maximum values of $\sim 270 \text{ km s}^{-1}$.

Inspecting the H α panel of Figure 4.3, we find the group of low-EW measurement (ϕ

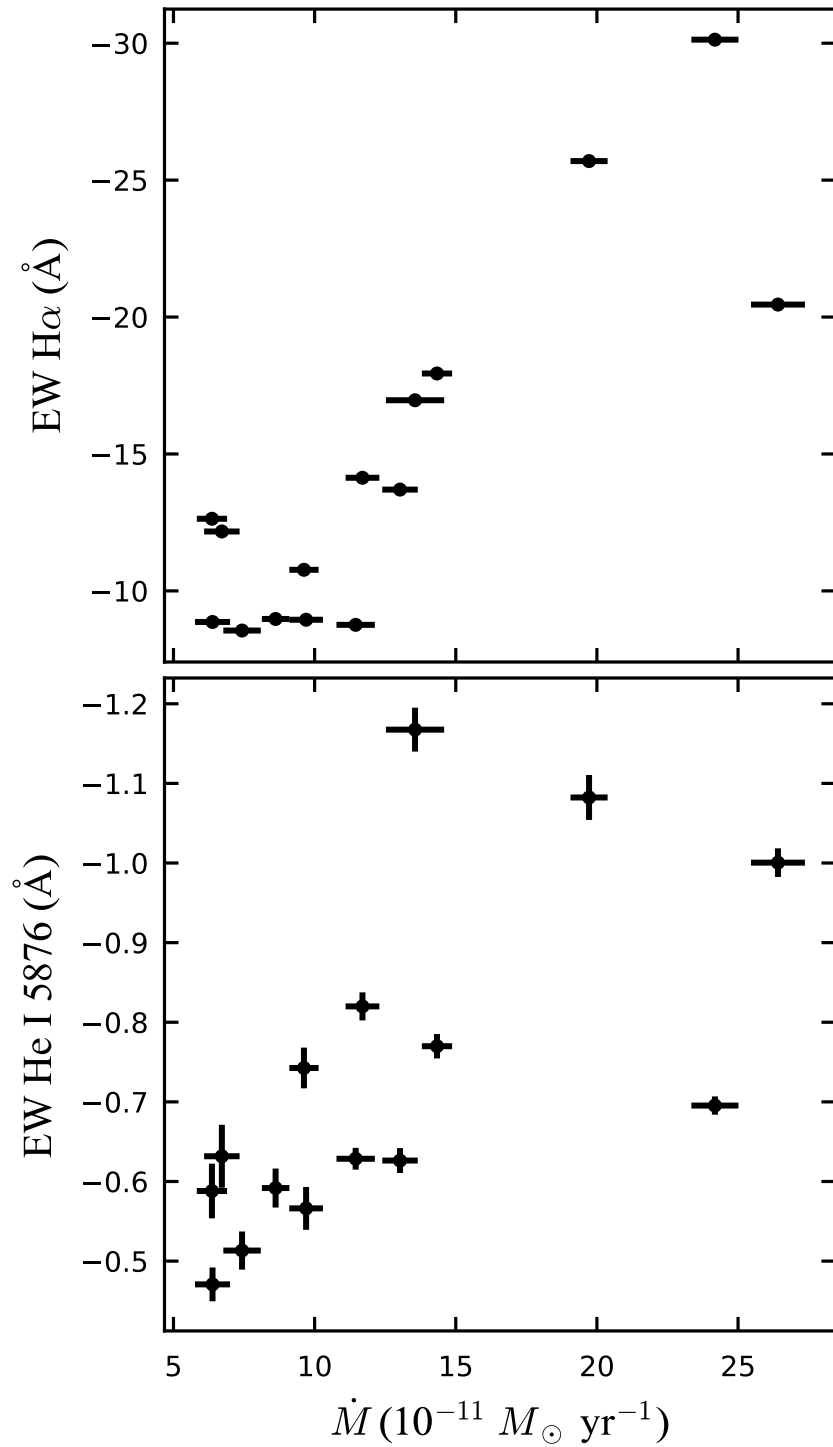


Figure 4.12 Equivalent widths of accretion-tracing emission lines as a function of the photometrically determined mass accretion rate. Mass accretion rate for each equivalent width measurement is the linear interpolation of the adjacent photometric observations.

= 0.32–0.66) all have line structures matching chromospheric emission (Houdebine 2009; Houdebine et al. 2012), just as the EW cutoff above would suggest. There are a few epochs however that have low EW but do not possess the same line structure. They are $\phi = 0.10$, 0.12, and 0.80 in Figure 4.3 and $\phi = 0.04$ and 0.06 in Figure 4.10. Due to the limitations in EW measurement in the absence of a continuum correction (see Section 4.4.1), we conclude that these observations also contain active accretion despite their low EW values. These are signified with an “A-LS” opposite their phase label in the H α panel of Figure 4.3, the He I 5876 Å panel of Figure 4.6, and in Figure 4.10.

For each of the three characteristics listed above, the chromospheric components of He I 5876 Å are less well characterized than H α or Ca II H and K due to its weaker emission. In many main-sequence dwarfs He I 5876 Å is in absorption for instance (Houdebine et al. 2009). The seemingly on-off nature of accretion in TWA 3A supplies a unique opportunity to diagnose the He I chromospheric contribution. Following the discussions above we propose a similar H α -like EW boundary for chromospheric and accretion dominated emission for He I 5876 Å EWs at -0.8 Å, which is presented as the horizontal dashed line in Figure 4.11.

This interpretation of minimal or absent accretion outside of periastron is consistent with the K2 observations of DQ Tau. This light curve show clear star-spot modulation in between periastron accretion events. (These data have yet to appear in the literature but are publicly available and presented for reference in Appendix C.1.) Even with its red-optical centered passband where continuum enhancements from accretion are small, *Kepler*’s precision should detect variable accretion at low levels. This interpretation implies some tension with the results of Tofflemire et al. (2017a,b, DQ Tau and TWA 3A) and Basri et al. (1997, DQ Tau), which find some level of accretion at all times in T Tauri binaries via photometry and spectroscopy, respectively. For the photometric measurements,

systematic errors in the derived zero-point allow for flux measurements near apastron that are consistent with the determined photospheric and chromospheric background flux level. In the case of spectroscopy, the spectral template used to derive DQ Tau’s constant veiling was a main sequence K6 star, Gl 380. (For reference, DQ Tau’s spectral type is likely M0; Herczeg & Hillenbrand 2014). White & Basri (2003) later showed that main-sequence and giant spectral templates result in erroneously high veiling measurements when compared to an empirical WTTS spectral template. It is likely that a more representative template would eliminate the constant, low level of veiling observed outside of periastron.

4.5.2 Preferential Accretion onto the TWA 3A Primary

Within the subset of our observations that show evidence for active accretion, we use the velocity structure of He I 5876 Å as a probe of the relative mass accretion rate onto each star. This line has the advantage over most accretion-tracing emission lines in that it has a narrow width, allowing us to decompose the emission from both stars.

Moving from He I 5876 Å emission to a quantitative measure of relative mass accretion rate between the primary and secondary requires correcting for changes in the observed continuum level due to accretion. From there, a model from the chromospheric emission from each star can be removed. An analysis of this kind is beyond the scope of the current work. Still, the observed relative flux at each star’s radial velocity can provide a qualitative assessment of the accretion onto the components of TWA 3A.

Figure 4.13 demonstrates the capability of this line to detect accretion onto individual stellar components. Here we compare a high-accretion, periastron epoch in black ($\phi = 0.92$) with a low-, or zero-accretion, apastron epoch in gray ($\phi = 0.46$). In the case of the apastron epoch, the stellar velocities are nearly overlapping. We assume the same chromospheric contribution from each star and overplot the line at half strength for each

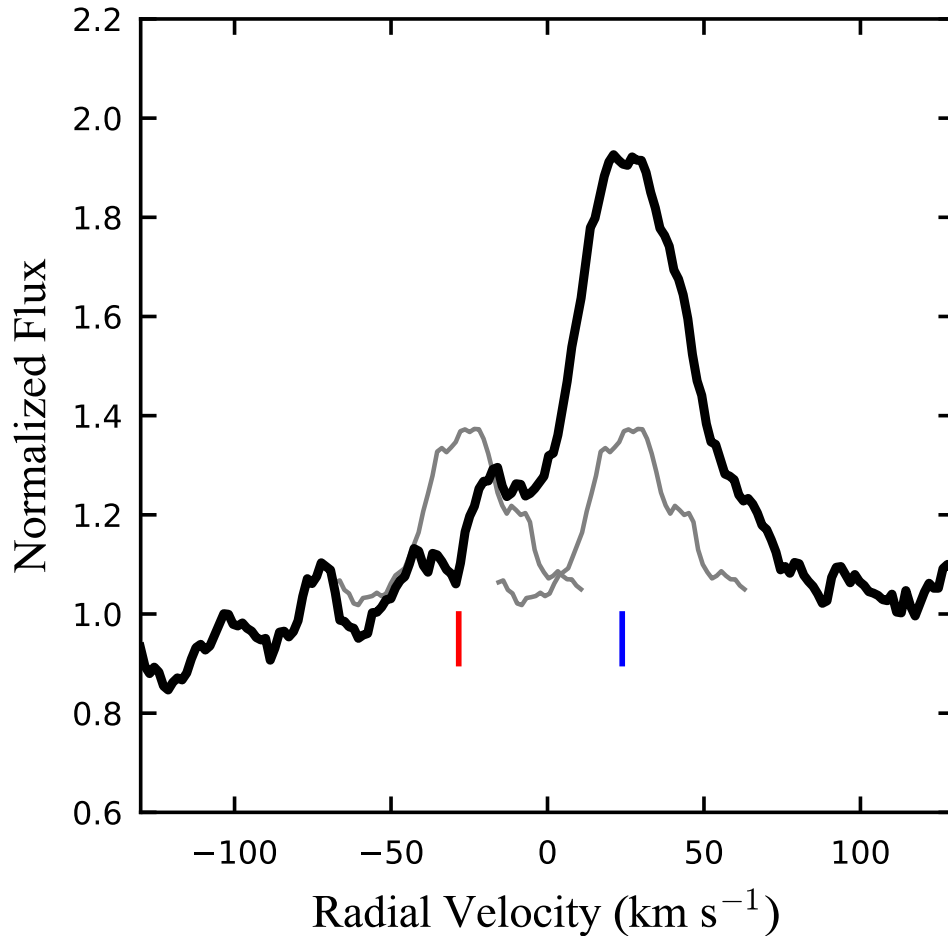


Figure 4.13 Velocity structure of a high EW epoch of He I 5876Å ($\phi=0.92$) in black, with the narrowest He I 5876 Å line profile ($\phi=0.46$) over-plotted in gray for each stellar velocity at $\phi=0.92$. The low EW observations has been divide by two assuming an equal contribution between both stars. The high EW observation has been scaled by the most adjacent relative V -band flux between the two epochs. Blue and red dashes mark the radial velocities of the primary and secondary, respectively, at an orbital phase of $\phi = 0.92$.

star's radial velocity at a corresponding orbital phase of $\phi = 0.92$. The velocity of the primary and secondary are presented as the blue and red lines, respectively. The black curve has been scaled by the relative V -band flux between these two observations based on a linear interpolation of the Tofflemire et al. (2017b) photometry. While this continuum correction is crude, this figure highlights its necessity for a quantitative analysis.

The large increase in emission strength that is centered on the primary's velocity

(blue) is compelling evidence for a burst of accretion that preferentially feeds the primary star. While Figure 4.13 only compares one high-accretion-rate epoch, this line consistently has the dominant component of its emission centered at the velocity of the primary star, which can be seen in Figures 4.6 and 4.10. An alternative view of the actively accreting epochs is provided in a Doppler tomographic representation in Figure 4.14.

While there do exist epochs where there is a clear contribution from both stars ($\phi=0.89, 0.10$ in Figure 4.6; $\phi=0.95$ in Figure 4.10), there are no observations that show dominant emission at the secondary’s velocity. Our interpretation of this line structure is that accretion from the circumbinary disk preferentially feeds the TWA 3A primary star.

We note that due to the difference in stellar properties between the primary and secondary, an equal mass accretion rate onto each star would not correspond to an equal accretion luminosity. Since the He I 5876 Å luminosity has been shown to be tightly correlated with the accretion luminosity (Dahm 2008; Herczeg & Hillenbrand 2008; Fang et al. 2009), we use the following equation to compare the relative emission from the components of TWA 3A:

$$\dot{M} \simeq \frac{L_{\text{Acc}} R_{\star}}{GM_{\star}} \left(1 - \frac{R_{\star}}{R_{\text{in}}}\right)^{-1}. \quad (4.1)$$

Assuming the parameters listed in Section 4.2, an equal mass accretion rate onto each star would correspond to $\sim 10\%$ more emission from the primary star due its higher mass. With this in mind, He I 5876 Å observations like $\phi=0.89$ (Figure 4.6) and 0.95 (Figure 4.10) may have relative accretion rates near unity despite their difference in relative flux for each component.

4.5.2.1 Implication for the Accretion Stream Theory

Our conclusion that the TWA 3A primary is the main recipient of infalling circumbinary material places a strong observational constraint on the binary accretion stream theory.

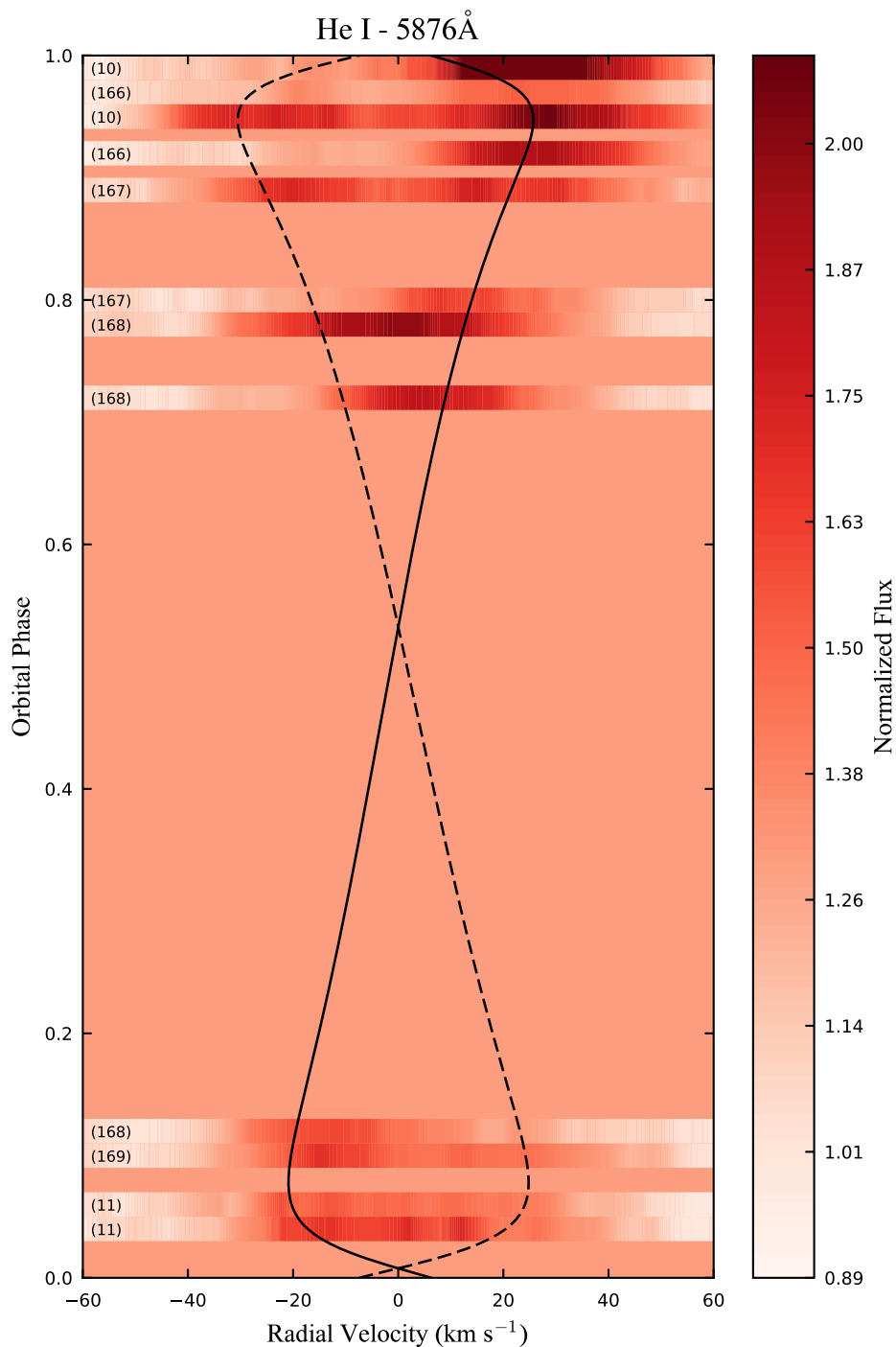


Figure 4.14 Doppler tomography of He I 5876 Å from SALT-HRS and FEROS observations with active accretion (see Section 4.5.1). Each spectrum is presented as a horizontal band where the color encodes the normalized flux. The orbital cycle of each observation is presented on the left of the band. Solid and dashed curves represent the primary and secondary stellar velocities, respectively.

As far as we are aware, this is the first observation of the relative accretion rate for the components of a spectroscopic binary and is the first measurement of relative accretion rates in a binary spanning multiple dynamical timescales. We note that individual accretion rates have been measured for spatially resolved binaries with separations less than the typical protoplanetary disk size ($a = 14\text{--}140$ AU; Hartigan & Kenyon 2003). It is uncertain the degree to which accretion in these wider binaries, especially at the largest separations ($a > 100$ AU), is analogous to a system like TWA 3A, but it is intriguing that higher accretion rates are more often found for the primary star in these systems.

This result becomes more significant in the light of a large body of theoretical work that consistently predicts the secondary should be the dominant recipient of circumbinary accretion flows (Hayasaki et al. 2007, 2013; Cuadra et al. 2009; Roedig et al. 2011; Farris et al. 2014; Young et al. 2015; Young & Clarke 2015). These works have focused mainly on black-hole binary systems but should, in principle, describe the same physical processes. The physical interpretation of these results is that inner circumbinary disk material will have specific angular momenta that are closer to that of the secondary than the primary, requiring less angular momentum loss in order to be accreted. Framed in another way, the secondary is always closer to the circumbinary disk allowing it to more easily collect incoming accretion streams.

It is worth noting that efforts to simulate specific T Tauri binaries have found preferential accretion onto one component of an equal mass system (DQ Tau; de Val-Borro et al. 2011), and preferential accretion onto the primary (rather than secondary) component under certain orbital parameters (GG Tau; Günther & Kley 2002). These specific results should be interpreted with caution, however, as they only simulate a small number of binary orbital periods. It is not clear that these simulations have reached a steady state, especially in the inner disk which requires many hundreds of binary orbital

periods to relax from the initial conditions. As a result, these studies may be depicting behavior that is transient in nature. In truth, many of the theoretical works above simulate at most a few hundred orbital periods and draw their conclusions from an average of \sim tens of binary orbits once the simulation is deemed to be in steady state. Due to the expensive nature of these simulations, secular variability cannot be probed.

The numerical study of binary accretion by Muñoz & Lai (2016) stands out amongst others by simulating > 2000 binary orbital periods and thereby reaching relaxation in the circumbinary disk out to $\sim 9a$. These authors also track accretion variability over many hundreds of binary orbital periods. In the case of an eccentric ($e=0.5$), equal-mass binary, they find that the dominant recipient of circumbinary accretion flows alternates between the two stars on timescales of hundreds of binary orbital periods. The driver of this behavior is the precession of an eccentric inner disk cavity. This eccentricity naturally arises from the binary's non-axisymmetric potential. (We note this has also been found by other works that either did not resolve binary accretion (Dunhill et al. 2015) or did not simulate long enough to observe the gap's precession (Farris et al. 2014)). As this eccentric gap experiences apsidal precession, its orientation brings one star's apastron passage closer to the circumbinary disk than the other, inducing a larger accretion stream and corresponding accretion burst compared to its companion. At any given time, one star may accrete 10-20 times more than its companion, but over many precession times, the integrated mass accreted by each component approaches unity.

If the precession of an inner circumbinary disk gap is indeed the source of our observed preferential accretion into the TWA 3A primary, we should expect this behavior to reverse on half of the gap-precession timescale. For a pressureless particle disk, the precession rate

around an eccentric binary is:

$$\dot{\omega}_d \simeq \frac{3\Omega}{4} \frac{q}{(1+q)^2} \left(1 + \frac{3}{2}e^2\right) \left(\frac{a}{a_d}\right)^{7/2}, \quad (4.2)$$

where Ω is angular frequency of the binary, and a_d is the inner edge of the circumbinary disk, typically assumed to be $3a$ (Muñoz & Lai 2016). Assuming the dominant accretor flips after 180° of precession, the alternating timescale then becomes $T_{\text{flip}} \simeq \pi/\dot{\omega}_d$. For TWA 3A’s orbital parameters this corresponds to ~ 80 orbits. With only two widely separated epochs observed, we have limited leverage to constrain the predicted accretion-flipping behavior. The consistent preference for accretion onto the primary at epochs roughly 150 orbital periods apart does not strictly conflict with this prediction. Follow-up observations will be required to make a stronger statement about the validity of this precessing-gap scenario.

While the prospect of confirming this scenario is intriguing, it should be noted that direct comparisons between the Muñoz & Lai (2016) models and TWA 3A are limited. The main difference arises from the presence of small circumstellar disks in the models, which are likely not present in TWA 3A due to the narrow periastron separation and the disruptive effect magnetic fields have on inner disk material (see Tofflemire et al. 2017a,b for further discussion). The extent to which the accretion behavior and specifically the accretion-flipping behavior depends on the presence of circumstellar disks is unclear.

Circumbinary accretion is often employed to explain the abundance of stellar “twins” (Raghavan et al. 2010, $q > 0.95$), assuming accretion dominated by the secondary equalizes the mass ratio. Given the discussion above, we hesitate to comment on the implications of our result on the evolution of the binary mass ratio. It also is unclear the degree to which the TWA 3A accretion behavior is representative of other T Tauri binaries or of proto-binary systems where, due to higher disk masses and mass accretion rates, the largest change in

the binary mass ratio is likely to take place. We advocate for continued examination of the above assumption and for future theoretical efforts to examine secular interaction between binaries and their disks.

4.6 Conclusions

In this work we have monitored the T Tauri binary TWA 3A with time-series, high-spectral-resolution optical spectroscopy and time-series optical photometry to trace variability in the amplitude and kinematics of accretion flows. The main results of our work are as follows:

1. Accretion diagnostics H α , H β , and He I 5876Å reveal bursts of accretion near TWA 3A periastron passages, confirming the orbital phase dependent accretion behavior observed photometrically in Tofflemire et al. (2017b).
2. The emission strength and line-shape of H α outside of periastron appears to be chromospheric, suggesting very low, or a complete lack of accretion outside of discrete periastron bursts.
3. Similar to the -15 \AA H α EW boundary separating weak-lined and classical T Tauri stars with M3–4 spectral types, we propose a cutoff for He I 5876 Å EWs at -0.8 \AA .
4. The velocity profiles of narrow, accretion-tracing emission lines consistently favor the primary stellar radial velocity in TWA 3A. We have focused our analysis most heavily on He I 5876 Å but note the same behavior is present in H γ , H δ , Ca II H and K, and in the emission cores of Na I D and the Ca II IR triplet.
5. We interpret the He I 5876 Å velocity structure as preferential mass accretion onto the primary star. This result conflicts with the vast majority of numerical simulations

of binary accretion. The simulations of Muñoz & Lai (2016), however, include a precessing, eccentric inner disk cavity that allows for the dominant accretor to alternate between the primary and secondary on timescales of hundreds of orbital periods. If this is the case, future observations should find He I 5876 Å emission to preferentially reside at the secondary’s radial velocity near periastron passage.

6. The emission of [O I] 6300 Å is not correlated with the accretion rate or the stellar velocities, favoring a disk wind scenario originating in the extended circumbinary disk.

4.7 Future Work

This chapter is a manuscript in development for submission to the *Astrophysical Journal*. Already, we have been able to make important conclusions regarding the kinematics of accretion streams near the TWA 3A binary. The following outline of future work presents other dimensions for exploration of this rich dataset.

- Characterizing the veiling continuum will allow for a direct comparison of flux values across epochs. This is required for much of our future analysis. Veiling will be measured by fitting an empirical, M4 WTTS spectrum with an additive continuum to regions of our spectra with rich stellar absorption features. Manara et al. (2017) provide an extensive library of such spectra.
- Develop a model for the chromospheric emission of He I 5876 Å based on the veiling corrected, apastron spectra in this work, and from archival observations of other WTTS.
- With veiling corrected spectra, we will measure the relative contribution of He I 5876 Å emission from each star. This will be accomplished by first subtracting the

empirically derived chromospheric component, then assigning a Gaussian probability of flux “ownership” centered on each star’s velocity. The distribution width will be set by the characteristic FWHM of emission in high-accretion rate epochs. Flux at a given velocity will be assigned to each star based on the ratio of the Gaussian probability at that velocity-distance from each star. The average of this relative flux (corrected for the difference in the TWA 3Aa–3Ab stellar parameters) will provide a quantitative measure of relative accretion rates onto each star.

- More robust quantitative statements about [O I] stability will also be possible after veiling corrections.
- There is a consistent absorption notch in the red-shifted wings of the H α spectra that may provide information on the dynamics of infalling accretion flows that warrants an in-depth analysis.

I would like to first acknowledge the input of Robert Mathieu on this thesis chapter. I would also like to thank Diego Muñoz and Enrico Ragusa for useful discussions of circumbinary accretion theory, and Adam Kowalski and John Wisniewski for discussion of chromospheric emission. Some of the observations reported in this paper were obtained with the Southern African Large Telescope (SALT). STSDAS and PyRAF are products of the Space Telescope Science Institute, which is operated by AURA for NASA. This work has made use of data from the European Space Agency (ESA) mission *Gaia* (<https://www.cosmos.esa.int/gaia>), processed by the *Gaia* Data Processing and Analysis Consortium (DPAC, <https://www.cosmos.esa.int/web/gaia/dpac/consortium>). Funding for the DPAC has been provided by national institutions, in particular the in-

stitutions participating in the *Gaia* Multilateral Agreement. All figures in this paper were generated using the python package MATPLOTLIB (Hunter 2007).

References

- Alencar, S. H. P., Bouvier, J., Walter, F. M., et al. 2012, *A&A*, 541, A116
- Andrews, S. M., Czekala, I., Wilner, D. J., et al. 2010, *ApJ*, 710, 462
- Anthonioz, F., Ménard, F., Pinte, C., et al. 2015, *A&A*, 574, A41
- Artymowicz, P., & Lubow, S. H. 1994, *ApJ*, 421, 651
- . 1996, *ApJL*, 467, L77
- Astraatmadja, T. L., & Bailer-Jones, C. A. L. 2016, *ApJ*, 833, 119
- Bai, X.-N., Ye, J., Goodman, J., & Yuan, F. 2016, *ApJ*, 818, 152
- Bailer-Jones, C. A. L. 2015, *PASP*, 127, 994
- Basri, G., Johns-Krull, C. M., & Mathieu, R. D. 1997, *AJ*, 114, 781
- Bertin, E., & Arnouts, S. 1996, *Astron. Astrophys. Suppl. Ser.*, 117, 393
- Bramall, D. G., Sharples, R., Tyas, L., et al. 2010, in *Proc. SPIE*, Vol. 7735, *Ground-based and Airborne Instrumentation for Astronomy III*, 77354F
- Bramall, D. G., Schmoll, J., Tyas, L. M. G., et al. 2012, in *Proc. SPIE*, Vol. 8446, *Ground-based and Airborne Instrumentation for Astronomy IV*, 84460A
- Brown, T. M., Baliber, N., Bianco, F. B., et al. 2013, *PASP*, 125, 1031
- Buckley, D. A. H., Swart, G. P., & Meiring, J. G. 2006, in *Proc. SPIE*, Vol. 6267, *Society of Photo-Optical Instrumentation Engineers (SPIE) Conference Series*, 62670Z
- Calvet, N., & Hartmann, L. 1992, *ApJ*, 386, 239

- Capelo, H. L., Herbst, W., Leggett, S. K., Hamilton, C. M., & Johnson, J. A. 2012, *ApJL*, 757, L18
- Cazzoletti, P., Ricci, L., Birnstiel, T., & Lodato, G. 2017, *A&A*, 599, A102
- Cuadra, J., Armitage, P. J., Alexander, R. D., & Begelman, M. C. 2009, *MNRAS*, 393, 1423
- Czekala, I., Andrews, S. M., Torres, G., et al. 2016, *Astrophys. J.*, 818, 156
- Dahm, S. E. 2008, *AJ*, 136, 521
- de Val-Borro, M., Gahm, G. F., Stempels, H. C., & Pepliski, A. 2011, *Mon. Not. R. Astron. Soc.*, 413, 2679
- Dotter, A., Chaboyer, B., Jevremović, D., et al. 2008, *ApJS*, 178, 89
- Dunhill, A. C., Cuadra, J., & Dougados, C. 2015, *MNRAS*, 448, 3545
- Dupree, A. K., Brickhouse, N. S., Cranmer, S. R., et al. 2012, *ApJ*, 750, 73
- Ercolano, B., & Owen, J. E. 2010, *MNRAS*, 406, 1553
- . 2016, *MNRAS*, 460, 3472
- Facchini, S., Juhász, A., & Lodato, G. 2018, *MNRAS*, 473, 4459
- Fang, M., van Boekel, R., Wang, W., et al. 2009, *A&A*, 504, 461
- Farris, B. D., Duffell, P., MacFadyen, A. I., & Haiman, Z. 2014, *ApJ*, 783, 134
- Flores Soriano, M., Strassmeier, K. G., & Weber, M. 2015, *A&A*, 575, A57
- Gaia Collaboration, Brown, A. G. A., Vallenari, A., et al. 2018, *ArXiv e-prints*

- Gaia Collaboration, Prusti, T., de Bruijne, J. H. J., et al. 2016, *A&A*, 595, A1
- Gallet, F., & Bouvier, J. 2013, *A&A*, 556, A36
- Gullbring, E., Hartmann, L., Briceno, C., & Calvet, N. 1998, *ApJ*, 492, 323
- Gully-Santiago, M. A., Herczeg, G. J., Czekala, I., et al. 2017, *ApJ*, 836, 200
- Günther, R., & Kley, W. 2002, *A&A*, 387, 550
- Hartigan, P., Edwards, S., & Ghandour, L. 1995, *ApJ*, 452, 736
- Hartigan, P., & Kenyon, S. J. 2003, *ApJ*, 583, 334
- Hartmann, L., Hewett, R., & Calvet, N. 1994, *ApJ*, 426, 669
- Hayasaki, K., Mineshige, S., & Sudou, H. 2007, *PASJ*, 59, 427
- Hayasaki, K., Saito, H., & Mineshige, S. 2013, *PASJ*, 65, 86
- Herczeg, G. J., Cruz, K. L., & Hillenbrand, L. A. 2009, *ApJ*, 696, 1589
- Herczeg, G. J., & Hillenbrand, L. A. 2008, *ApJ*, 681, 594
- . 2014, *ApJ*, 786, 97
- Hirth, G. A., Mundt, R., & Solf, J. 1997, *A&AS*, 126, 437
- Honeycutt, R. K. 1992, *PASP*, 104, 435
- Houdebine, E. R. 2009, *MNRAS*, 397, 2133
- . 2012, *MNRAS*, 421, 3189
- Houdebine, E. R., Butler, C. J., Garcia-Alvarez, D., & Telting, J. 2012, *MNRAS*, 426, 1591

- Houdebine, E. R., Stempels, H. C., & Oliveira, J. H. 2009, MNRAS, 400, 238
- Huerta, M., Hartigan, P., & White, R. J. 2005, AJ, 129, 985
- Hunter, J. D. 2007, Computing in Science and Engineering, 9, 90
- Jayawardhana, R., Hartmann, L., Fazio, G., et al. 1999, ApJL, 520, L41
- Johns-Krull, C. M. 2007, ApJ, 664, 975
- Johnstone, C. P., Jardine, M., Gregory, S. G., Donati, J.-F., & Hussain, G. 2014, MNRAS, 437, 3202
- Juhász, A., & Facchini, S. 2017, MNRAS, 466, 4053
- Kellogg, K., Prato, L., Torres, G., et al. 2017, ApJ, 844, 168
- Kennedy, G. M., Wyatt, M. C., Sibthorpe, B., et al. 2012, MNRAS, 421, 2264
- Koenigl, A. 1991, ApJL, 370, L39
- Kowalski, A. F., Hawley, S. L., Wisniewski, J. P., et al. 2013, ApJS, 207, 15
- Kraus, A. L., Ireland, M. J., Martinache, F., & Hillenbrand, L. A. 2011, ApJ, 731, 8
- López-Santiago, J., Montes, D., Fernández-Figueroa, M. J., & Ramsey, L. W. 2003, A&A, 411, 489
- Lubow, S. H., & Martin, R. G. 2018, MNRAS, 473, 3733
- Lubow, S. H., & Ogilvie, G. I. 2000, ApJ, 538, 326
- Mamajek, E. E. 2005, ApJ, 634, 1385
- Manara, C. F., Frasca, A., Alcalá, J. M., et al. 2017, A&A, 605, A86

- Martin, R. G., & Lubow, S. H. 2017, *ApJL*, 835, L28
- Mathieu, R. D., Stassun, K., Basri, G., et al. 1997, *AJ*, 113, 1841
- Miranda, R., Muñoz, D. J., & Lai, D. 2017, *MNRAS*, 466, 1170
- Muñoz, D. J., & Lai, D. 2016, *ApJ*, 827, 43
- Muzerolle, J., Hartmann, L., & Calvet, N. 1998, *AJ*, 116, 455
- Papaloizou, J. C. B., & Lin, D. N. C. 1995, *ApJ*, 438, 841
- Raghavan, D., McAlister, H. A., Henry, T. J., et al. 2010, *ApJS*, 190, 1
- Ray, T., Dougados, C., Bacciotti, F., Eisloffel, J., & Chrysostomou, A. 2007, *Protostars and Planets V*, 231
- Roedig, C., Dotti, M., Sesana, A., Cuadra, J., & Colpi, M. 2011, *MNRAS*, 415, 3033
- Schmidt, S. J., Kowalski, A. F., Hawley, S. L., et al. 2012, *ApJ*, 745, 14
- Shu, F., Najita, J., Ostriker, E., et al. 1994, *ApJ*, 429, 781
- Shu, F. H., Najita, J. R., Shang, H., & Li, Z.-Y. 2000, *Protostars and Planets IV*, 789
- Sills, A., Pinsonneault, M. H., & Terndrup, D. M. 2000, *ApJ*, 534, 335
- Simon, M. N., Pascucci, I., Edwards, S., et al. 2016, *ApJ*, 831, 169
- Sousa, A. P., Alencar, S. H. P., Bouvier, J., et al. 2016, *A&A*, 586, A47
- Tofflemire, B. M., Mathieu, R. D., Ardila, D. R., et al. 2017a, *ApJ*, 835, 8
- Tofflemire, B. M., Mathieu, R. D., Herczeg, G. J., Akeson, R. L., & Ciardi, D. R. 2017b, *ApJL*, 842, L12

van Dokkum, P. G. 2001, PASP, 113, 1420

White, R. J., & Basri, G. 2003, ApJ, 582, 1109

Young, M. D., Baird, J. T., & Clarke, C. J. 2015, MNRAS, 447, 2907

Young, M. D., & Clarke, C. J. 2015, MNRAS, 452, 3085

Chapter 5

Conclusions

*I've been pullin' on a wire, but it just
won't break. I've been turnin' up the
dial, but I hear no sound. I resist
what I cannot change, and I want to
find what can't be found.*

Adam Granduciel

The results presented in Chapters 2–4 mark a significant advancement in our understanding of the binary-disk interaction. Through these studies we have confirmed the most fundamental predictions of binary accretion theory, while at the same time providing an extensive set of observations that push the limits of current theory. In this concluding chapter, I summarize the collective results of this thesis, comment on their broader impact to our understanding of mass accretion in young binary stars, and outline some of the largest lingering questions that remain.

A common thread of the work presented in this thesis is the search for variable mass accretion onto stars in young binary systems that is driven by their orbital dynamics. Study of pulsed accretion in eccentric binaries began in concert with the theoretical investigations of Artymowicz & Lubow (1996) and the Mathieu et al. (1997) observations of DQ Tau. Since then, advancement on an observational front has proceeded slowly due to the challenge of conducting major time-series investigations. With the advent of a coordinated global network of telescopes provided by the Las Cumbres Observatory (LCO), however, we have been able to conduct one such investigation. In a long-term photometric monitoring campaign we have probed traditional accretion diagnostics at a high sampling rate continuously for ~ 10 binary orbits. Additionally, these data have allowed us to supplement this work with more expensive observational techniques (high-cadence photometry, time-series spectroscopy), supplying a background context for each observation, and ultimately, a deeper analysis.

In Chapter 2 we have used these observations to unequivocally show that bursts of accretion consistently occur near the periastron passages of the eccentric binary DQ Tau. At a surface level, these results agree with the predictions of numerical simulations but in detail, point to the limitations that can be drawn from comparing the two. This limitation

is due to the tight orbital configuration of DQ Tau, which likely prevents the presence of stable circumstellar disks through both outer, dynamical and inner, magnetic truncation processes. We hypothesize that this is the main driver of the discrepancies that we observe.

With the addition of high-cadence observations of DQ Tau, a rich and structured morphology of the accretion events was revealed. Rather than a steady rise and fall, periastron accretion events consist of a series of discrete bursts that occur at varying orbital phases and varying amplitudes. The presence of quasi-periodic apastron accretion events were also seen, which are not predicted by any simulations of binary accretion. This variability, as well as the large variability in the total mass accreted from one orbit to the next, points to a much more complex interaction than models depict.

In Chapter 3 we have shown a remarkably similar accretion behavior is present in the short-period, eccentric binary TWA 3A. Also host to consistent periastron accretion events, the relative amplitude and orbital phases in which elevated accretion occurs is near identical to DQ Tau. The agreement between these two systems, which have accretion rates that differ by close to an order of magnitude, is a compelling confirmation of pulsed accretion. TWA 3A should also suffer from the same circumstellar disk truncation processes as DQ Tau, so while the pulsing mechanism remains uncertain (e.g. tidally torqued circumstellar disks or the direct interaction between stars and streams), it appears to operate consistently across these systems.

In Chapter 4 we have explored the kinematic behavior of the TWA 3A stellar accretion flows with time-series, high-resolution optical spectroscopy. Through this analysis we have found that spectral-line accretion diagnostics confirm the photometric behavior observed above, while also pointing to a near absence of accretion outside of the periastron bursts. In numerical simulations with circumstellar disks, some level of constant accretion is predicted, while TWA 3A lines emission appears completely chromospheric in origin near apastron.

This observed behavior may be due to TWA 3A’s low overall accretion rate, or it may be a further line of evidence for the lack of circumstellar disks.

Another exciting and potentially important result that came from this spectroscopic analysis was the evidence for preferential accretion on the TWA 3A primary star. This measurement was made by monitoring the velocity structure of the narrow, accretion-tracing emission line He I 5876 Å, which was consistently emitted at the radial velocity of the primary star. This is a surprising result given that the vast majority of numerical simulations predict that circumbinary accretion streams should preferentially feed the secondary component directly, or through its disk (e.g. Artymowicz & Lubow 1996; Farris et al. 2014). This behavior and its potential for balancing the binary mass ratio is numerically reproduced with such consistency that it has been proposed to explain certain aspects of the main-sequence binary population (e.g. Young & Clarke 2015). The only simulations that find deviation from secondary-favored accretion are those that include secular interactions between the binary and disk (e.g. Muñoz & Lai 2016). In this scenario, the precession of an eccentric circumbinary disk gap alternates which star is preferentially fed stream material. This result for TWA 3A is only one constraint in one corner of a large and unexplored parameter space, but it may be revealing the importance of long-timescale processes that typically are not probed by numerical simulations.

Beyond the details of our findings in TWA 3A, the demonstration of He I 5876 Å as a probe of the accretion rate for individual components of spectroscopic binaries is an important result. It opens the possibility for a similar analysis on a number of other binary systems, many of which have existing datasets containing this line. A census of preferential accretion in binary systems with diverse orbital parameters should be readily attainable in the near future.

Collectively, the results of this thesis have placed strong observational constraints on when and where accretion takes place in eccentric, short-period binary systems. In doing so, we have provided an indirect probe of the binary-disk interaction. Under these orbital parameters, the picture of the binary-disk interaction that emerges from this work for is one of dynamic and variable mass streams that fill the inner circumbinary disk gap. In the likely absence of circumstellar accretion disks, the discrete and variable bursts we observe may be probes of the direct interaction between the stars, their magnetospheres, and circumbinary accretion streams. If so, these results reveal the reaction of inner circumbinary disk material to binary orbital dynamics, which is not accessible in longer period systems where circumstellar disks “buffer” this interaction. Still, the presence of periodic accretion bursts is compelling evidence that outer, circumbinary disk material is being brought inward every orbital period.

The original design of this thesis program sought to answer the question of how circumbinary disk material crosses a cleared gap to feed a central binary. While we can begin to build a picture of this interaction for short-period, eccentric binaries, our data do not allow us to definitively rule out the presence of small amounts of stable circumstellar disk material or establish the way in which the stellar magnetic fields interact with surrounding material. Additionally, interpreting these observations has been challenging without numerical simulations that specifically investigate this area of parameter space.

At the conclusion of this thesis, many open questions remain, but a few are of particular relevance given the results presented here. First, how do high-velocity flows interact with strong stellar magnetospheres? This may be the interaction taking place in DQ Tau and TWA 3A, yet few theoretical predictions exist for this scenario and it represents a challenging region to probe observationally.

Second, how does the binary orbit perturb the inner edge of the circumbinary disk

and launch accretion flows? In principle, observing the dynamics of the region should be accessible with MIR spectroscopy of molecular tracers of warm gas (e.g. Carr et al. 2001). Assessing the kinematic variability of this gas may provide a direct comparison with existing numerical simulations while helping to address whether the short-timescale stellar accretion variability observed here could be rooted in variability at the inner edge of the circumbinary disk. Additionally, a determination of circumbinary gap asymmetries may be possible with these MIR lines, providing a test of the Muñoz & Lai (2016) prediction.

And third, how does the accretion behavior depend on binary orbital parameters? This thesis has only probed one small corner of a vast parameter space, but it has supplied a road map for a more extensive analysis of binary accretion. Testing how accretion variability is affected by the binary orbit is likely to provide the largest lever to constrain numerical simulations.

Our understanding of the binary-disk interaction and to a larger degree binary star formation has significantly lagged that of single stars. From both an observational and computational perspective, binary systems pose significant challenges to study. With the major increase in computing resources and in the time-domain capabilities of observational astronomy, the time is now ripe to confront our understanding of binary star formation. Doing so will advance our knowledge of a diverse range of physical process from star and planet formation to stellar evolution to the mergers of binary black holes. This thesis is one small step toward that ultimate goal.

References

Artymowicz, P., & Lubow, S. H. 1996, *ApJL*, 467, L77

Carr, J. S., Mathieu, R. D., & Najita, J. R. 2001, *ApJ*, 551, 454

Farris, B. D., Duffell, P., MacFadyen, A. I., & Haiman, Z. 2014, *ApJ*, 783, 134

Mathieu, R. D., Stassun, K., Basri, G., et al. 1997, *AJ*, 113, 1841

Muñoz, D. J., & Lai, D. 2016, *ApJ*, 827, 43

Young, M. D., & Clarke, C. J. 2015, *MNRAS*, 452, 3085

Appendix A

SALT–HRS Red-Arm Specific Reductions

*When the going gets weird, the weird
turn pro.*

Raoul Duke

A.1 SALT–HRS Red-Arm Specific Reductions

As described in Section 4.3.1.1, geometric distortions of the HRS pseudo-slit are variable across the dispersion axis in red arm spectral orders. This results in an increasingly broad resolution element with wavelength in a given spectral order, which distorts the shapes of lines when combining overlapping spectral orders. The main culprit of this distortion is a tilt in the pseudo-slit image that increases with pixel column (although we note that the even without the tilt, the pseudo-slit’s FWHM in a given pixel row also increases with pixel column).

The top panels of Figure A1 display this distortion with two emission lines from the same spectral order of a Th-Ar comparison spectrum ($m=62$). The left panel shows an emission line, Ar I 7948.2Å, which falls on the left side of the CCD. Each curve is the emission profile of this line for an individual pixel row in the spectral order. The line color corresponds to the pixel row which is presented in the color bar at the right. Here it is clear that the line peak falls at smaller column-pixel values at the bottom of the spectral order and higher column-pixel values at the top. On the right side of the CCD, this behavior is more extreme where from the top of the spectral order to the bottom, the pseudo-slit image has shifted by more than the line profile’s FWHM value. One Ar line severely affected in this way is presented in the top right panel of Figure A1. Simply summing the flux across pixel-columns, as most extraction methods do, would increasingly smear the line’s flux, extensively lowering the spectral resolution.

Our scheme to correct this distortion exploits the fact that emission lines in a Th-Ar comparison spectra provide an image of the pseudo-slit at discrete wavelengths across the spectral order. By measuring the “ridge line” of many emission lines in a spectral order,

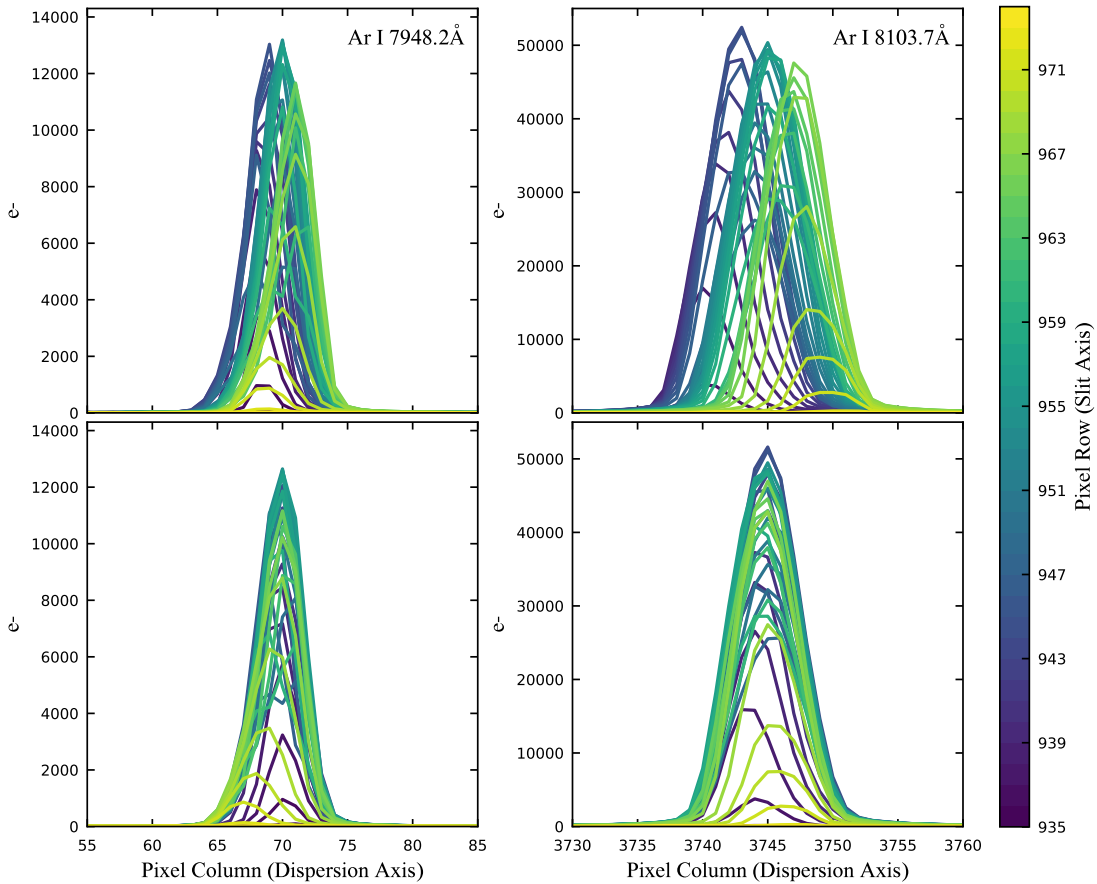


Figure A1 Two Ar I emission lines, 7948.2Å and 8103.7Å, are presented on the left and right columns, respectively, extracted from the 62nd spectral order ($\sim 7945\text{\AA}$ to 8110\AA) of a Th-Ar comparison in the SALT-HRS red arm. All four panels display the distribution of the emission line’s flux across the dispersion axis (an image of the pseudo-slit). The line color signifies the pixel row across the vertical extend of the spectral order. Flux profiles prior to pseudo-slit rectification are shown in the top panels with the transformed version below. (Pixel rows displayed here are extracted from the order rectified image.)

we are able to map the tilt of the pseudo-slit as a function of the column pixel and row pixels within the spectral order. This mapping can then be used to transform, or “rectify” the pseudo-slit.

The correction of this distortion as we have conceived it here requires spectral orders that fall directly across pixel rows, with no curvature across the CCD. This is not case for raw HRS red arm images, nor is it for any echelle spectrograph. As such, we first rectify the spectral orders with the IRAF, NOAO.longslit functions `fitcoords` and `transform`. (For

reference, the spectral lines presented in top panels of Figure A1 are extracted from single pixel rows of the order rectified image.)

For each spectral order the center row is set as the zero-point about which pixel rows above and below are transformed to match. For each pixel row we record the location of emission line's peaks with a Gaussian fit. The column-pixel locations of these line peaks, x_{row} , are then fit to the peak at the order center, x_{center} , with the following expression:

$$x_{\text{center}} = x_{\text{row}} + Ay_{\text{offset}}x_{\text{row}} + By_{\text{offset}}x_{\text{row}}^2 + Cy_{\text{offset}}, \quad (\text{A.1})$$

where $y_{\text{offset}} = y - y_{\text{center}}$, the number of pixel rows away from the order center. The best-fit values for A , B , and C then define the correction for a given row where Equation A.1 is applied as a geometric coordinate transformation. In order to conserve flux during this process, we multiply the transformed flux values by the determinant of the transformation's Jacobian matrix. We find this preserves the flux values of each row to within 1%.

The bottom panels of Figure A1 presents the pseudo-slit-rectified line profiles where the pseudo-slit is aligned with the pixel columns, signified by their overlapping profiles. This process reduces the size of the order-extracted resolution element at all points across the order and increases the consistency across wavelength.

We note that the pseudo-slit image width increases for every pixel row with increasing pixel column. This can be seen as a wider distribution in the bottom right panel compared to the bottom left. This behavior is present prior to order rectification and it not introduced by it. The effect is minor, however, compared to the pseudo-slit tilt and we do not attempt to correct for it.

Appendix B

Distance Inference from Gaia Parallax

*I know when to go out, I know when
to stay in, get things done.*

David Bowie

B.1 Distance Inference from Gaia Parallax

The determination of distance (d) from a Gaia (Gaia Collaboration et al. 2016) parallax (ϖ) is not necessary as straightforward as $d = 1/\varpi$ with an associated uncertainty of $\sigma_d = (1/\varpi^2)\sigma_\varpi$. In the Bayesian framework this can be represented as having a non-uniform prior on the distance, which represents the non-uniform radial distribution of stars around the Sun. In the Bayesian framework:

$$P(d|\varpi) = \frac{P(\varpi|d)P(d)}{P(\varpi)}, \quad (\text{B.1})$$

Where $P(\varpi)$ is a constant and

$$P(\varpi|d) = \frac{1}{\sqrt{2\pi}\sigma_\varpi} e^{-\frac{(\varpi-1/d)^2}{2\sigma_\varpi^2}}, \quad (\text{B.2})$$

assuming the parallax errors are normally distributed. For the distance prior, we adopt the exponentially decreasing stellar space density used in Bailer-Jones (2015) and Astraatmadja & Bailer-Jones (2016a):

$$P(d) = \frac{1}{2L^3} d^2 e^{-d/L}. \quad (\text{B.3})$$

This distribution corresponds to a constant space density for small d , with an exponential tail for distances much larger than $2L$. For an end-of-mission *Gaia*-like catalog, the optimum scale-length is $L = 1.35\text{kpc}$ (Astraatmadja & Bailer-Jones 2016a).

Due to known systematic errors in *Gaia* parallaxes on the order of 0.1 mas (Arenou et al. 2018; Lindegren et al. 2018), which have yet to be fully characterized, we inflate our parallax uncertainty by this value. Even with this conservative measure, the resultant distance uncertainty improves upon previous estimates for the TWA 3 system distance by more than an order of magnitude.

The effect of the non-uniform distance prior has the largest effect on parallax measurements with large fractional uncertainty. In the case of TWA 3A and TWA 3B, the fractional uncertainties are small ($\sim 4 \times 10^{-3}$) and the resultant distance posterior does not deviate significantly from a normal distribution with $\sigma = (1/\varpi^2)\sigma_\varpi$. For this reason, we quote the mode distance with a standard error uncertainty in Table 4.1, which corresponds to the 16 and 84% percentile of the posterior distribution.

References

Arenou, F., Luri, X., Babusiaux, C., et al. 2018, ArXiv e-prints

Astraatmadja, T. L., & Bailer-Jones, C. A. L. 2016a, ApJ, 832, 137

Bailer-Jones, C. A. L. 2015, PASP, 127, 994

Gaia Collaboration, Prusti, T., de Bruijne, J. H. J., et al. 2016, A&A, 595, A1

Lindgren, L., Hernandez, J., Bombrun, A., et al. 2018, ArXiv e-prints

Appendix C

DQ Tau K2 Light Curve

*Rule number one, I'm number one.
You hear that? I like to kid around.
Rule number two, the croc is number
two.*

Joe Dirt

C.1 DQ Tau K2 Light Curve

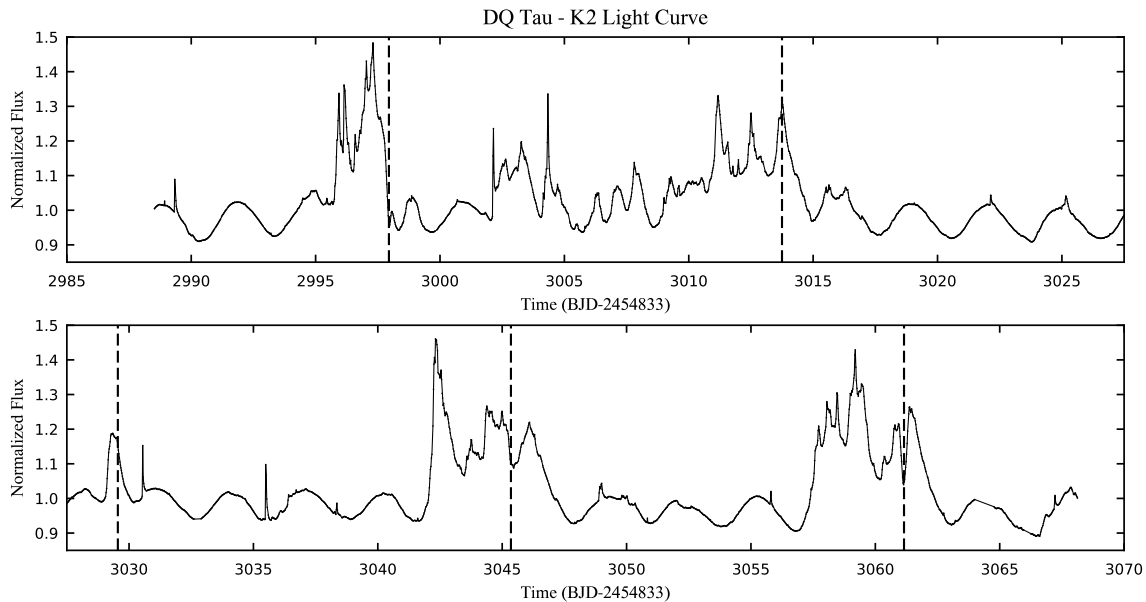


Figure C1 K2 Campaign 13 light curve of the T Tauri binary DQ Tau. Photometry presented is the long-cadence sampling rate using the raw 99 pixel circular aperture extracted with the k2sff pipeline (Vanderburg & Johnson 2014).

To aid in our discussion of the accretion level in TWA 3A near apastron, we present the K2, Campaign 13, long-cadence light curve of DQ Tau. The photometric measurements come from the Vanderburg & Johnson (2014), k2sff pipeline using the raw photometric values for the 99 pixel aperture. We present the raw, rather than corrected values because the algorithm that attempts to correct for the ~ 6 hr thruster fire assumes a relatively constant flux, which DQ Tau clearly does not have. Thruster fires shift the *Kepler* point-spread-function over pixels with different response functions, but these are small compared to the intrinsic variability. The 99 pixel aperture contains the entire range of pixels that thruster jitter might spread light over and does not include flux from adjacent stars.

In this light curve there is clear star-spot modulation that is typical of non-accreting

systems. Our interpretation of these data is that there is no accretion taking place outside of the discrete periastron bursts. This is a rich and interesting light curve containing accretion variability and stellar flares that certainly warrants an in-depth analysis.

References

Vanderburg, A., & Johnson, J. A. 2014, *PASP*, 126, 948